DRAFT VERSION MARCH 23, 2017
Preprint typeset using LaTeX style emulateapj v. 01/23/15

SPACE TELESCOPE AND OPTICAL REVERBERATION MAPPING PROJECT. III. OPTICAL CONTINUUM EMISSION AND BROAD-BAND TIME DELAYS IN NGC 5548

M. M. FAUSNAUGH[1], K. D. DENNEY[1,2,3], A. J. BARTH[4], M. C. BENTZ[5], M. C. BOTTORFF[6], M. T. CARINI[7], K. V. CROXALL[1,2], G. DE ROSA[1,2,8], M. R. GOAD[9], KEITH HORNE[10], M. D. JONER[11], S. KASPI[12,13], M. KIM[14], S. A. KLIMANOV[15], C. S. KOCHANEK[1,2], D. C. LEONARD[16], H. NETZER[12], B. M. PETERSON[1,2], K. SCHNÜLLE[17], S. G. SERGEEV[18], M. VESTERGAARD[19,20], W.-K. ZHENG[21], Y. ZU[1,22], M. D. ANDERSON[5], P. ARÉVALO[23], C. BAZHAW[5], G. A. BORMAN[18], T. A. BOROSON[24], W. N. BRANDT[25,26,27], A. A. BREEVELD[28], B. J. BREWER[29], E. M. CACKETT[30], D. M. CRENSHAW[5], E. DALLA BONTÀ[31,32], A. DE LORENZO-CÁCERES[10], M. DIETRICH[33,34], R. EDELSON[35], N. V. EFIMOVA[15], J. ELY[8], P. A. EVANS[9], A. V. FILIPPENKO[21] , K. FLATLAND[16], N. GEHRELS[36], S. GEIER[37,38,39], J. M. GELBORD[40,41], L. GONZALEZ[16], V. GORJIAN[42], C. J. GRIER,[1,25,26], D. GRUPE[43], P. B. HALL[44], S. HICKS[7], D. HORENSTEIN[5], T. HUTCHISON[6], M. IM[45], J. J. JENSEN[19], J. JONES[5], J. KAASTRA[46,47,48], B. C. KELLY[49], J. A. KENNEA[24], S. C. KIM[14], K. T. KORISTA[50], G. A. KRISS[8,51], J. C. LEE[14], P. LIRA[52], F. MACINNIS[6], E. R. MANNE-NICHOLAS[5], S. MATHUR[1,2], I. M. M$^{\rm c}$HARDY[53], C. MONTOURI[54], R. MUSSO[6], S. V. NAZAROV[18], R. P. NORRIS[5], J. A. NOUSEK[25], D. N. OKHMAT[18], A. PANCOAST[55,56], I. PAPADAKIS[57,58], J. R. PARKS[5], L. PEI[4], R. W. POGGE[1,2], J.-U. POTT[17], S. E. RAFTER[13,59], H.-W. RIX[17], D. A. SAYLOR[5], J. S. SCHIMOIA[1,60], M. SIEGEL[24], M. SPENCER[11], D. STARKEY[10], H.-I. SUNG[14], K. G. TEEMS[5], T. TREU[49,61,62], C. S. TURNER[5], P. UTTLEY[63], C. VILLFORTH[64], Y. WEISS[13], J.-H. WOO[45], H. YAN[65], AND S. YOUNG[35]

Draft version March 23, 2017

ABSTRACT

We present ground-based optical photometric monitoring data for NGC 5548, part of an extended multi-wavelength reverberation mapping campaign. The light curves have nearly daily cadence from 2014 January to July in nine filters (*BVRI* and *ugriz*). Combined with ultraviolet data from the *Hubble Space Telescope* and *Swift*, we confirm significant time delays between the continuum bands as a function of wavelength, extending the wavelength coverage from 1158 Å to the z band ($\sim$9160 Å). We find that the lags at wavelengths longer than the V band are equal to or greater than the lags of high-ionization-state emission lines (such as He II λ1640 and λ4686), suggesting that the continuum-emitting source is of a physical size comparable to the inner broad-line region (BLR). The trend of lag with wavelength is broadly consistent with the prediction for continuum reprocessing by an accretion disk with $\tau \propto \lambda^{4/3}$. However, the lags also imply a disk radius that is 3 times larger than the prediction from standard thin-disk theory, assuming that the bolometric luminosity is 10% of the Eddington luminosity ($L = 0.1L_{\rm Edd}$). Using optical spectra from the Large Binocular Telescope, we estimate the bias of the interband continuum lags due to BLR emission observed in the filters. We find that the bias for filters with high levels of BLR contamination ($\sim$20%) can be important for the shortest continuum lags, and likely has a significant impact on the u and U bands owing to Balmer continuum emission.

Keywords: galaxies: active — galaxies: individual (NGC 5548) — galaxies: nuclei — galaxies: Seyfert

[1] Department of Astronomy, The Ohio State University, 140 W 18th Ave, Columbus, OH 43210, USA
[2] Center for Cosmology and AstroParticle Physics, The Ohio State University, 191 West Woodruff Ave, Columbus, OH 43210, USA
[4] Department of Physics and Astronomy, 4129 Frederick Reines Hall, University of California, Irvine, CA 92697, USA
[5] Department of Physics and Astronomy, Georgia State University, 25 Park Place, Suite 605, Atlanta, GA 30303, USA
[6] Fountainwood Observatory, Department of Physics FJS 149, Southwestern University, 1011 E. University Ave., Georgetown, TX 78626, USA
[7] Department of Physics and Astronomy, Western Kentucky University, 1906 College Heights Blvd #11077, Bowling Green, KY 42101, USA
[8] Space Telescope Science Institute, 3700 San Martin Drive, Baltimore, MD 21218, USA
[9] University of Leicester, Department of Physics and Astronomy, Leicester, LE1 7RH, UK
[10] SUPA Physics and Astronomy, University of St. Andrews, Fife, KY16 9SS Scotland, UK
[11] Department of Physics and Astronomy, N283 ESC, Brigham Young University, Provo, UT 84602-4360, USA
[12] School of Physics and Astronomy, Raymond and Beverly Sackler Faculty of Exact Sciences, Tel Aviv University, Tel Aviv 69978, Israel
[13] Physics Department, Technion, Haifa 32000, Israel
[14] Korea Astronomy and Space Science Institute, Republic of Korea
[15] Pulkovo Observatory, 196140 St. Petersburg, Russia
[16] Department of Astronomy, San Diego State University, San Diego, CA 92182-1221, USA
[17] Max Planck Institut für Astronomie, Königstuhl 17, D–69117 Heidelberg, Germany
[18] Crimean Astrophysical Observatory, P/O Nauchny, Crimea 298409, Russia
[19] Dark Cosmology Centre, Niels Bohr Institute, University of Copenhagen, Juliane Maries Vej 30, DK-2100 Copenhagen, Denmark
[20] Steward Observatory, University of Arizona, 933 North Cherry Avenue, Tucson, AZ 85721, USA
[21] Department of Astronomy, University of California, Berkeley, CA 94720-3411, USA
[22] Department of Physics, Carnegie Mellon University, 5000 Forbes Avenue, Pittsburgh, PA 15213, USA
[23] Instituto de Física y Astronomía, Facultad de Ciencias, Universidad de Valparaíso, Gran Bretana N 1111, Playa Ancha, Valparaíso, Chile
[24] Las Cumbres Global Telescope Network, 6740 Cortona Drive, Suite 102, Santa Barbara, CA 93117, USA
[25] Department of Astronomy and Astrophysics, Eberly College of Science, The Pennsylvania State University, 525 Davey Laboratory, University Park, PA 16802, USA
[26] Institute for Gravitation and the Cosmos, The Pennsylvania State University, University Park, PA 16802, USA
[27] Department of Physics, The Pennsylvania State University, 104 Davey Lab, University Park, PA 16802
[28] Mullard Space Science Laboratory, University College London, Holmbury St. Mary, Dorking, Surrey RH5 6NT, UK
[29] Department of Statistics, The University of Auckland, Private Bag 92019, Auckland 1142, New Zealand
[30] Department of Physics and Astronomy, Wayne State University, 666 W. Hancock St, Detroit, MI 48201, USA
[31] Dipartimento di Fisica e Astronomia "G. Galilei," Università di Padova, Vicolo dell'Osservatorio 3, I-35122 Padova, Italy

1. INTRODUCTION

The continuum emission of radio-quiet active galactic nuclei (AGN) is believed to originate in an accretion disk around a supermassive black hole (SMBH). At accretion rates and masses appropriate for SMBHs, geometrically thin, optically thick accretion disks have maximum temperatures of $\sim 10^5$–10^6 K, naturally accounting for the characteristic peak of AGN spectral energy distributions (SEDs) in the far ultraviolet (UV; Burbidge 1967; Shakura & Sunyaev 1973; Shields 1978). However, a large variety of competing models of the accretion flow exist, such as thick-disk geometries at extremely super- or sub-Eddington accretion rates (Abramowicz et al. 1988; Narayan & Yi 1995). In addition, AGN exhibit nonthermal X-ray emission, which requires a hot plasma component or "corona" (e.g., Haardt & Maraschi 1991; Chakrabarti & Titarchuk 1995). The potential configurations and complex interplay between the hot corona and accretion disk admit a wide range of models with many free parameters, and searching for the unique observational signatures of a given disk model is very challenging (Sun & Malkan 1989; Laor et al. 1997; Koratkar & Blaes 1999; Vestergaard & Wilkes 2001; Telfer et al. 2002; Kishimoto et al. 2004, and references therein).

Reverberation mapping (RM; Blandford & McKee 1982; Peterson 1993, 2014) can provide insight into the structure of the accretion disk, and has become a standard tool for AGN astrophysics over the last 25 years (Clavel et al. 1991; Peterson et al. 1991; Horne et al. 1991; Kaspi et al. 2000; Peterson et al. 2004; Bentz et al. 2009; Denney et al. 2010; Grier et al. 2013b; Pancoast et al. 2014; Pei et al. 2014; Barth et al. 2015, and references therein). The basic principle of RM is that emission at two different wavelengths is causally connected, so that the time delay (or lag) between two light curves represents the light-crossing time within the system, and thereby provides a straightforward measurement of the system's physical size. For example, because the AGN continuum powers the prominent emission lines observed in Seyfert galaxy/quasar spectra, the time delays between continuum and broad-line light curves are commonly used to determine the physical extent of the line-emitting gas (the so-called broad-line region, BLR).

In a similar way, RM techniques can be used to constrain the physical processes governing AGN continuum emission. X-ray emission from the corona may irradiate and heat the accretion disk. If the corona is relatively compact and centrally located, the UV and optical emission would be expected to respond to the incident X-ray flux, "echoing" the X-ray light curve after a time delay corresponding to the light-travel time across the disk (Krolik et al. 1991). On the other hand, X-ray light curves would be expected to lag behind UV and optical light curves if the X-rays are produced by Comptonization of thermal UV/optical disk photons (Haardt & Maraschi 1991). Observational investigations of the relation between X-ray and UV/optical emission have produced ambiguous results. X-rays have been found to lead the optical emission by one to several days in some objects (e.g., Arévalo et al. 2009; Breedt et al. 2010; Shappee et al. 2014; Troyer et al. 2016), but the X-ray variability on long (> 1 year) timescales cannot always account for the optical variations (Uttley et al. 2003; Breedt et al. 2009). In addition, other studies find no long-term X-ray/optical correlations (Maoz et al. 2002), or find optical variations that lead the X-rays on shorter timescales (~ 15 days, Marshall et al. 2008).

RM can also reveal information about the size and structure of the continuum-emitting source. Emission from different portions of the disk peaks at different wavelengths depending on the local disk temperature. By translating the wavelength of the continuum emission into a characteristic temperature, time delays between continuum light curves can be used to map the temperature profile of the disk. The first statistically significant interband time delays were found in NGC 7469 by Wanders et al. (1997) and Collier et al. (1998). Sergeev et al. (2005) carried out intensive optical monitoring of 14 AGN and found evidence that longer wavelengths lag shorter-wavelength emission. More recent continuum RM campaigns have used the *Swift* observatory (Gehrels et al. 2004) to obtain unprecedentedly well-sampled light curves across X-ray, near-UV, and optical wavelengths: Shappee et al. (2014) observed NGC 2617 with *Swift* on a nearly daily basis for several months in 2014, while McHardy et al. (2014) monitored NGC 5548 with ~ 2

[32] INAF-Osservatorio Astronomico di Padova, Vicolo dell'Osservatorio 5 I-35122, Padova, Italy
[33] Department of Physics and Astronomy, Ohio University, Athens, OH 45701, USA
[34] Department of Earth, Environment, and Physics, Worcester State University, 486 Chandler Street, Worcester, MA 01602, USA
[35] Department of Astronomy, University of Maryland, College Park, MD 20742-2421, USA
[36] Astrophysics Science Division, NASA Goddard Space Flight Center, Greenbelt, MD 20771, USA
[37] Instituto de Astrofísica de Canarias, 38200 La Laguna, Tenerife, Spain
[38] Departamento de Astrofísica, Universidad de La Laguna, E-38206 La Laguna, Tenerife, Spain
[39] Gran Telescopio Canarias (GRANTECAN), 38205 San Cristóbal de La Laguna, Tenerife, Spain
[40] Spectral Sciences Inc., 4 Fourth Ave., Burlington, MA 01803, USA
[41] Eureka Scientific Inc., 2452 Delmer St. Suite 100, Oakland, CA 94602, USA
[42] MS 169-327, Jet Propulsion Laboratory, California Institute of Technology, 4800 Oak Grove Drive, Pasadena, CA 91109, USA
[43] Space Science Center, Morehead State University, 235 Martindale Dr., Morehead, KY 40351, USA
[44] Department of Physics and Astronomy, York University, Toronto, ON M3J 1P3, Canada
[45] Astronomy Program, Department of Physics & Astronomy, Seoul National University, Seoul, Republic of Korea
[46] SRON Netherlands Institute for Space Research, Sorbonnelaan 2, 3584 CA Utrecht, The Netherlands
[47] Department of Physics and Astronomy, Univeristeit Utrecht, P.O. Box 80000, 3508 Utrecht, The Netherlands
[48] Leiden Observatory, Leiden University, PO Box 9513, 2300 RA Leiden, The Netherlands
[49] Department of Physics, University of California, Santa Barbara, CA 93106, USA
[50] Department of Physics, Western Michigan University, 1120 Everett Tower, Kalamazoo, MI 49008-5252, USA
[51] Department of Physics and Astronomy, The Johns Hopkins University, Baltimore, MD 21218, USA
[52] Departamento de Astronomia, Universidad de Chile, Camino del Observatorio 1515, Santiago, Chile
[53] University of Southampton, Highfield, Southampton, SO17 1BJ, UK
[54] DiSAT, Universita dell'Insubria, via Valleggio 11, 22100, Como, Italy
[55] Harvard-Smithsonian Center for Astrophysics, 60 Garden Street, Cambridge, MA 02138, USA
[57] Department of Physics and Institute of Theoretical and Computational Physics, University of Crete, GR-71003 Heraklion, Greece
[58] IESL, Foundation for Research and Technology, GR-71110 Heraklion, Greece
[59] Department of Physics, Faculty of Natural Sciences, University of Haifa, Haifa 31905, Israel
[60] Instituto de Física, Universidade Federal do Rio do Sul, Campus do Vale, Porto Alegre, Brazil
[61] Department of Physics and Astronomy, University of California, Los Angeles, CA 90095-1547, USA
[63] Astronomical Institute 'Anton Pannekoek,' University of Amsterdam, Postbus 94249, NL-1090 GE Amsterdam, The Netherlands
[64] University of Bath, Department of Physics, Claverton Down, BA2 7AY, Bath, United Kingdom
[65] Department of Physics and Astronomy, University of Missouri, Columbia, MO 65211, USA
[3] NSF Postdoctoral Research Fellow
[56] Einstein Fellow
[62] Packard Fellow

day cadence for approximately 2 years (excepting seasonal gaps). These studies found trends of lag with wavelength that are well fit by the expectation for X-ray/far-UV reprocessing.

The present study is the third in a series describing the results of the AGN Space Telescope and Optical Reverberation Mapping (STORM) project, an intensive, multi-wavelength monitoring campaign of NGC 5548. The AGN STORM campaign is anchored by daily far-UV observations using the Cosmic Origins Spectrograph (COS; Green et al. 2012) on the *Hubble Space Telescope* (*HST*). De Rosa et al. (2015, hereinafter Paper I) give a complete introduction to the project and an analysis of the *HST* data. The COS program was complemented by a four-month broad-band photometric monitoring campaign using *Swift*, the first results of which are presented by Edelson et al. (2015, hereinafter Paper II). The *Swift* campaign achieved ~ 0.5 day cadence and detected significant lags between the UV and optical continua, which follow the expected lag-wavelength relation of a thin accretion disk ($\tau \propto \lambda^{4/3}$).

Supplementing these space-based observations are ground-based optical monitoring programs. The present study details the optical broad-band photometric monitoring component, which extends the analysis in Paper II using data in nine optical filters with $\lesssim 1$ day cadence for seven months. The similarly intensive ground-based spectroscopic monitoring will be presented by Pei et al. (in prep., hereinafter Paper V). In terms of cadence, temporal baseline, and wavelength coverage, the combination of UV and optical observations of the AGN STORM project represents the most complete RM experiment ever conducted.

The present work has three primary goals. The first is to directly compare the far-UV and optical light curves of NGC 5548 over a concurrent monitoring period. The far-UV light curve ($\sim$1350 Å) is expected to closely trace the true ionizing continuum ($\leq$912 Å), while the optical continuum ($\sim$5100 Å) appears to be delayed and somewhat smoothed compared to the UV emission. Since ground-based RM campaigns use the optical continuum as a proxy for the driving continuum light curve, understanding how the continuum emission changes as a function of wavelength is important for understanding any systematic effects in optical RM experiments. The second goal is to search for time delays between the UV and optical data, in an attempt to probe the structure of the continuum-emitting region. However, because broad-band filters pick up spectral features that arise in the BLR (e.g., strong emission lines), and these features have large lags relative to the underlying continuum (several days for a Seyfert galaxy such as NGC 5548), interband lags estimated from broad-band photometry may be biased indicators of the accretion-disk size. Therefore, our final goal is to estimate the impact of BLR emission on the observed interband time delays.

In §2, we describe the observations, data reduction, flux calibration, and general properties of the ground-based photometric light curves. In §3, we describe our time-series analysis, measuring the lag as a function of wavelength of the broad-band filters. We then explore the impact of BLR emission on the observed interband lags in §4. Finally, in §5, we discuss our results, and we summarize our conclusions in §6. Where relevant, we assume a standard cosmological model with $\Omega_m = 0.28$, $\Omega_\Lambda = 0.72$, and $H_0 = 70$ km s^{-1} (Komatsu et al. 2011).

2. OBSERVATIONS AND DATA REDUCTION

In conjunction with the *HST COS* UV RM campaign described in Paper I, NGC 5548 was observed between 2013 December and 2014 August by 16 ground-based observatories in optical broad-band filters: Johnson/Cousins *BVRI* and Sloan Digital Sky Survey (SDSS) *ugriz*. A short description of each telescope, the relevant imager, and the number of contributed epochs is given in Table 1. All observatories followed a common reduction protocol: images were first overscan-corrected, bias-subtracted, and flat-fielded following standard procedures. The reduced data, as well as nightly calibration frames, raw images, and observing logs, were then uploaded to a central repository, and the image quality was assessed by eye. Images taken in reasonable atmospheric conditions and free of obvious reduction errors were analyzed as described below.

2.1. *Differential Photometry*

The analysis is based on the `ISIS` image-subtraction software package (Alard & Lupton 1998). Images are first registered to a common coordinate system, and the images with the lowest backgrounds and best seeing are combined into a high signal-to-noise ratio (S/N) "reference" image. The other images are then rescaled to match the effective exposure time of the reference image. Next, the reference image is convolved with a spatially variable kernel to match the point-spread function (PSF) of each individual epoch, and then subtracted to leave the variable flux in each pixel. We use `ISIS`'s built-in photometry package to extract light curves from the subtracted images at the position of the AGN in NGC 5548, in units of differential counts relative to the reference image. Because each telescope/filter/detector combination has slightly different properties (pixel scales, fields of view, gains, etc.), we built reference frames and subtracted images for each unique dataset. This procedure corrects for variable seeing conditions and removes nonvariable sources such as host-galaxy starlight, allowing a clean measurement of the variable AGN flux.

2.2. *Measurement Uncertainties*

The formal errors found by `ISIS` sometimes underestimate the full uncertainties because they only account for local Poisson error contributions. In order to estimate more reliable measurement uncertainties, we examined the residual fluxes of stars in the subtracted images, and rescaled the formal `ISIS` errors to be consistent with the observed scatter. Our method is similar to that of Hartman et al. (2004, §4.1).

We first used `ISIS` to extract differential light curves at the positions of each unsaturated star in the reference images. For stars with constant flux in time, the distribution of residual fluxes at each epoch serves as an estimate of the uncertainty in the subtraction. Since we are only concerned with the magnitude of the residuals, we first take their absolute value. We then divide these values by their formal `ISIS` uncertainties, so that the resulting ratios indicate the factor by which the true uncertainties are underestimated. We set a minimum value of 1.0 for this ratio, since the uncertainty cannot be smaller than the local photon noise. Finally, we multiply the formal uncertainty for the AGN at the matching epoch by the median of the rescaling factors from all stars. The procedure ensures that the measurement uncertainty in a given image is consistent with the observed scatter of the subtracted stars. The median rescaling factor for all images was 2.9, while 75% of the rescaling factors are less than 6.6 and 98% are less than 25.0. The remaining 2% have rescaling factors between 30 and 87. The poorest subtractions result when `ISIS` cannot accurately construct the image PSF, usually because the image has too few stars.

To assess the effectiveness of this method, we adjusted the stars' uncertainties by the derived rescaling factor for each image, and then checked the goodness-of-fit for a constant-flux

Table 1
Contributing Observatories

Observatory Name	Obs ID	Aperture	Detector	Pixel Scale	Field of View	Observing Period	Filters	Epochs
Bohyunsan Optical Astronomy Observatory	BOAO	1.8m	e2v CCD231-84	0.″21	$15' \times 15'$	March-April	*V*	5
Crimean Astrophysical Observatory	CrAO	0.7m	AP7p CCD	1.″76	$15' \times 15'$	Dec-June	*BVRI*	76
Fountainwood Observatory	FWO	0.4m	SBIG 8300M	0.″35	$19' \times 15'$	Jan-August	*V*	60
Hard Labor Creek Observatory	HLCO	0.5m	Apogee USB/Net	0.″75	$25' \times 25'$	April-June	*V*	27
La Silla Observatory	GROND	2.2m	Gamma-ray Burst Optical/ Near-IR Detector	0.″33	$5' \times 5'$	Feb-July	*griz*	6
Las Cumbres Observatory Global Telescope Network	LCOGT	1.0m	SBIGSTX-16803/ Sinistro CCD-486BI	0.″23 0.″39	$16' \times 16'$ $27' \times 27'$	Jan-August	*BVugriz*	263
Lick Observatory Katzman Automatic Imaging Telescope	KAIT	0.8m	AP7 CCD	0.″80	$7' \times 7'$	Jan-July	*V*	80
Liverpool Telescope	LT	2.0m	e2v CCD 231	0.″15	$10' \times 10'$	Feb-August	*ugriz*	120
Maidanak Observatory	MO15	1.5m	SNUCAM	0.″27	$18' \times 18'$	April-August	*BVR*	45
Mt. Laguna Observatory	MLO	1.0m	CCD2005	0.″41	$14' \times 14'$	June-August	*V*	10
Mt. Lemmon Optical Astronomy Observatory	LOAO	1.0m	KAF-4301E	0.″68	$22' \times 22'$	Feb-July	*V*	26
Nordic Optical Telescope	NOT	2.5m	e2V CCD42-40	0.″19	$6' \times 6'$	April	*V*	3
Robotically Controlled Telescope	RCT	1.3m	SITe CCD	0.″30	$10' \times 10'$	Dec-May	*BV*	55
Svetloe Observatory	SvO	0.4m	ST-7XME CCD	2.″00	$12' \times 8'$	Jan-May	*BVRI*	49
West Mountain Observatory	WMO	0.9m	Finger Lakes PL-3041-UV	0.″61	$21' \times 21'$	Jan-July	*BVR*	44
Wise Observatory	WC18	0.5m	STL-6303E CCD	1.″47	$75' \times 50'$	Dec-July	*BVRI*	126

model of each star. The goodness-of-fit is calculated by

$$\chi^2/\mathrm{dof} = \frac{1}{N-1}\sum_{i}^{N}\left(\frac{c_i - \bar{c}}{\sigma_i}\right)^2, \quad (1)$$

where dof = $N-1$ is the number of degrees of freedom of the fit, c_i is the counts in the light curve at epoch i, σ_i is the rescaled uncertainty, and $\bar{c}$ is the mean counts of the light curve. 90% of the rescaled values of χ^2/dof are between 0.32 and 2.09, and the distribution peaks at 0.81, somewhat lower than would be expected for purely Gaussian statistics. This may indicate that our rescaling method is slightly overestimating the measurement uncertainties. However, given our large dataset, we can afford to be conservative in this regard.

Data from the Katzman Automatic Imaging Telescope (KAIT; Filippenko et al. 2001) and the *u*-band data from the Liverpool Telescope (LT; Steele et al. 2004) required a different treatment since these images have 10 stars or fewer, which are not enough to provide robust estimates of the error-rescaling factors. We instead calculated global rescaling factors from all available epochs, rather than individual corrections from single images. Using Equation 1, we calculate χ^2/dof for all available stars, using the unscaled `ISIS` uncertainties for σ_i. We then multiplied the uncertainties of the AGN light curve by the average value of $(\chi^2/\mathrm{dof})^{1/2}$. We found that the mean rescaling factor was 8.99 for the KAIT data and 2.23 for the *u*-band LT data. Although this method does not account for epochs with high-quality subtractions, we find the cautious approach preferable to underestimating the uncertainties.

2.3. *Intercalibration of Light Curves*

In order to combine differential light curves in the same filter but from different telescopes, it is necessary to intercalibrate the light curves to a common flux scale. This accounts for the different mean flux levels and analog-to-digital unit (ADU) definitions between the reference images, as well as small differences in filter transmission functions, detector efficiencies, etc., of the many telescopes. We model the difference of any two light curves by a multiplicative rescaling factor a and an additive shift b. While it is trivial to solve for these parameters by matching epochs where the fluxes are known to be equal, no two observations occur at precisely the same time and it is therefore necessary to interpolate the light curves. Furthermore, this method can only treat two light curves at a time, and therefore loses information by ignoring the global probability of the ensemble calibration parameters for all telescopes. In order to address both of these problems, we built a full statistical model of the intercalibrated light curve using the software package `JAVELIN`, following the `SPEAR` formalism of Zu et al. (2011).

`JAVELIN` models the light curves as a damped random walk (DRW). Although recent studies using *Kepler* light curves have shown that the DRW overpredicts the amplitude of AGN continuum variability on short timescales (Edelson et al. 2014; Kasliwal et al. 2015), the DRW provides an adequate description of the observed light curves for the noise properties and cadence/timescales of this study (we quantitatively verify this claim in the Appendix, but see also Kelly et al. 2009; MacLeod et al. 2010; Zu et al. 2013). In brief, points sampled from a DRW have an exponential covariance matrix, which is described by an amplitude σ_{DRW} that characterizes the strength of short-term variations, and a damping timescale τ_{DRW} over which the light curve becomes decoherent. Using a Markov Chain Monte Carlo (MCMC) calculation, we simultaneously fit for the shifts and rescaling factors of all light curves in a single filter. We also fit for σ_{DRW}, but our light curves do not have a sufficiently long temporal baseline to meaningfully constrain τ_{DRW}. We therefore fixed τ_{DRW} = 164 days, so as to match the value determined from multiyear historical light curves of NGC 5548 (Zu et al. 2011). The model provides a well-defined and self-consistent means of interpolating all the light curves simultaneously (see Zu et al. 2011; Li et al. 2013 for further details).

Our fitting procedure requires one light curve to be chosen to define the flux scale and mean flux level of the resulting intercalibration, so that this reference light curve is assigned a shift of 0 and a rescaling factor of 1. In the Johnson *BVRI* bands, we use the Wise C18 (WC18; Brosch et al. 2008) data as the calibration light curve, owing to its dense temporal sampling, long baseline, and large number of comparison stars (>400). For

the SDSS *ugriz* bands, we use the LT light curves, since they have the longest baseline and most complete time sampling.

Uncertainty in the intercalibration parameters for a given telescope contributes to the final measurement uncertainty. For a flux measurement $f(t_i)$ at epoch t_i, the calibrated measurement is $f_c(t_i) = af(t_i)+b$, and standard error propagation shows that the uncertainty introduced per point is $\sigma_{f_c}^2 = \sigma_a^2 f(t_i)^2 + \sigma_b^2 + 2f(t_i)\mathrm{cov}(a,b)$. Since a and b are usually anticorrelated, σ_{f_c} is often small compared to the uncertainties from image subtraction. However, this is not always the case for telescopes with very small numbers of observations, so we calculated σ_a, σ_b, and $\mathrm{cov}(a,b)$ from the posterior distributions of these parameters for each telescope, and added σ_{f_c} in quadrature to the rescaled `ISIS` uncertainties for each epoch. This treatment is very conservative, since the intercalibration uncertainty is strongly correlated between points from a single telescope. A summary of the mean intercalibration uncertainties is given in Table 2.

The choice of reference light curves defines the physical flux level of the AGN from the corresponding `ISIS` reference image (WC18 and LT). We convert the intercalibrated differential light curves to physical flux units by performing aperture photometry on these reference images. For the AGN and all unsaturated stars in the field, we measured the flux enclosed in a $5\farcs0$ radius circular aperture, and converted the summed fluxes to instrumental magnitudes. This means that the host-galaxy light within the aperture is included in the measurement of the AGN flux, and this issue is discussed in §2.4. The background sky level was estimated from an annulus with inner/outer radius of $14''/29''$ for the stars, and $118''/132''$ for the AGN (so as to avoid light from the host galaxy).

We then matched all stars to the SDSS Data Release 7 catalog (Abazajian et al. 2009), and computed the offset between instrumental magnitudes and the SDSS AB magnitudes. We did not find any significant color terms in the flux calibration from the comparison stars, although the spectral slope of the AGN would be a poor match to such color terms regardless of their small values. For the Johnson/Cousins *BVRI* bands, we determined the comparison-star magnitudes using the filter-system transformations given by Fukugita et al. (1996), and converted these to AB magnitudes using Fukugita et al. (1996) Table 8. The filter transforms have an uncertainty of ~ 0.03 mag, which we adopt as a floor for the *BVRI* flux-calibration uncertainty. The final flux-calibrated light curves are shown in Figure 1 and given in Table 8.

2.4. *Light-Curve Properties*

Table 3 gives a summary of the sampling properties of the AGN STORM continuum light curves, and shows that the light curves have approximately daily cadence over the entire campaign. Paper I and Paper II only presented the *HST* 1367 Å continuum light curve; here, we include three additional UV continuum light curves measured from the *HST* COS spectra, extracted from 5–6 Å windows centered at 1158 Å, 1479 Å, and 1746 Å, and given in Table 9. These continuum windows were chosen to be as uncontaminated as possible by absorption lines and broad emission-line wings. We also drop the *Swift V*-band light curve from this analysis, because its mean fractional uncertainty is much larger than that of the ground-based Johnson *V*-band light curve (3.2% compared to 0.8%). The reported wavelengths of the optical light curves are pivot wavelengths calculated from the filter response curves of the optical bands, and they are independent of the source spectrum (atmospheric cutoffs at 3000 Å and 1 μm were imposed for these calculations). Figure 2 shows a comparison of all the continuum light curves used in this study.

Table 2
Mean Intercalibration Uncertainty

Telecope (Matches Table 1)	*B* (%)	*V* (%)	*R* (%)	*I* (%)	*u* (%)	*g* (%)	*r* (%)	*i* (%)	*z* (%)
WC18	ref	ref	ref	ref	...	...	...	...	...
LT	...	...	...	...	ref	ref	ref	ref	ref
LCOGT1	0.9	0.2	...	...	1.1	1.2	0.5	0.1	0.3
LCOGT2	2.3	0.4	...	...	1.8	0.5	1.9	0.4	1.9
LCOGT3	1.5	0.6	...	...	...	...	...	...	...
LCOGT4	2.7	...	...	...	...	...	0.3	0.1	0.2
LCOGT5	...	0.6	...	...	...	1.3	...	...	0.7
LCOGT6	...	0.5	...	...	...	1.6	1.4	0.4	...
LCOGT7	...	1.9	...	...	...	...	...	...	...
LCOGT8	...	1.3	...	...	...	...	...	...	...
WMO	0.9	0.6	0.3	...	...	...	...	...	...
CrAO	0.2	...	0.3	0.3	...	...	...	...	...
RCT	0.2	0.1	...	...	...	...	...	...	...
MO15	...	0.4	0.7	...	...	...	...	...	...
FWO	...	0.3	...	...	...	...	...	...	...
HLCO	...	0.4	...	...	...	...	...	...	...
KAIT	...	0.1	...	...	...	...	...	...	...
MLO	...	0.7	...	...	...	...	...	...	...
LOAO	...	0.4	...	...	...	...	...	...	...

Note. — Percentages are averaged for all epochs of the given telescope, measured relative to the flux at that epoch—see §2.3 for the definition of the intercalibration uncertainty. "ref" is the reference telescope to which the others are aligned.

Table 3 also gives the variability properties of the light curves. Column 8 gives the mean flux and root-mean square (rms) scatter of the light curves, corrected for Galactic extinction assuming a Cardelli, Clayton, & Mathis (1989) extinction law with $R_V = 3.1$ and $E(B-V) = 0.0171$ mag (Schlegel et al. 1998; Schlafly & Finkbeiner 2011; Paper I). Columns 10, 11, and 12 give different estimates of their fractional variability. The fractional variability $F_{\rm var}$ of a light curve is defined by

$$F_{\rm var} = \frac{1}{\langle f(t)\rangle}\sqrt{\frac{1}{N}\sum_i^N \left\{\left[f(t_i)-\langle f(t)\rangle\right]^2 - \sigma_i^2\right\}} \qquad (2)$$

and the uncertainty in $F_{\rm var}$ is

$$\sigma_{F_{\rm var}}^2 = \left(\sqrt{\frac{1}{2N}}\frac{\langle\sigma^2\rangle}{\langle f(t)\rangle^2 F_{\rm var}}\right)^2 + \left(\sqrt{\frac{\langle\sigma^2\rangle}{N}}\frac{1}{\langle f(t)\rangle}\right)^2, \qquad (3)$$

where $f(t_i)$ is the value of the light curve at epoch i, σ_i is the associated uncertainty, $\langle f(t)\rangle$ is the (unweighted) mean value of the light curve, and $\langle\sigma^2\rangle$ is the mean square of the measurement uncertainties (Rodríguez-Pascual et al. 1997; Vaughan et al. 2003). We also estimated the fractional variability using the `JAVELIN` amplitudes, $\sigma_{\rm DRW}/\langle f\rangle$, since this is an equivalent measure of $F_{\rm var}$ under the DRW model. The values of $\sigma_{\rm DRW}/\langle f\rangle$ and $F_{\rm var}$ are often in good agreement, but with notable exceptions, as given in Table 3.

Figure 3 shows the mean flux and variability properties of these light curves. The top panel displays the mean SED (corrected for Galactic extinction). The vertical error bars show the minimum and maximum states of the AGN, which occur at HJD$-2,400,000 = 56,723.1$ and $56,818.9$, respectively. These dates are based on the *HST* 1367 Å light curve, and the other bands are adjusted for interband time delays that are measured in §3. The middle panel illustrates the logarithm of the difference in flux between the minimum and maximum states of the AGN, which cleanly isolates the variable component of the spectrum and better traces the shape of the accretion-disk SED. For comparison, a standard thin accretion disk SED with $\lambda F_\lambda \propto \lambda^{-4/3}$ is shown, arbitrarily normalized to match the

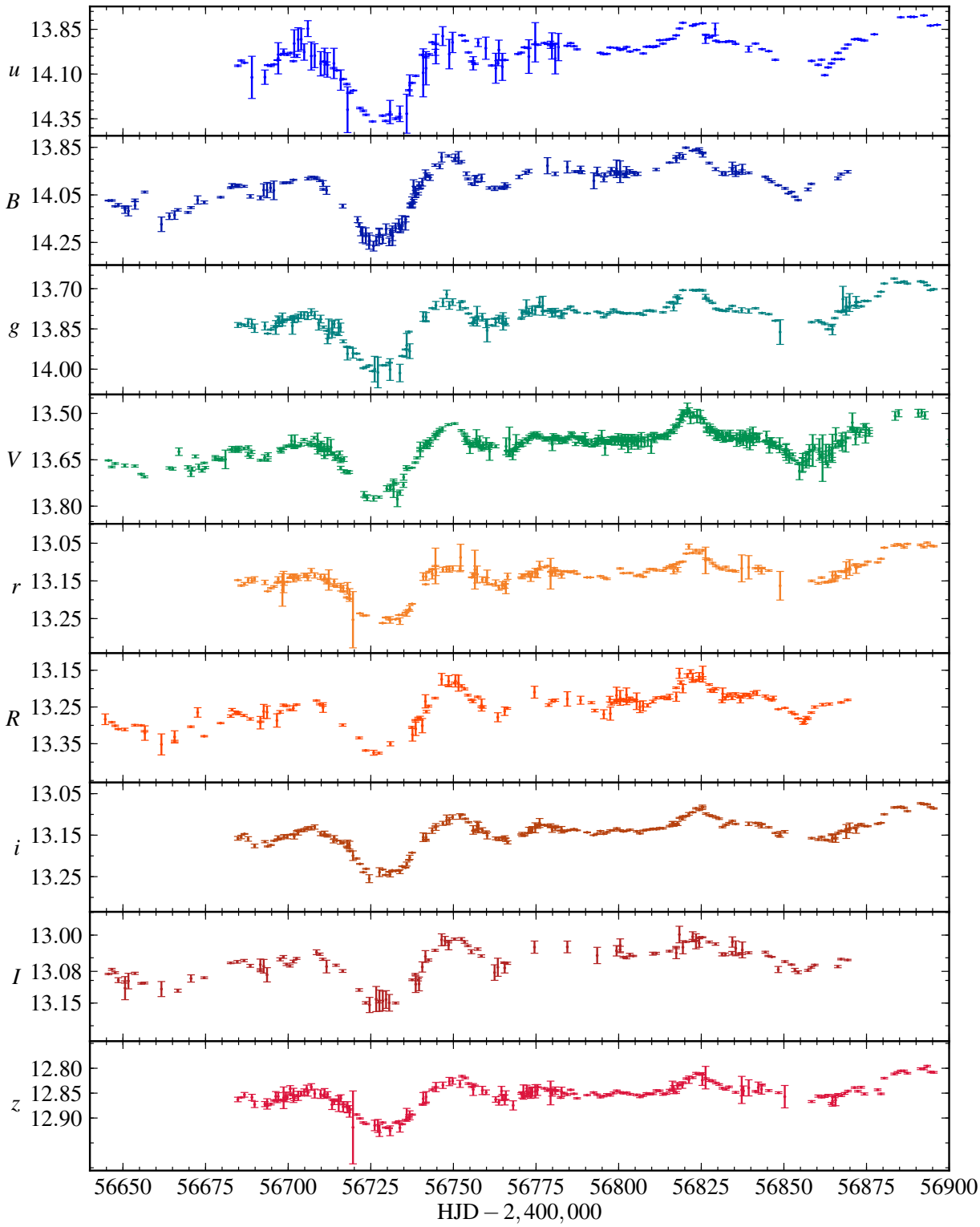

Figure 1. *BVRI* and *ugriz* ground-based light curves from the full monitoring campaign in AB magnitudes. Only the measurement uncertainties in the differential fluxes are shown. These uncertainties include those due to intercalibration, summarized in Table 2. Systematic uncertainties for the absolute flux calibration are given in Table 3.

Johnson V-band differential flux. Although the data are in excellent agreement with the prediction at longer wavelengths, the UV data lie significantly below the model SED. This discrepancy may be caused by extinction internal to the AGN, or the inner edge of the disk, which will display an exponential Wien cutoff rather than $\lambda F_\lambda \propto \lambda^{-4/3}$. A more complete discussion and modeling of the variable spectrum will be presented by Starkey et al. (in prep.). Finally, the bottom panel shows $F_{\rm var}$ as a function of wavelength. The far-UV light curves have values of $F_{\rm var} \geq 0.20$, which sharply decrease with wavelength to about 0.06 in the V band. At longer wavelengths, the trend flattens, reaching 0.02 in the z band.

At least part of this effect is caused by the constant flux contributed by the host galaxy, which becomes increasingly important at longer wavelengths. Based on spectral decomposition models and synthetic photometry (described in §4.1 and §4.2), the host galaxy contributes about 20% of the observed flux in the B band, and about 54% in the I and z bands. We corrected $\langle f(t) \rangle$ for this constant component, and Figure 3 and Table 3 also show the host-galaxy flux and revised values of $F_{\rm var}$. The effect on the trend in Figure 3 is fairly subtle, and does not change the flattening at optical wavelengths.

The larger variability amplitudes at short wavelengths suggest that the SED of NGC 5548 becomes bluer in higher flux states. The same effect was seen by Cackett et al. (2015) in NGC 5548 with near-UV grism monitoring data from *Swift*. However, the trend is driven by the light curves at wavelengths < 5000 Å, and is most significant at wavelengths $\lesssim 3500$ Å, which may be why optical studies of AGN variability do not always find any "bluer when brighter" trend (e.g., Sakata et al. 2010).

3. TIME-SERIES ANALYSIS

We measure the lags between light curves using two methods. First, we use the interpolated cross-correlation function (ICCF), as employed by Peterson et al. (2004), and estimate the uncertainty of the lag using a Monte Carlo method. Second, we use `JAVELIN`, which measures lags by modeling reverberating light curves as shifted, scaled, and smoothed versions of the driving light curve.

In the first method, the ICCF is calculated by shifting one light curve on a grid of lags τ spaced by 0.1 day, and calculating the correlation coefficient $r_{cc}(\tau)$ by linearly interpolating the second light curve. The lags are estimated from the centroid of the ICCF, defined as the mean ICCF-weighted lag for which $r_{cc}(\tau) > 0.8\, r_{\rm max}$. Uncertainties are estimated using the flux randomization/random subset selection (FR/RSS) method, wherein a distribution of ICCF centroids is built from cross correlating 10^3 realizations of both light curves. Each realization consists of randomly selected epochs (chosen with replacement), and the corresponding flux measurements are adjusted by random Gaussian deviates scaled to the measurement uncertainties. The lags reported here correspond to the medians of the ICCF centroid distributions, while the lower and upper uncertainties define their central 68% confidence intervals.

We detrended the light curves, as is common practice in RM studies (Peterson et al. 2004; Paper II), in order to remove long-term secular trends that are poorly sampled in the frequency domain and may bias the observed lag (Welsh 1999). The detrending procedure consists of subtracting a second-order polynomial linear least-squares fit (with equal weight given to all data points) from the observed light curves. Following Paper I and Paper II, we restricted the analysis to the time period coincident with the *HST* campaign, and measured the time delays relative to the *HST* 1367 Å light curve. When calculating the ICCF, we only interpolate the 1367 Å light curve. Table 4 summarizes the resulting mean lags, corrected for cosmological time dilation (the redshift of NGC 5548 is $z = 0.017175$; Paper I). Lags for the hard and soft X-ray bands of the *Swift* XRT are also included, as determined in Paper II. The ICCF for all bands is shown in Figure 4 with the solid black lines, while the centroid distributions are shown as the gray histograms. We found that the *HST* 1158 Å and 1479 Å lags were only slightly larger than the spacing of our interpolation grid (0.1 day), so we repeated the procedure on these light curves using a grid of 0.01 day. This did not have a noticeable effect on the ICCF centroids, but it did change the ICCF peaks by ~ 0.05 day. The lags reported in Table 4 make use of the finer grid for these light curves.

Our treatment of the *Swift* light curves (*UVW2, UVM2, UVW1, U,* and *B*) results in lags systematically larger than those found in Paper II, although the tension is only moderate (typically $\lesssim 1.5\sigma$). These differences are primarily caused by the different detrending procedures of the two studies. Paper II detrended the *Swift* light curves using a 30-day running mean, while we use a low-order polynomial. A running mean corresponds to a lower-pass filter than a polynomial trend, so this detrending procedure removes more low-frequency power from the light curve and is therefore expected to result in smaller lags. However, several of our light curves have very irregular sampling, which makes the calculation of the running mean poorly defined, so we instead use the low-order polynomial. The ground-based SDSS u and *Swift U* lags and the Johnson B and *Swift B* lags are consistent at the $\sim 0.6\sigma$ level using the polynomial detrending, so it is likely that the detrending procedure accounts for most of the difference between the near-UV lags. Two other smaller effects may be important for the lag determinations. First, the *Swift* UVOT optical filters are much narrower than the standard Bessell filters used for the ground-based light curves, so the observed variations are not perfectly identical (the *Swift* light curves also have slightly shorter baselines). Second, the *Swift* optical light curves have much larger fractional uncertainties, which may shift the ICCF centroid distribution of the otherwise similar light curves.

We also estimate the lags using `JAVELIN`, which calculates a maximum-likelihood lag, scale factor, and kernel width (assuming a top-hat transfer function) from the DRW covariance matrices. `JAVELIN` internally employs a linear detrending procedure, so we do not apply the second-order detrending as for the ICCF analysis. We also imposed a minimum kernel width of 0.75 day, in order to suppress solutions where `JAVELIN` finds a δ-function transfer function and aligns the reverberating light curve with the gaps between samples of the driving light curve (this is an aliasing problem associated with light curves that have similar cadences).

We adopt the medians of the posterior lag distributions and their central 68% confidence intervals as estimates of the lag and its uncertainty, which are given in Table 4. The posterior distributions are shown by the red histograms in Figure 4. The median lags are always consistent with the ICCF analysis, with the largest discrepancy being 1.7σ in the r band. The `Javelin` uncertainties generically appear to be uncomfortably small. This is because `JAVELIN` assumes correctly characterized random Gaussian measurement errors, that the line light curve is a simple lagged and smoothed version of the continuum light curve, and that the smoothing kernel is well characterized by the functional form of the model (a top-hat function). Given that all these requirements are seldom fully met (particularly the Gaussianity of the measurement errors), `Javelin` uncertainties need to be interpreted conservatively. A rough rule of thumb from modeling gravitational lens time delays is that repeated measurements for the same system will

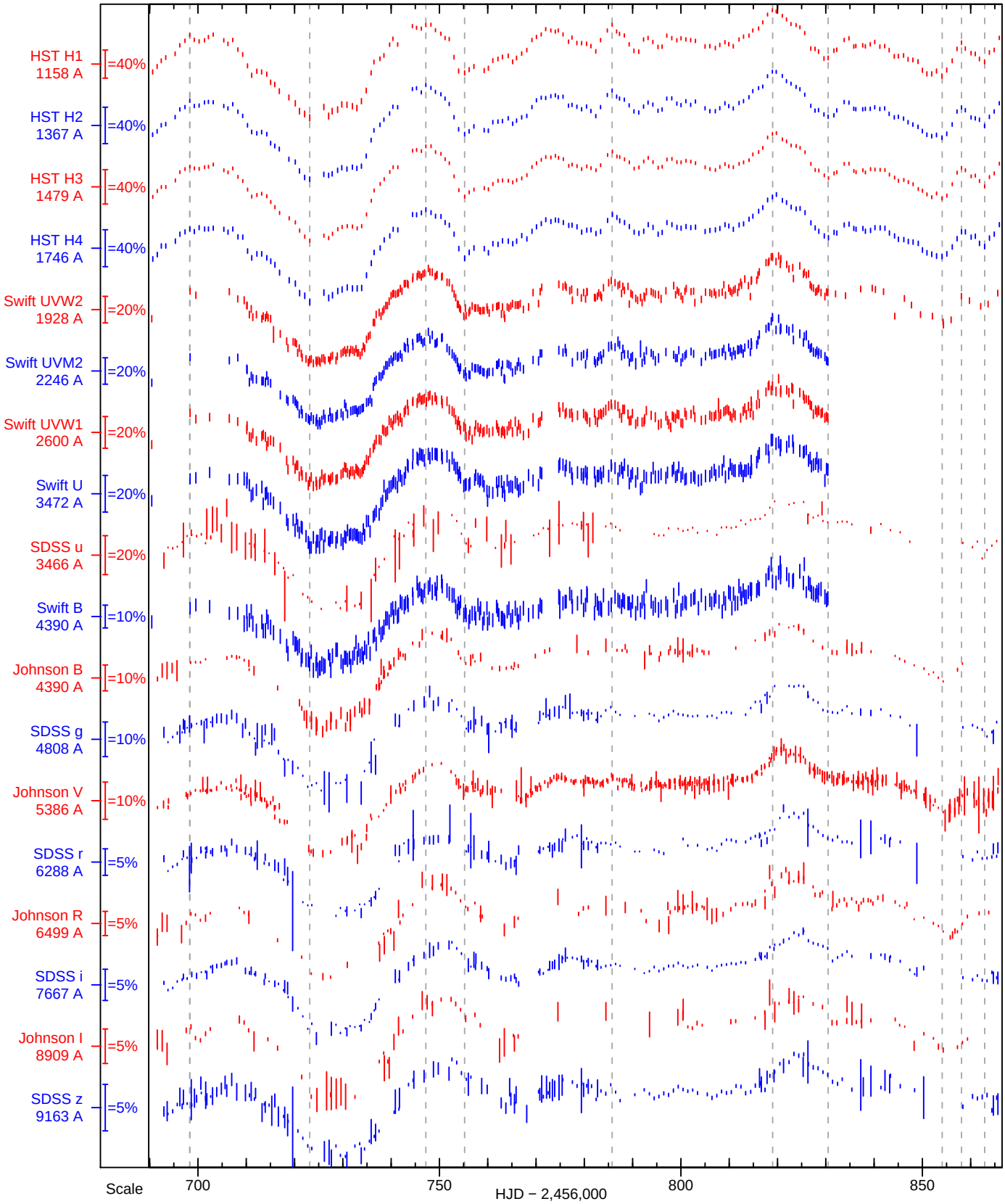

Figure 2. AGN STORM UV and optical continuum light curves used in this analysis, restricted to the observing window of the *HST* campaign. Light curves have been converted to AB magnitudes, but are rescaled and shifted for clarity—the scales along the vertical axis show the fractional variations. The vertical dashed lines mark local extrema in the *HST* 1158 Å light curve.

Table 3
Light Curves Properties

Source	Filter	$\lambda_{\rm pivot}$ (Å)	Flux Calibration Uncertainty (mag)	$N_{\rm obs}$	$\Delta t_{\rm ave}$ (days)	$\Delta t_{\rm med}$ (days)	$\langle f(t)\rangle$[a]	Host[a]	$F_{\rm var}$	$F_{\rm var2}$[b]	$\sigma_{\rm DRW}/\langle f(t)\rangle$
(1)	(2)	(3)	(4)	(5)	(6)	(7)	(8)	(9)	(10)	(11)	(12)
HST	λ1158	1158	0.050	171	1.03	1.00	52.41 ± 13.38	...	0.254 ± 0.002	0.254 ± 0.002	0.281 ± 0.054
HST	λ1367	1367	0.050	171	1.03	1.00	49.17 ± 9.89	...	0.200 ± 0.001	0.200 ± 0.001	0.205 ± 0.062
HST	λ1479	1479	0.050	171	1.03	1.00	43.54 ± 9.20	...	0.211 ± 0.001	0.211 ± 0.001	0.176 ± 0.029
HST	λ1746	1746	0.058	171	1.03	1.00	38.26 ± 7.32	...	0.190 ± 0.002	0.190 ± 0.002	0.145 ± 0.024
Swift	*UVW2*	1928	0.030	284	0.62	0.39	34.71 ± 5.83	...	0.166 ± 0.001	0.166 ± 0.001	0.150 ± 0.023
Swift	*UVM2*	2246	0.030	256	0.55	0.35	33.83 ± 5.55	...	0.162 ± 0.002	0.162 ± 0.002	0.121 ± 0.017
Swift	*UVW1*	2600	0.030	270	0.52	0.38	29.70 ± 4.01	...	0.133 ± 0.002	0.133 ± 0.002	0.097 ± 0.014
Swift	*U*	3467	0.020	145	1.20	0.99	24.43 ± 2.59	1.22 ± 0.02	0.104 ± 0.002	0.110 ± 0.002	0.236 ± 0.021
Ground	*u*	3472	0.035	270	0.52	0.38	23.18 ± 2.94	1.16 ± 0.02	0.124 ± 0.002	0.130 ± 0.002	0.068 ± 0.012
Ground	*B*	4369	0.030	151	1.11	0.98	15.15 ± 1.36	2.88 ± 0.05	0.089 ± 0.001	0.110 ± 0.001	0.090 ± 0.007
Swift	*B Swift*	4392	0.016	271	0.52	0.37	15.69 ± 1.48	2.98 ± 0.05	0.090 ± 0.002	0.112 ± 0.002	0.019 ± 0.003
Ground	*g*	4776	0.034	172	1.01	0.97	15.06 ± 0.89	3.83 ± 0.08	0.058 ± 0.001	0.078 ± 0.001	0.081 ± 0.005
Ground	*V*	5404	0.030	429	0.41	0.31	14.29 ± 0.56	4.79 ± 0.10	0.039 ± 0.001	0.058 ± 0.001	0.112 ± 0.007
Ground	*r*	6176	0.032	172	1.01	0.93	16.49 ± 0.59	5.76 ± 0.12	0.035 ± 0.001	0.054 ± 0.001	0.059 ± 0.005
Ground	*R*	6440	0.030	136	1.28	0.96	13.88 ± 0.52	5.25 ± 0.10	0.037 ± 0.001	0.060 ± 0.001	0.049 ± 0.003
Ground	*i*	7648	0.021	178	0.98	0.96	10.59 ± 0.33	5.33 ± 0.10	0.031 ± 0.001	0.063 ± 0.001	0.032 ± 0.002
Ground	*I*	8561	0.030	98	1.73	1.02	9.15 ± 0.32	4.73 ± 0.08	0.034 ± 0.001	0.071 ± 0.001	0.030 ± 0.002
Ground	*z*	9157	0.011	186	0.93	0.91	9.57 ± 0.21	5.00 ± 0.08	0.021 ± 0.001	0.044 ± 0.001	0.019 ± 0.002

Note. — $N_{\rm obs}$ gives the number of epochs in the lightcurve, $\Delta t_{\rm ave}$ gives the average cadence, $\Delta t_{\rm med}$ gives the median cadence, $\langle f(t)\rangle$ gives the mean flux (the uncertainty gives the rms scatter of the lightcurve), "Host" gives the host-galaxy flux, $F_{\rm var}$ is defined in §2.4, and $\sigma_{\rm DRW}$ is the DRW amplitude. The flux calibration uncertainty is the systematic uncertainty for conversion to physical units (i.e., zeropoint errors). For *HST*, these values are taken from Paper I, while for *Swift* the values are from Table 6 of Poole et al. (2008). The uncertainties for the ground-based lightcurves represent our calibration to the SDSS AB mag photometric system. A correction for Galactic extinction has been applied to these data (see §2.4 for details).

[a] 10^{-15}erg cm^{-2} s^{-1} Å^{-1}

[b] Corrected for host-galaxy flux

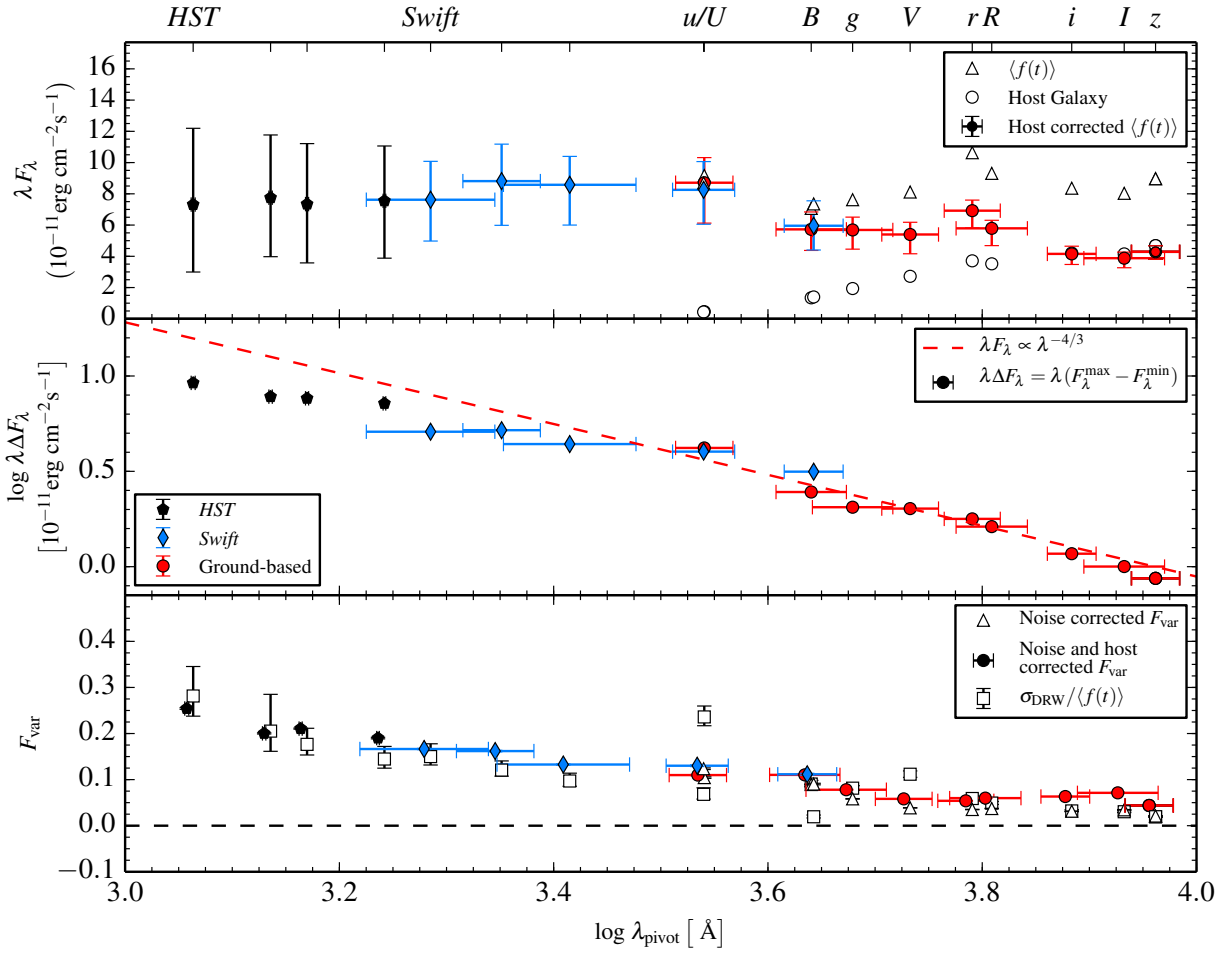

Figure 3. Top Panel: Mean SED of NGC 5548 from far-UV to optical wavelengths, corrected for Galactic extinction. The vertical error bars represent the AGN in the maximum and minimum states of the campaign. The horizontal error bars represent the rms width of the filter transmission curves. See §4 for a discussion of the host-galaxy estimate. **Middle Panel:** Variable SED component, calculated from the difference in flux between the minimum and maximum states, which more cleanly identifies the accretion-disk spectrum. The dashed red line is the predicted spectrum for a standard thin disk—discrepancies at short wavelengths may be due to extinction internal to the AGN or the inner edge of the disk. **Bottom Panel:** Fractional variability $F_{\rm var}$ as a function of wavelength. $\sigma_{\rm DRW}$ is the DRW amplitude from the JAVELIN fits. For clarity, a small shift in wavelength to the $F_{\rm var}$ points has been applied.

typically be within 2–3σ of each other.

The very small JAVELIN uncertainties may also indicate that the simple lagged and smoothed model of the reverberating light-curve model is an inadequate description of the data. Paper I found a similar result, where the shape of the line light curves was not always a good match to the observed continuum light curve. Therefore, smoothing the continuum light curve by a simple transfer function cannot always reproduce the line light curve, suggesting that other processes are important for the observed line emission (perhaps, for example, anisotropic emission/reprocessing). A more detailed investigation of this result will be pursued in upcoming papers of this series.

Using either lag estimation technique, we find that longer wavelength continuum variations follow those at shorter wavelengths. Figure 5 shows the lags as a function of the pivot wavelength of each filter. While the far-UV and near-UV light curves have time delays $\tau < 1$ day, the V band lags the 1367 Å continuum by 2.04 ± 0.21 days, and the z band lags it by 3.93 ± 0.42 days. For comparison, the He II UV and optical lines (1640 Å and 4686 Å, respectively) have a mean lag of $\sim$2.5 days relative to the 1367 Å light curve (Paper I, Paper V). The optical light curves have a time delay comparable to, and frequently larger than, that of high-ionization-state lines in the BLR.

The trend of larger lags at longer wavelengths is nearly monotonic. The most notable exceptions are (1) in the longest-wavelength filters, where the trend appears to level out near the i band, and (2) in the u and U bands. The u and U bands have mean lags of 2.03 ± 0.41 days and 1.80 ± 0.24 days, respectively, comparable to or larger than the lags of the g and V-band light curves. This may be due to emission originating in the BLR picked up in the u and U-band filters, which would contaminate measurements of the AGN continuum emission and artificially increase the observed lag. A similar explanation may exist for the downturn at the I and z bands, since Paschen continuum emission from the BLR begins at 8204 Å (see Korista & Goad 2001). We return to the question of BLR contamination in §4.

Optical continuum lags in NGC 5548 have previously been measured by Sergeev et al. (2005), and the same light curves were reexamined by Chelouche & Zucker (2013) and Chelouche (2013). Sergeev et al. (2005) found substantially longer time delays between the B and R/Cousins I bands than the lags presented here (about 8 days). However, the Sergeev et al. (2005) light curves have $\sim$3 day cadence and suffer from large seasonal/scheduling gaps of 20 days or more. The difference

in the optical lags is therefore likely caused by systematic issues with the Sergeev et al. (2005) light curves, such as unfortunate gaps that affect the cross-correlation functions. On the other hand, Chelouche & Zucker (2013) and Chelouche (2013) claim that the large optical lags are due to BLR contamination and that the true continuum lags are consistent with zero. We discuss this possibility further in §4.3, but we find this interpretation to be unlikely. These studies did not discuss the impact of gaps in the data on the multivariate cross-correlation function used to disentangle line and continuum lags, and we are further skeptical that this method can meaningfully measure lags below the cadence of the light curves (3 days, in this case).

To avoid the systematics associated with small lags, interband continuum lags should be measured with data taken near or well below the timescale of any suspected lags. The UV wavelength coverage of the STORM project therefore lends a tremendous boost to our ability to detect the continuum lags, since the UV-optical lags are 3 to 6 times larger than the interband optical lags. This has implications for ground-based studies attempting to resolve interband continuum lags. Since the optical lags are of order 1 day (or less), the diurnal cycle may make it impossible to measure reliable interband optical lags from the ground without favorable conditions.

In order to quantify the trend of lag with wavelength, we fit a model to the data presented in Figure 5 using the functional form

$$\tau = \alpha \left[\left(\frac{\lambda}{\lambda_0} \right)^{\beta} - 1 \right], \tag{4}$$

where τ is the observed lag, λ_0 is a reference wavelength, and α and β are free parameters. As in Paper II, we set $\lambda_0 = 1367$ Å and report all covariances between parameters. The results of the fits are summarized in Table 5. We find that $\alpha = 0.97 \pm 0.24$ day and $\beta = 0.90 \pm 0.12$. The parameters are strongly correlated, with a normalized correlation coefficient $\rho(\alpha, \beta) = -0.99$, and $\chi^2 = 25.94$, which approaches a low probability for 18 degrees of freedom ($\chi^2/\mathrm{dof} = 1.44$ and $P(\chi^2|\mathrm{dof}) = 0.05$ for a one-tailed χ^2 test). Since there is good reason to suspect that the *u* and *U* bands are affected by BLR emission (see §4), we also fit the data excluding these lags. With these bands excluded, we find $\alpha = 0.79 \pm 0.22$ day and $\beta = 0.99 \pm 0.14$. The normalized correlation coefficient does not change, but the goodness-of-fit is now $\chi^2 = 16.85$ with dof = 16, and $\chi^2/\mathrm{dof} = 1.05$ (and $P(\chi^2|\mathrm{dof}) = 0.60$ for the same one-tailed test). The interpretation of Equation 4 is discussed in §5.3.

4. CONTAMINATION BY BROAD-LINE REGION EMISSION

As noted above, the *u* and *U* lags are outliers from the trend in Figure 5. A major component of the flux observed in these filters is the "small blue bump," caused by bound-bound and bound-free hydrogen emission (the so-called Balmer continuum), as well as blended Fe II lines that originate in the BLR. This BLR emission may cause the *u* and *U*-band lags to be biased estimators of the light-crossing time within the continuum source. In fact, several filters pick up other spectral features that originate in the BLR. The strongest is the prominent Hα line in the *r* and *R* bands, although additional emission lines and a diffuse continuum consisting of bound-free, free-free, electron scattering, and reflection is expected to be present at all wavelengths (Korista & Goad 2001). Understanding the impact of BLR emission on the observed lags is therefore important for interpreting the interband time delays.

In this section, we assess the effect of BLR emission on the interband continuum lags. First, we decompose spectra of NGC 5548 into models of each emission component. We then estimate the fractional contribution from BLR emission in each filter using synthetic photometry. Finally, we simulate broad-band filter observations by combining mock continuum and BLR light curves, and search for biases in the lags by cross-correlating each emission component with the 1367 Å light curve.

4.1. *Spectral Decomposition*

We begin by decomposing spectra of NGC 5548 into models of each emission component. We obtained moderate-resolution ($R \approx 2000$) optical spectra of NGC 5548 using the Multi-Object Double Spectrographs (MODS; Pogge et al. 2010) on the Large Binocular Telescope (LBT; Hill et al. 2010). These observations are from 2014 June 08 and 2014 June 25 UT (HJD =2,456,817 and 2,456,834, respectively). The spectra were reduced and flux-calibrated using the `modsIDL` Spectral Reduction Pipeline.[66] The spectra cover the wavelength range from 3000 Å to 1 μm. Wavelength solutions were derived from comparison-lamp calibrations for each observing run. Relative-flux calibration was performed using three standard stars observed on the same nights as NGC 5548; however, the observations were taken in poor atmospheric conditions, making their absolute-flux calibration unreliable. We therefore rescaled the spectra so that the integrated [O III] λ5007 fluxes match the value measured for the photometric nights of the optical spectral RM campaign, $(5.01 \pm 0.11) \times 10^{-13}$ erg s^{-1} cm^2 (Paper V). The slit width and extraction window of the MODS spectra were 5″ and 15″, respectively, chosen to match those of the optical monitoring spectra. This ensures that the relative contribution of host-galaxy light, narrow-line emission, and BLR emission are the same in both datasets. We corrected for Galactic extinction following the prescription described in §2.4. We did not make any correction for telluric absorption because broad-band filters suffer from the same effect.

Since we are only concerned with the relative magnitude of various emission components to the broad-band filter fluxes, we employed a minimal spectral decomposition, which is relatively coarse compared to state-of-the-art spectral modeling. Accordingly, we do not interpret any of our model parameters as indicative of physical conditions within the AGN, and instead focus on finding a model that provides a good fit to the data (based on minimizing χ^2). Our decomposition has three components: host-galaxy starlight, the underlying AGN continuum, and the Balmer continuum shortward of $\sim$3648 Å (rest frame). We ignore the diffuse continuum at other wavelengths, since it is poorly constrained, while the Balmer continuum can be determined from the shape and amplitude of the small blue bump. Emission-line fluxes are then estimated by subtracting the summed model components from the observed spectrum.

We simultaneously fit each component with an MCMC calculation, masking AGN emission lines and telluric absorption. We also masked the long and short edges of the spectra, because the MODS flux calibration is unreliable at $\lambda < 3200$ Å and $\lambda > 9100$ Å (rest frame). At these wavelengths, we set the observed flux equal to the summed model, which implicitly sets the emission-line flux to zero. This has a small effect on the estimated BLR contamination in the *u*, *U*, *I*, and *z* bands, but is more robust than using the unreliable flux calibration.

Details of the model components are as follows.

1. **Host Galaxy:** We determined the host-galaxy spectrum

[66] A full description can be found at http://www.astronomy.ohio-state.edu/MODS/Manuals/modsIDL.pdf

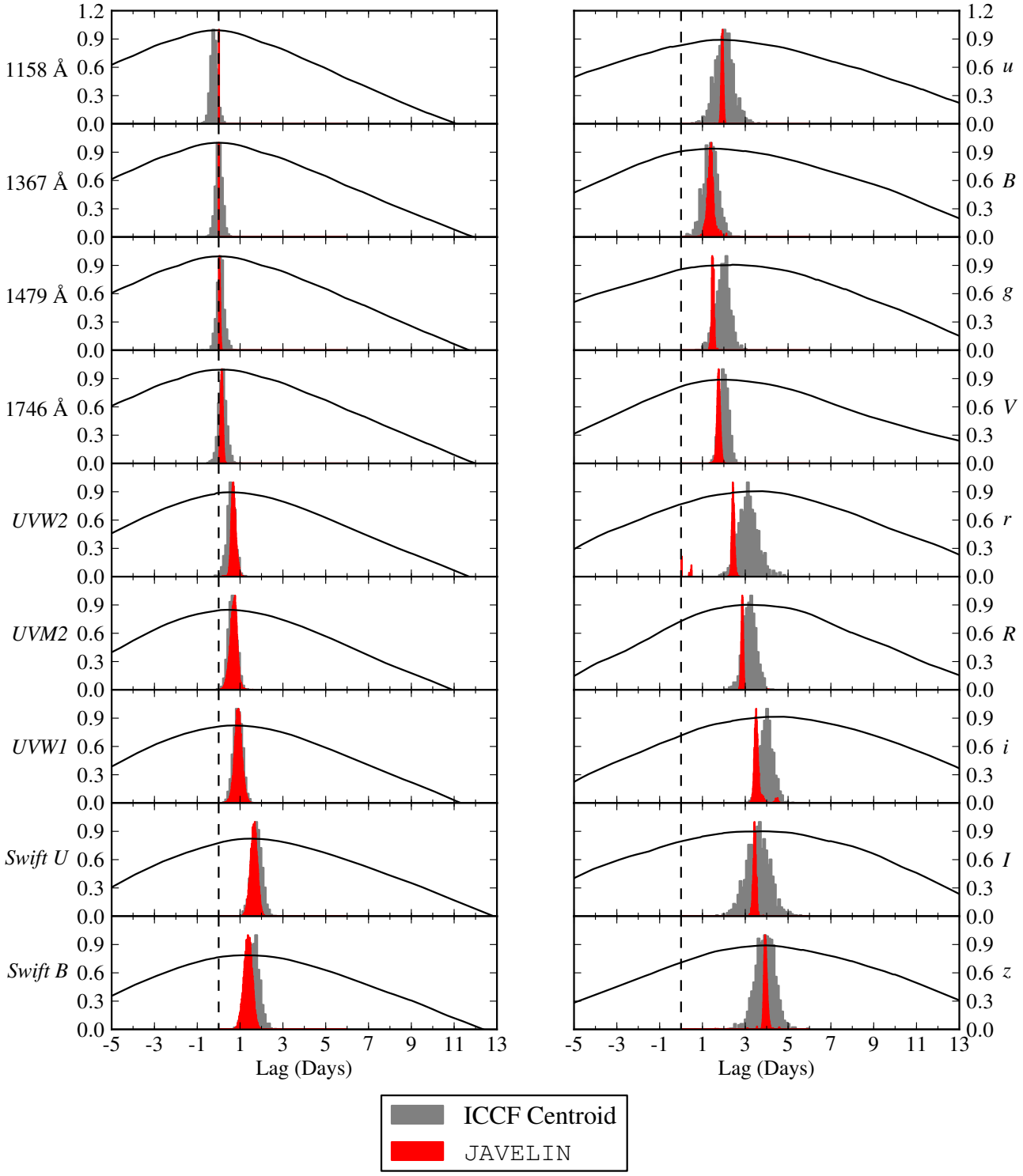

Figure 4. ICCF for all light curves, with the ordinate showing the correlation coefficient r_{cc}. Lags for data from Paper I and Paper II (following our reanalysis) are shown in the left column, ground-based optical lags are presented in the right column. The grey histograms are the ICCF centroid distributions from the FR/RSS method, the red histograms are from JAVELIN. Both histograms are in units of $P(\tau)/\max[P(\tau)]$.

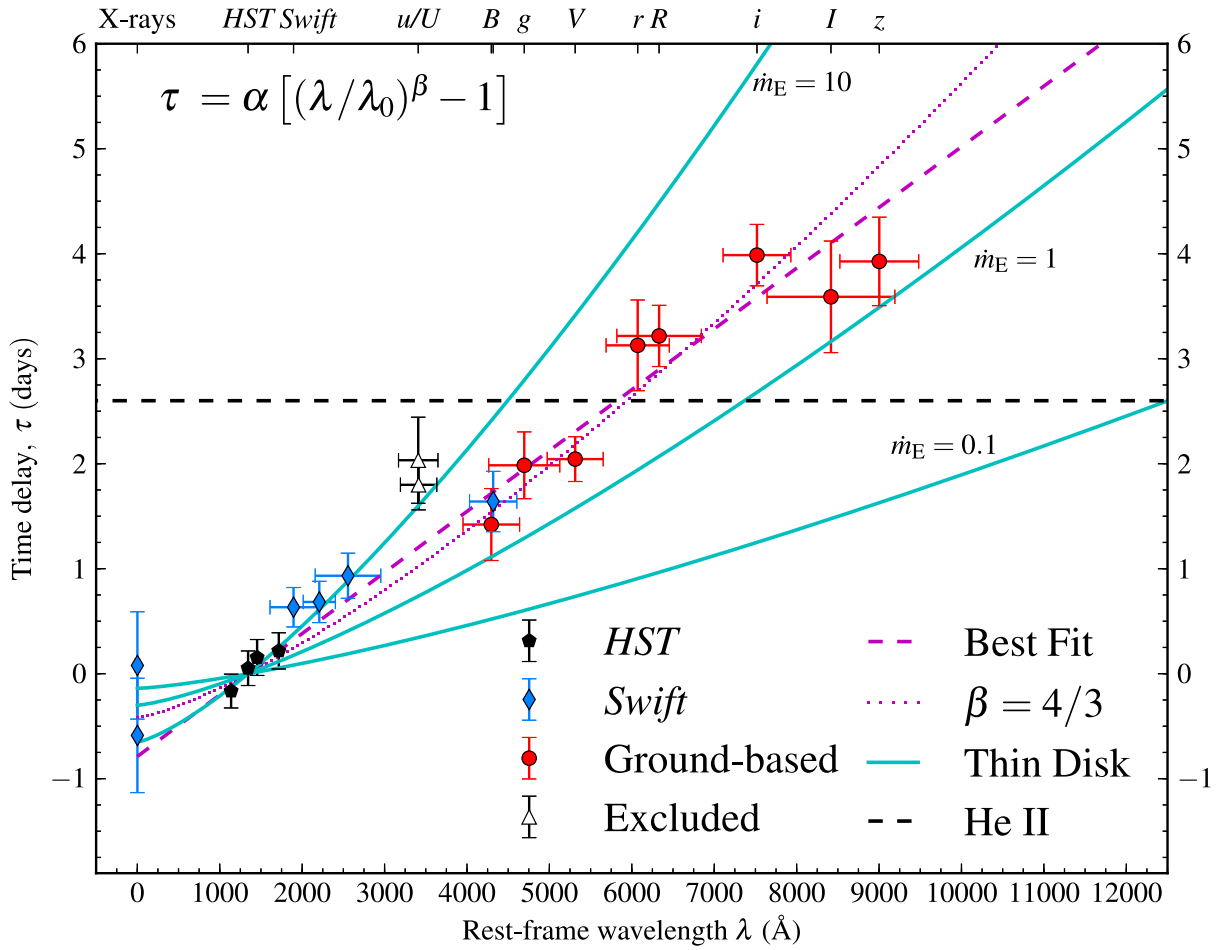

Figure 5. Time delay (ICCF centroid) as a function of pivot wavelength of the filters. The horizontal error bars represent the rms width of the filters. The best-fit model is shown by the dashed magenta line, while the fit fixing $\beta = 4/3$ is shown by the dotted magenta line. Predictions for a thin-disk model with $\dot{m}_{\rm E} = L/L_{\rm Edd}$ are shown by the solid cyan lines, although the assumptions of the model are unlikely to hold at large $\dot{m}_{\rm E}$ (see §5.3). The mean lag of the He II λ1640 and λ4686 lines is shown by the horizontal dashed black line (Paper I, Paper V).

Table 4
Time Delays

Source	Filter	$\lambda_{\rm pivot}$ (Å)	ICCF $\tau_{\rm cent}$ (days)	$\tau_{\rm peak}$ (days)	$r_{\rm max}$	JAVELIN $\tau_{\rm JAV}$ (days)
Swift	HX	4.4	$-0.65^{+0.45}_{-0.45}$	$-0.46^{+0.49}_{-0.39}$	0.35 ± 0.20	...
Swift	SX	25.3	$0.08^{+0.51}_{-0.51}$	$0.23^{+0.29}_{-0.39}$	0.44 ± 0.07	...
HST	λ1158	1158	$-0.17^{+0.16}_{-0.16}$	$-0.21^{+0.08}_{-0.10}$	1.07 ± 2.53	$-0.14^{+0.04}_{-0.04}$
HST	λ1479	1479	$0.15^{+0.18}_{-0.16}$	$0.14^{+0.23}_{-0.06}$	1.03 ± 1.08	$0.03^{+0.04}_{-0.04}$
HST	λ1746	1746	$0.22^{+0.16}_{-0.19}$	$0.21^{+0.10}_{-0.10}$	0.98 ± 0.01	$0.14^{+0.05}_{-0.05}$
Swift	*UVW2*	1928	$0.63^{+0.19}_{-0.18}$	$0.59^{+0.20}_{-0.10}$	0.92 ± 0.16	$0.68^{+0.11}_{-0.09}$
Swift	*UVM2*	2246	$0.68^{+0.19}_{-0.20}$	$0.59^{+0.20}_{-0.10}$	0.90 ± 0.27	$0.69^{+0.14}_{-0.17}$
Swift	*UVW1*	2600	$0.93^{+0.20}_{-0.23}$	$0.88^{+0.29}_{-0.20}$	0.89 ± 0.01	$0.90^{+0.16}_{-0.16}$
Swift	*U*	3467	$1.80^{+0.24}_{-0.24}$	$1.47^{+0.20}_{-0.29}$	0.88 ± 0.35	$1.62^{+0.16}_{-0.16}$
Ground	*u*	3472	$2.03^{+0.43}_{-0.39}$	$2.04^{+0.29}_{-0.39}$	0.83 ± 0.04	$1.90^{+0.04}_{-0.04}$
Ground	*B*	4369	$1.42^{+0.36}_{-0.33}$	$1.22^{+0.20}_{-0.29}$	0.91 ± 0.02	$1.36^{+0.11}_{-0.13}$
Swift	*B*	4392	$1.64^{+0.31}_{-0.27}$	$1.28^{+0.29}_{-0.39}$	0.82 ± 0.02	$1.34^{+0.19}_{-0.21}$
Ground	*g*	4776	$1.98^{+0.34}_{-0.29}$	$1.64^{+0.29}_{-0.39}$	0.89 ± 0.02	$1.45^{+0.06}_{-0.04}$
Ground	*V*	5404	$2.04^{+0.22}_{-0.20}$	$1.87^{+0.29}_{-0.10}$	0.84 ± 0.02	$1.72^{+0.07}_{-0.07}$
Ground	*r*	6176	$3.13^{+0.41}_{-0.46}$	$3.12^{+0.29}_{-0.59}$	0.85 ± 0.04	$2.38^{+0.06}_{-0.07}$
Ground	*R*	6440	$3.22^{+0.30}_{-0.29}$	$2.88^{+0.39}_{-0.20}$	0.87 ± 0.11	$2.81^{+0.04}_{-0.05}$
Ground	*i*	7648	$3.99^{+0.29}_{-0.29}$	$3.90^{+0.20}_{-0.29}$	0.90 ± 0.02	$3.46^{+0.11}_{-0.08}$
Ground	*I*	8561	$3.59^{+0.53}_{-0.54}$	$2.88^{+0.59}_{-0.88}$	0.86 ± 0.06	$3.38^{+0.07}_{-0.07}$
Ground	*z*	9157	$3.93^{+0.44}_{-0.40}$	$3.71^{+0.59}_{-0.20}$	0.84 ± 0.04	$3.88^{+0.08}_{-0.06}$

Note. — Measured relative to the *HST* 1367 Å light curve and corrected to the rest frame. The *Swift* lags are recalculated from Paper II using a second-order polynomial detrending routine, as described in §3.

Table 5
Parameters for lag–wavelength fits

Model	α (days)	β	$\rho(\alpha,\beta)$	χ^2	χ^2/dof
All	0.97 ± 0.24	0.90 ± 0.12	-0.99	25.94	1.44
	0.43 ± 0.02	4/3		38.66	2.03
No *Uu*	0.79 ± 0.22	0.99 ± 0.14	-0.99	16.85	1.05
	0.42 ± 0.02	4/3		22.64	1.33
No *UuIz*	0.58 ± 0.20	1.18 ± 0.19	-0.99	12.4	0.89
	0.45 ± 0.02	4/3		13.0	0.87

using the STARLIGHT spectral synthesis code (Cid Fernandes et al. 2004). STARLIGHT fits the observed spectrum with a linear combination of a large library of synthetic stellar populations that span a wide range of ages and metallicities (150 templates from Bruzual & Charlot 2003). The best-fitting models consist of several very old (usually $> 10^{10}$ year) stellar populations at a range of metallicities (0.4–2.5 $Z_\odot$), and provide a reasonable match to the galaxy templates used by Denney et al. (2010) and Mehdipour et al. (2015). The resulting host templates have one parameter, the flux normalization. We also impose a tight prior on the flux at 5100 Å (rest frame), chosen to match the value measured by Bentz et al. (2013) adjusted to the MODS slit width and extraction window, $(4.52 \pm 0.45) \times 10^{-15}$ erg s^{-1} cm^2 Å^{-1}.

2. **Power Law:** A broken power law is used to model the AGN continuum emission. This component has four free parameters: a flux-normalization factor, two spectral indices, and the location of the transition between indices. A loose prior (a Gaussian distribution with mean 5700 Å and width 700 Å) is imposed on the transition wavelength, to prevent it from moving to the edges of the spectra.
3. **Balmer Continuum:** The Balmer continuum component is estimated from a grid of models calculated by Dietrich et al. (2002), evaluated at varying temperatures, electron densities, and optical depths. Again, we simply choose the template that produces the overall minimum value of χ^2. The templates have a single parameter, a flux rescaling factor.

We ignored blended Fe II emission, because Fe emission is relatively weak in NGC 5548 (Denney et al. 2009; Mehdipour et al. 2015) and varies with an amplitude <50–75% that of Hβ (Vestergaard & Peterson 2005). This component is therefore expected to contribute very little flux to the broad-band photometric measurements and have a negligible impact on the observed lag. In order to assess the effect of this omission, we also fit the spectra with the small blue bump template of Mehdipour et al. (2015), which includes blended Fe II emission lines. We found that these templates produce a poorer fit than the Dietrich et al. (2002) templates at the blue end of the spectrum, which may be a result of the limited wavelength coverage of our MODS spectra in the near-UV.

Each epoch was fit independently, and the resulting component parameters are in reasonable agreement, after allowing for the intrinsic variability of the power-law and Balmer continuum. The flux rescaling factors of the power-law continuum

and galaxy templates are degenerate, so the prior imposed on the host-galaxy flux at 5100 Å (rest frame) does the most to constrain these parameters. Figure 6 shows an example of the decomposition, using the spectrum from 2014 June 08, overlaid with the filter transmission curves.

4.2. *Synthetic Photometry*

Next, we estimate the contribution of each model component to the observed flux in each broad-band filter. We first reapply Galactic reddening to the model components, since differential extinction may affect the integrated flux across broad-band filters. We then calculate the observed flux using the `synphot` `IRAF` task and filter transmission curves for the calibration telescopes (WC18 *BVRI* filters and LT *ugriz* filters), truncated at 3000 Å and 1μm to represent the atmospheric transmission cutoff. Uncertainties in the broad-band fluxes of individual components were estimated by resampling the posterior distributions of the model component parameters and rerunning `synphot` 10^3 times.

Table 6 shows the results of our synthetic photometry. The "Total" column was calculated from the original spectrum, and the fractional contributions of individual components are reported relative to this value. The uncertainties represent the central 68% confidence interval of the resampled synthetic photometry distributions. The uncertainties are generally less than 1% because of the tight prior on the 5100 Å host-galaxy flux, which forces the galaxy template to be nearly constant and limits the variation of the other model components.

We do not consider effects of changing detector sensitivity with wavelength, since quantum efficiency curves for different instruments are usually much more variable than their filter transmission curves. Quantum efficiency will have the largest impact on the *I* and *z* filters, limiting the response of these filters at wavelength shorter than the cutoff imposed at 1 μm. We investigated this effect by truncating the filter response at 9000 Å and repeating the experiment (essentially simulating a very steep quantum efficiency curve). We found that the final fractional contributions of the host/power-law components in these bands changes by 1% or less, and is therefore of minimal importance for our conclusions.

We find that the power-law component is dominant from the *u* band through the *V* band ($>$ 50% of the flux), although the host galaxy makes considerable contributions even in the *B* band ($\sim$ 20%). At longer wavelengths, the power-law component and host galaxy contribute roughly equal amounts of flux, except for the *r* and *R* bands, which include a substantial contribution from the Hα line: 20% in the *r* band and 15% in the *R* band. Line emission in all other filters is $\leq$10%. Balmer continuum emission accounts for about 19% of the flux in the *u* and *U* filters. The Mehdipour et al. (2015) blended Fe templates contribute $<$ 1% of the observed flux in the *g*, *V*, and *r* bands, confirming that Fe emission is a negligible component of the broad-band fluxes of this object.

4.3. *Impact on Time Delays*

The final step is to estimate the impact of BLR emission on the recovered interband time delays. First, we simulate light curves for the AGN continuum, Balmer continuum, and BLR emission models. We then sum the component light curves to reproduce light curves as would be observed in a given filter, and calculate the lag between the composite light curve and the *HST* 1367 Å continuum light curve.

The observed light curve is a superposition of the continuum emission and BLR emission,

$$X_{\rm obs}(t) = c(t) + l(t), \tag{5}$$

where $X_{\rm obs}$ is the observed light curve in filter X, $c(t)$ is the continuum light curve in that filter, and $l(t)$ is the line light curve, assumed to originate in the BLR. We use the term "line light curve" to refer to any emission produced in the BLR, including the Balmer continuum.

To simulate $c(t)$, we calculated the lag $\tau_{\rm cont}$ implied by the best-fit parameters in Figure 5 ($\alpha = 0.79 \pm 0.22$ and $\beta = 0.99 \pm 0.14$ in Equation 4) at the pivot wavelength of the filter, and shifted the `JAVELIN` DRW model of the *HST* 1367 Å light curve by this amount. This method assumes that the *HST* 1367 Å light curve drives $c(t)$ through instantaneous reprocessing after some light-travel-time delay, as would be expected for X-ray reprocessing in the accretion disk. [67]

In RM, the line emission is assumed to be powered by ionizing continuum emission, so that

$$l(t) = \int \Psi(\tau) C(t-\tau)\, d\tau, \tag{6}$$

where $C(t)$ is the driving continuum light curve and $\Psi(\tau)$ is the transfer function. For simplicity, we assume $C(t)$ equal to the `JAVELIN` model of the *HST* 1367 Å light curve and a top-hat transfer function,

$$\Psi(\tau) = \frac{1}{w} \text{ for } (\bar{\tau} - w/2) < \tau < (\bar{\tau} + w/2), \tag{7}$$

where $\bar{\tau}$ is the mean line lag and w is the width of the smoothing kernel. The choice of a top-hat function is for mathematical convenience and does not reflect any particular geometry, although it is widely consistent with a range of BLR configurations (for example, a spherical shell or the gross properties of an inclined disk/annulus; Peterson 2001). We varied $\bar{\tau}$ and w by octaves, with $\bar{\tau}$ = 2, 4, 8, and 16 days, and w = 0, 2, 4, 8, and 16 days. These values were chosen to sample the parameter space near the mean Hβ lag during the monitoring campaign (8.57 ± 0.67 days; Paper V). To a low approximation, the Balmer continuum and Hα lag would be expected to lie near this value. Finally, we enforced causality by setting $\Psi(\tau) = 0$ for $\tau < 0$.

We simulate light curves for the *u, U, r,* and *R* bands, in order to investigate the impact of Balmer continuum and Hα emission on the recovered lags. After generating the grid of shifted and smoothed line light curves, we renormalized each so as to reproduce the level of BLR contamination inferred from the spectral decomposition (Table 6). We then adjusted the fractional variability amplitude $F_{\rm var}$ (defined in §2.4) of both the continuum and line light curves to match their observed values. For the continuum light curves, $F_{\rm var,cont}$ is estimated directly from the observed broad-band light curves (Table 3, Column 9). For the line light curves, we set $F_{\rm var,line}$ = 4.6%, derived from the observed Hβ light curve (Paper V). We also experimented with changing the fractional variability amplitude of the line light curve to $F_{\rm var,line}$ = 0.012, 0.023, 0.092, and 0.184. Examples of two composite light curves and their model components, $c(t)$ and $l(t)$, are shown in Figure 7.

After constructing $c(t)$ and $l(t)$ for each model, we calculated the lags of these light curves relative to $C(t)$ using the

[67] Reprocessed emission is also expected to be somewhat smoothed in time compared to the driving light curve. We therefore also considered versions of $c(t)$ which are both smoothed and shifted by convolving the `JAVELIN` 1367 Å model with a top-hat function of amplitude $1/(2\tau_{\rm cont})$ for $0 < \tau < 2\tau_{\rm cont}$. We found that this smoothing made very little difference on the results, and so we only discuss the results for the shifted versions of $c(t)$ here.

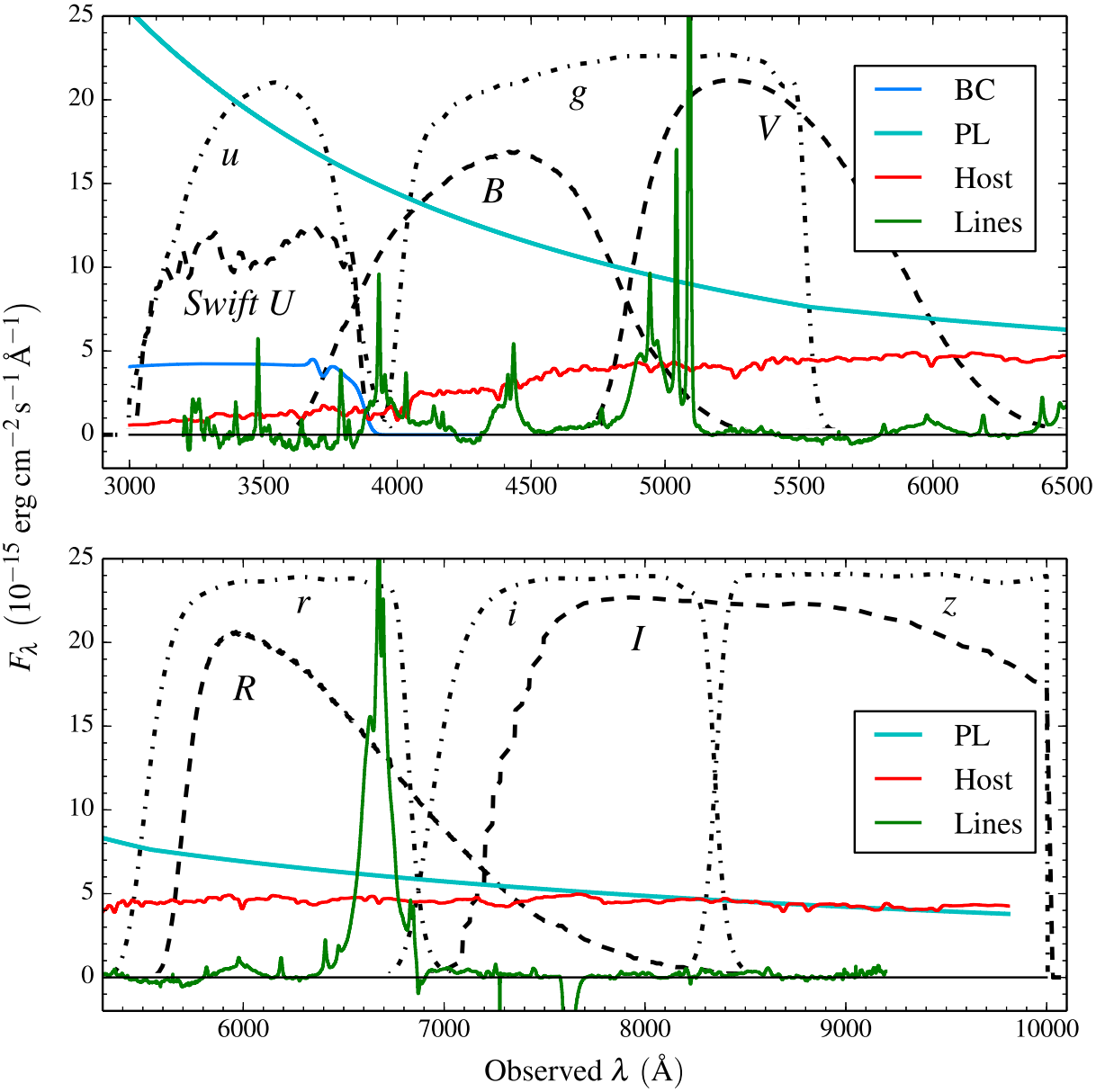

Figure 6. Decompositions of the MODS spectra from 2014 June 08, showing the contribution of the model components to different filters. "BC" is the Balmer continuum, "PL" is the power law, "Host" is the host-galaxy component, and "Lines" are the AGN emission lines. The emission lines are estimated by subtracting the total model from the observed spectrum. Johnson/Cousins optical filter transmission curves (and *Swift U*) are shown by the dashed black lines, SDSS filters are shown by the dot-dashed lines. The *Swift U* and u bands are truncated at 3000 Å and the *I* and *z* bands are truncated at 1 μm, in order to represent the atmospheric transmission cutoff.

ICCF method described in §3. In all cases, we recovered the input values of $\bar{\tau}$ and $\tau_{\rm cont}$ to within the time resolution of the model light curves (0.12 day). We then calculated the ICCF for the composite light curve $c(t)+l(t)$, finding that the recovered lags are most sensitive to the choice of $F_{\rm var,line}$ and $\bar{\tau}$ but are virtually independent of w. The resulting mean lags are shown in Figure 8 as a function of input $\bar{\tau}$ for the three values of $F_{\rm var,line}$ near that of Hβ (larger or smaller values of $F_{\rm var,line}$ do not plausibly reproduce the observed lags, and are omitted for clarity). Larger values of these parameters tend to increase the recovered lag, but at the fiducial values of Hβ the change is 0.6–1.2 days (blue point in Figure 8 with $\bar{\tau} = 8$).

We also checked for an effect of BLR contamination on the lag uncertainties. For each model, we found that larger values of $F_{\rm var,line}$ and $\bar{\tau}$ tend to increase the width of the ICCF. However, there was no correlation between these parameters and the location or width of the ICCF centroid distribution. This means that the lag uncertainties depend more sensitively on the light-curve quality rather than on any BLR contamination.

For values of $F_{\rm var,line}$ that are smaller than $F_{\rm var,cont}$ ($F_{\rm var,line} \leq 0.023$ in r and R and ≤ 0.092 in u and U), the input line lag only has a limited effect on the recovered lag, evidenced by the flattening of the trends in Figure 8. This result is in contrast to the simple expectation that the observed lag is the flux-weighted

mean lag of the line and continuum light curves, which scales linearly with the line lag. Instead, it appears that the observed lag only follows the line lag if the BLR emission dominates the variability properties of the composite light curve, as seen for the mock *r* and *R* bands at large $F_{\rm var,line}$. This indicates that the bias of the continuum lag introduced by BLR emission will usually be limited for broad-band filter light curves that are dominated by continuum emission, although the bias may still be important for small continuum lags.

Our simulations with these fiducial Hβ parameters produce *u* and *U*-band lags in excellent agreement with the observed lags, while the simulated *r* and *R*-band lags overestimate the observed lag by about 1 day. Our current campaign cannot directly address the issue of the unknown values of $F_{\rm var,line}$ and $\bar{\tau}$ for these reverberations. However, it is expected from photoionization modeling that the Balmer continuum has a larger response ($F_{\rm var,line}$) but shorter lag than Hβ, while Hα should have a smaller response but longer lag (Korista & Goad 2001, 2004). Based on Figure 8, this would serve to reduce the discrepancy between the recovered and observed lag in the *r* and *R* bands, while the recovered and observed lag in the *u* and *U* bands would remain in good agreement.

Thus, our simulations suggest that contamination by BLR emission can reasonably account for the systematic offset of the measured *u, U, r,* and *R* lags above the fit in Figure 5. This bias is well resolved in the *u* and *U* bands (the offset from the fit in Figure 5 is 2.0σ and 2.5σ, respectively), but of small importance in the *r* and *R* bands (0.6σ and 1.7σ, respectively). This result justifies our exclusion of the *u* and *U*-band data in the fit to Equation 4.

Chelouche & Zucker (2013) and Chelouche (2013) claim that BLR emission is responsible for the large *B*-*R*/Cousins *I* lags in the Sergeev et al. (2005) NGC 5548 light curves, and they find optical continuum lags consistent with 0 days. This is at odds with our results, since the BLR biases would have to be $\gtrsim 8$ days. These studies use a variation of the ICCF method (the multivariate CCF) to disentangle line and continuum lags from emission observed in a single filter. As we have already noted, gaps in the Sergeev et al. (2005) data make cross-correlation functions that rely on interpolation unreliable. Furthermore, this bias would imply that line emission contributes 30–50% of the flux in the *R* and Cousins *I* bands, which is implausibly high based on both our spectral decompositions and the composite Seyfert 1 spectrum of Chelouche (2013).

5. DISCUSSION

5.1. *UV/Optical Light Curves and Lags*

A primary goal of the AGN STORM project was to investigate how the continuum emission changes as a function of wavelength, and to assess any systematic issues introduced by using the optical continuum in place of the far-UV or extreme-UV. Figure 2 shows a detailed comparison of the *HST* 1367 Å light curve and all other data used in this study. We draw particular attention to the ground-based *V*-band light curve, since this is the most common choice of ionizing continuum proxy in ground-based RM studies. All of the major events and salient characteristics of the 1367 Å light curve are reproduced in the *V* band. There are, however, several noticeable differences.

5.1.1. *UV–Optical lags*

The first difference is a time delay between variations in the UV and optical light curves. Emission at 1158 Å, the shortest continuum wavelength available in this study, probably originates from a region of the accretion disk similar to that of the true ionizing continuum at $\lambda \leq 912$ Å. This is because the lag-wavelength relation must flatten at small wavelengths (owing to the inner edge of the disk), but the inner edge already makes an important contribution to emission at $\sim$1000 Å (Novikov & Thorne 1973). Extrapolating the fit from Equation 4 to $\lambda = 912$ Å implies a 0.26 day lag relative to the 1367 Å light curve, which is in reasonable agreement with the 1367 Å-1148 Å lag (-0.16 ± 0.16 day). We therefore adopt a value of 0.2 day for the lag between the true ionizing continuum and the 1367 Å emission, since the lags for wavelengths < 912 Å are unlikely to be much larger. This translates to a distance between the true ionizing continuum and the optically emitting portion of the disk of ~ 2.2 light days. A consequence of this UV-optical lag is that the radius of the BLR in NGC 5548 is underestimated when derived from the optical-Hβ lag. The optical–Hβ lag is variable in time, but typically has a value between 6 and 20 days (Peterson et al. 2004; Zu et al. 2011). Thus, if a similar UV–optical lag exists in other AGN, the physical size of the BLR is being systematically underestimated by up to $\sim$37% (or 11% for a lag of 20 days).

This result does not affect current optical RM SMBH masses, because RM only directly measures the virial product of the BLR, $c\tau(\Delta V)^2/G$, where τ is the BLR lag and ΔV^2 is its velocity dispersion (estimated from line-profile widths). Since the geometry and dynamics of the BLR are unknown, the virial product must be rescaled by a factor f in order to produce a SMBH mass. While every AGN has a different value of f, a statistical average $\langle f \rangle$ can be calculated by calibrating an ensemble of virial products to some other SMBH mass estimate. Currently, this is done using the $M-\sigma$ relation of local quiescent galaxies (Onken et al. 2004; Woo et al. 2010, 2013, 2015; Park et al. 2012a,b; Grier et al. 2013a). Thus, any systematic misestimation or bias of the lag (or velocity dispersion) is compensated by the calibration of $\langle f \rangle$, while the uncertainty of a single RM SMBH mass is dominated by the statistical uncertainty in $\langle f \rangle$, currently about 25–33% (Grier et al. 2013a; Woo et al. 2015). However, any physical interpretation of $\langle f \rangle$ (for example, a measure of the mean inclination of the BLR, assuming a disk or otherwise flattened geometry) requires a recalibrated value of $\langle f \rangle$ that takes into account the UV–optical lag.

Single-epoch SMBH mass estimates are also unaffected by this result, since the radius-luminosity (RL) relation is inferred from a sample of RM AGN. While the larger BLR radius measured from the UV data would increase the normalization of the RL relation, a recalibration of $\langle f \rangle$ exactly cancels this change. The UV–optical lag may introduce a second-order effect on single-epoch SMBH masses, if it is found that the magnitude of the UV–optical lag correlates with continuum luminosity or SMBH mass. Furthermore, the magnitude of the lag depends on accretion rate (see §5.3), which may also add scatter to existing mass-scaling relations. To investigate these effects, more simultaneous UV and optical RM experiments must be executed, using a sample of AGN with a wide range of luminosities.

Finally, the UV–optical lag has an impact on masses derived from direct dynamical modeling of RM data, since this method interprets the continuum-line lag as a measure of the physical radius of the BLR. To a low approximation, a larger BLR radius implies a proportionally larger SMBH mass. The effect of using UV continuum light curves for dynamical modeling studies will be investigated in future papers in this series, but until such modeling is complete, we adopt a RM-based SMBH mass for NGC 5548, since this estimate is less model dependent. From the Hβ virial products compiled by Bentz & Katz

Table 6
Flux percentage contribution by spectral component.

Filter	Total (10^{-11}erg cm^{-2} s^{-1})	PL (%)	BC (%)	Host (%)	Lines (%)
2014 June 08					
U	8.42	76.8 ± 1.5	16.7 ± 0.5	4.9 ± 0.1	2.3 ± 1.6
u	8.43	76.6 ± 1.5	16.7 ± 0.5	4.8 ± 0.1	2.7 ± 1.6
B	7.23	72.6 ± 0.9	1.4 ± 0.0	18.2 ± 0.5	7.6 ± 1.0
g	7.40	65.6 ± 0.6	...	24.3 ± 0.7	10.0 ± 0.8
V	7.39	59.0 ± 0.5	...	32.1 ± 0.9	9.1 ± 1.0
r	8.91	47.1 ± 0.4	...	33.4 ± 0.9	19.6 ± 1.0
R	8.44	48.9 ± 0.5	...	36.4 ± 1.0	14.8 ± 1.1
i	7.45	53.5 ± 0.7	...	48.5 ± 1.3	...
I	5.77	50.9 ± 0.7	...	50.3 ± 1.2	0.0 ± 0.1
z	4.60	49.5 ± 0.6	...	50.7 ± 1.0	0.0 ± 0.6
2014 June 25					
U	8.28	72.3 ± 1.5	21.4 ± 0.5	5.1 ± 0.1	1.0 ± 1.6
u	8.29	72.2 ± 1.5	21.4 ± 0.5	5.1 ± 0.1	0.6 ± 1.4
B	7.02	69.7 ± 1.0	1.8 ± 0.0	19.9 ± 0.2	8.5 ± 0.9
g	7.21	62.9 ± 0.7	...	26.6 ± 0.3	10.3 ± 0.9
V	7.29	55.9 ± 0.6	...	34.9 ± 0.4	9.0 ± 0.8
r	8.93	44.3 ± 0.4	...	35.8 ± 0.4	19.9 ± 0.7
R	8.47	46.0 ± 0.5	...	39.0 ± 0.4	15.0 ± 0.7
i	7.53	50.3 ± 0.6	...	51.9 ± 0.5	...
I	5.91	47.8 ± 0.5	...	53.7 ± 0.6	...
z	4.73	46.4 ± 0.5	...	54.0 ± 0.5	...
2014 June 08 (Blended Fe)					
U	8.49	82.6 ± 0.9	11.2 ± 0.5	5.3 ± 0.1	0.8 ± 1.1
u	8.49	82.4 ± 0.9	11.7 ± 0.5	5.3 ± 0.1	0.9 ± 1.1
B	7.23	73.5 ± 0.8	0.9 ± 0.0	20.0 ± 0.3	5.8 ± 1.0
g	7.40	64.5 ± 0.6	0.4 ± 0.0	26.7 ± 0.3	8.4 ± 0.8
V	7.38	55.9 ± 0.5	0.3 ± 0.0	35.3 ± 0.5	8.5 ± 0.7
r	8.90	44.2 ± 0.6	0.1 ± 0.0	36.6 ± 0.5	19.2 ± 0.6
R	8.43	45.7 ± 0.6	...	40.0 ± 0.5	14.4 ± 0.7
i	7.44	49.3 ± 0.9	...	53.3 ± 0.7	...
I	5.77	46.7 ± 0.9	...	55.0 ± 0.7	...
z	4.59	45.1 ± 0.9	...	55.4 ± 0.7	...
2014 June 25 (Blended Fe)					
U	8.41	82.8 ± 0.7	11.4 ± 0.4	5.8 ± 0.1	...
u	8.39	82.8 ± 0.7	12.0 ± 0.5	5.7 ± 0.1	...
B	7.02	70.7 ± 0.9	0.9 ± 0.0	22.8 ± 0.5	5.7 ± 1.2
g	7.21	60.7 ± 0.8	0.4 ± 0.0	30.5 ± 0.7	8.5 ± 1.3
V	7.27	50.4 ± 0.8	0.3 ± 0.0	40.1 ± 0.9	9.4 ± 1.2
r	8.88	38.4 ± 0.7	0.1 ± 0.0	41.3 ± 0.9	20.4 ± 1.1
R	8.40	39.6 ± 0.8	...	45.2 ± 1.0	15.5 ± 1.2
i	7.46	41.9 ± 0.8	...	60.3 ± 1.3	...
I	5.82	38.9 ± 0.9	...	62.5 ± 1.1	...
z	4.65	37.2 ± 0.9	...	63.2 ± 0.9	0.0 ± 0.1

Note. — PL is power law, BC is Balmer continuum, Host is the host galaxy, Lines are AGN emission lines. BC includes a Fe emission template in the "Blended Fe" models.

(2015), and taking $\langle f \rangle = 4.3 \pm 1.1$ (Grier et al. 2013b), we adopt a mass of $(5.2 \pm 1.3) \times 10^7\,M_\odot$ for the SMBH in NGC 5548. We note that this value moves in the correct direction for a larger BLR, but is still consistent within the quoted uncertainties of the dynamically modeled mass in Pancoast et al. (2014).

5.1.2. *Optical Smoothing*

The second difference between the UV and optical continuum light curves is that the *V*-band light curve appears to be smoother than the *HST* light curve. For example, the rapid oscillations in the UV light curve between HJD = 2,456,760 and 2,456,810 also appear in the *V*-band light curve, but at a much smaller amplitude with gentler inflections. The smoothing becomes increasingly severe at longer wavelengths where the amplitude of short-timescale variations decreases (see §2.4). These effects were also seen in NGC 2617 by Shappee et al. (2014), NGC 6814 by Troyer et al. (2016), and MCG-6-30-15 by Lira et al. (2015). Increased smoothing and decreased amplitudes are expected if shorter-wavelength emission drives the optical continuum, since the size, structure, and inclination of the accretion disk define a "continuum transfer function" that smooths the reprocessed light curve, while geometric dilution decreases the energy flux incident on large disk radii that contribute most to longer-wavelength emission.

In practical terms, the sharpest and strongest features in the *V*-band AGN STORM light curve are only slightly affected by this smoothing. Since these features provide the most leverage for constraining the CCF (Peterson 1993), we conclude that the smoothing of the optical continuum is not important for ground-based RM studies that aim only to recover a mean emission-line lag and a SMBH mass. The smoothing may be more problematic for reconstructing velocity-delay maps, direct dynamical modeling, or regularized linear inversion (Horne et al. 1991, 2004; Bentz et al. 2010b; Grier et al. 2013b; Pancoast et al. 2014; Skielboe et al. 2015). These methods are very sensitive to the fine structure of the driving continuum light curve, and smoothing the light curve will erase information that would otherwise be helpful for reconstruction of the geometry and dynamics of the BLR. Velocity-delay maps,

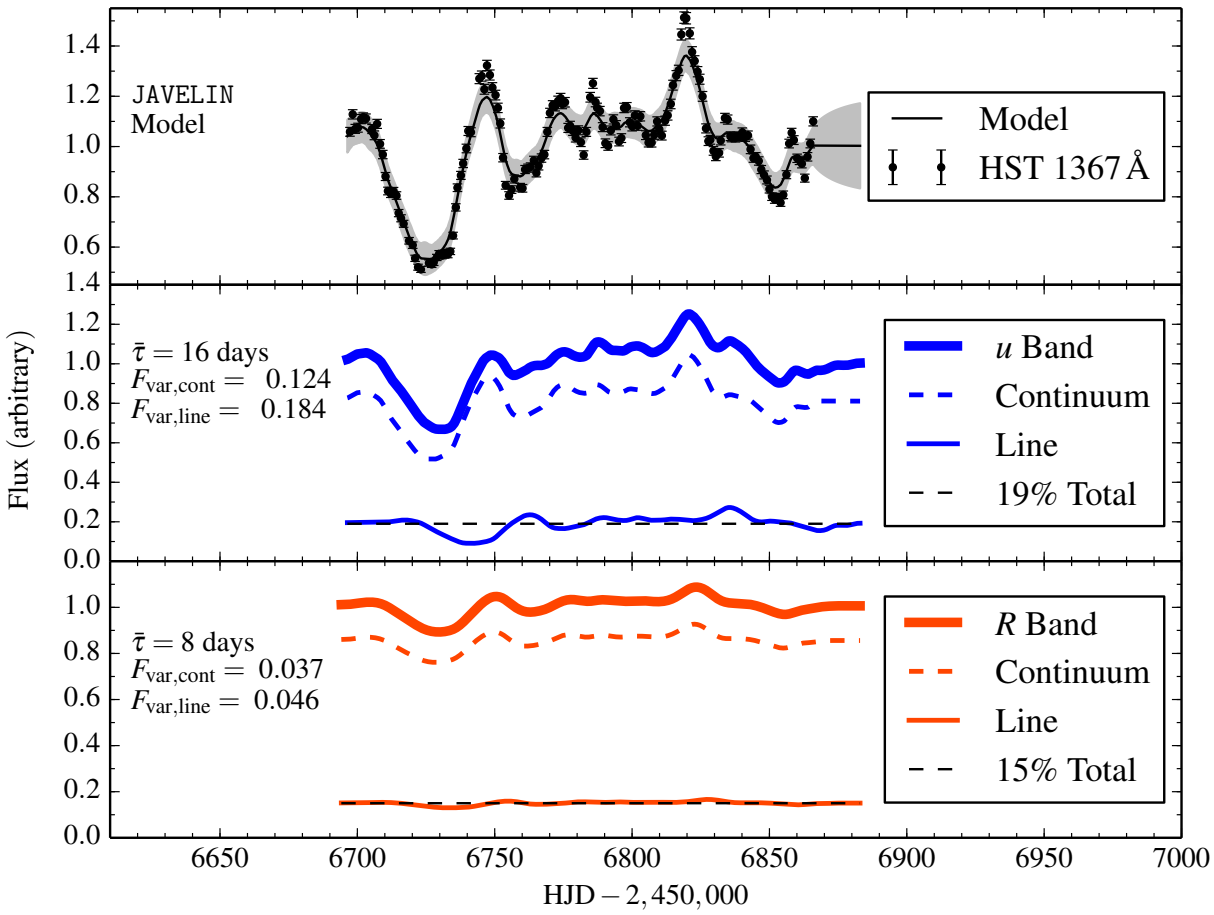

Figure 7. Examples of mock light curves, $c(t)$, $l(t)$, and $X_{\rm obs} = c(t) + l(t)$, used for the analysis in §4.3. The top panel shows the *HST* 1367 Å light curve and the JAVELIN model used to generate the mock light curves, with the 1σ uncertainty shown by the grey band. The middle panel displays an example of a mock *u*-band light curve, with a large line lag and high fractional variability, likely to result in the largest change of the observed lag. The bottom panel shows an example of a mock *R*-band light curve, with a more realistic line lag and fractional variability, chosen to be consistent with the Hβ light curve. See §4.3 for further details.

dynamical modeling, and regularized linear inversion for this dataset will be presented in upcoming papers in this series.

5.1.3. *Magnitude of UV–Optical Lags*

The large lags measured for optical bands, shown in Figure 5, are comparable to, and sometimes larger than, the lags for high-ionization-state lines such as He II λ1640 and C IV λ1549 (Paper I). If the lags do in fact represent light-travel times across the accretion disk, then the optically emitting portion of the accretion disk appears to have a similar physical extent as the highly ionized portion of the BLR. This situation implies a close connection between the BLR and continuum-emitting source. For example, BLR clouds may be directly above or interior to the portion of the accretion disk emitting in the optical. Another plausible hypothesis is that at least part of the inner, high-ionization BLR emission arises from a wind launched from the surface of the accretion disk (e.g., Collin-Souffrin 1987; Chiang & Murray 1996; Proga & Kurosawa 2010). Such models are able to reasonably explain many observed features of AGN emission lines, including their profiles, variability, and absorption characteristics (see Proga & Kallman 2004; Eracleous et al. 2009; Denney 2012; Higginbottom et al. 2014, and references therein). Alternatively, the accretion disk may smoothly merge with the BLR somewhere near 2–3 light days (for an analysis of this family of models, see, for example, Goad et al. 2012). Future papers in this series will attempt to map the geometry and kinematics of the inner BLR using the reverberation signal of high-ionization-state lines, which may shed further light on the connection between the accretion disk and BLR.

5.2. *BLR Emission and Broad-Band Filter Lags*

Based on our spectral decomposition, approximately 19% of the observed emission in the *u* and *U* bands is Balmer continuum emission from the BLR, while 15–20% of *r* and *R*-band emission is the prominent Hα line. These ratios may change with time, as shown in Table 6, depending on the luminosity state of the AGN, the difference in phase between the continuum and line light curves, and the light curves' variability amplitudes. For mean flux levels near the BLR contamination in the *u, U, r,* and *R* bands, as well as variability amplitudes and line lags that match the observed Hβ light curve, our experiments with mock light curves indicate biases in the interband continuum lag of $\sim$0.6–1.2 days.

These results depend on the assumption that all BLR emission light curves have properties similar to the Hβ light curve. It is likely that the diffuse continuum actually has a stronger response but smaller lag than Hβ, while Hα is expected to have a weaker response but larger lag (Korista & Goad 2001, 2004; Bentz et al. 2010a). Since these parameters have offsetting

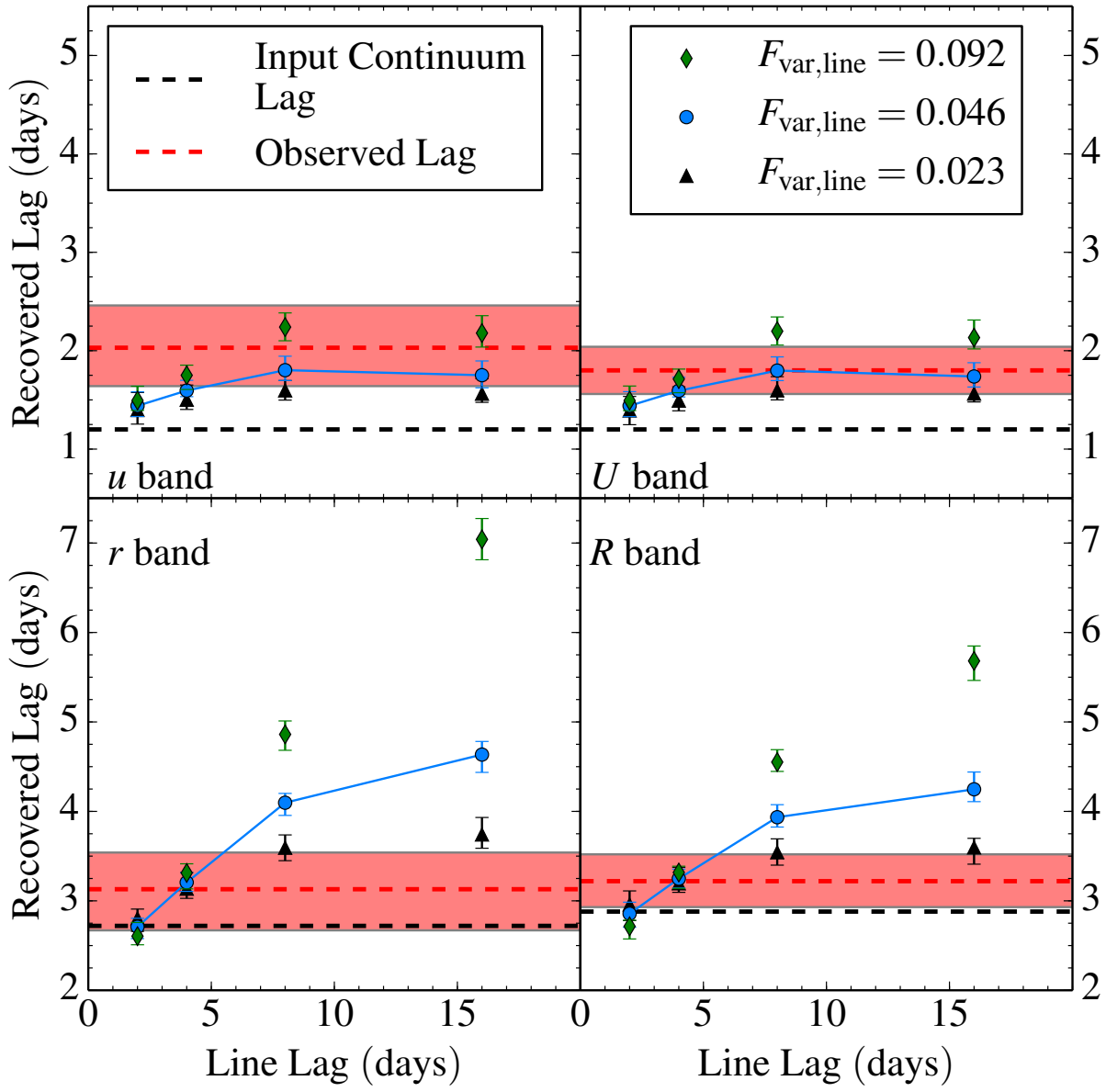

Figure 8. Recovered lags of mock light curves as a function of input line light curve $l(t)$ lag. The colored points show the results for different variability amplitudes of the line light curve. The solid blue lines indicate the variability amplitude observed in the Hβ light curve. The black dashed line represents the input lag of the continuum light curve $c(t)$, while the red dashed line is the observed lag and the red band is its 1σ uncertainty. See §4.3 for further details.

effects, it is unlikely that the lag biases caused by BLR contamination are larger than the fiducial estimates presented here (see Figure 8). Future RM programs can test this result by specifically targeting the diffuse continuum and Hα emission, putting stronger constraints on their variability amplitudes and mean lags.

The systematic tendency for the *u, U, r,* and *R* band lags to sit above the fit in Figure 5 can therefore reasonably be explained by BLR contamination. In the case of the *u* and *U* bands, the offset from the fit to Equation 4 is large compared to the predicted lag (as well as the observational uncertainty), which supports our decision to exclude these data from the final model. On the other hand, the *r* and *R*-band offsets are much smaller, so the BLR bias probably makes little difference for our final model. Extending this reasoning to the *B, g,* and *V*-band filters, the BLR contamination is less than 10%, which would result in even smaller biases.

It is therefore unlikely that there are any important biases of the continuum lags in these bands, unless the diffuse continuum component (e.g., free-free emission or the Paschen continuum) makes a substantial contribution. This diffuse continuum component of the spectrum is unconstrained in our spectral decomposition, but it provides an intriguing possibility of explaining the downturn of the lag-wavelength relation in the *I* and *z* bands. The Paschen continuum begins at 8204 Å, between the *i* and *I* bands, so the true continuum lag-wavelength

relation may run through the UV and *Iz*-band lags, but underneath the lags of the other optical filters. The viability of this explanation requires significant contamination of the optical filters by diffuse BLR emission, which can potentially be estimated through photoionization modeling of the *HST* data or additional optical/near-IR observations.

5.3. *Accretion-Disk Size*

A geometrically thin, optically thick, irradiated accretion disk makes definite predictions about the observed lag-wavelength structure of the AGN. Here, we compare this model to the observed continuum lags, although we do not necessarily interpret the model parameters as indicative of physical conditions within the AGN. Full physical modeling of the AGN STORM data is deferred to future papers in this series (Starkey et al., in prep.; Kochanek et al., in prep.).

The disk is assumed to have a fixed aspect ratio with scale height much smaller than radius, and is heated internally by viscous dissipation and externally by a UV/X-ray source near the SMBH at a small height H above the disk. In such a scenario, the temperature profile is

$$T(R) = \left(\frac{3GM\dot{M}}{8\pi\sigma R^3} + \frac{(1-A)L_{\rm X}H}{4\pi\sigma R^3} \right)^{1/4}, \quad (8)$$

where M is the mass of the central SMBH, $\dot{M}$ is the mass accretion rate of the disk, R is the distance away from the black hole and central source of heating radiation, $L_{\rm X}$ is the luminosity of the heating radiation, and A is the albedo of the disk (Cackett et al. 2007). Here, we have ignored the inclination and the inner edge of the disk, as well as any relativistic effects. Inclination and relativity may have a small impact on the temperature profile, but the largest effect is caused by the inner edge, which reaches a maximum temperature and probably makes important contributions to emission at wavelengths < 2000 Å (Novikov & Thorne 1973). This introduces an error when comparing the *HST* lags to this model, although the effect is small relative to the UV–optical lags.

Identifying the temperature with a characteristic emission wavelength $T = Xhc/k\lambda$, where X is a multiplicative factor of order unity, and the radius with the light-travel time $R = c\tau$, we have

$$c\tau = \left(X\frac{k\lambda}{hc} \right)^{4/3} \left(\frac{3GM\dot{M}}{8\pi\sigma} + \frac{(1-A)L_{\rm X}H}{4\pi\sigma} \right)^{1/3}. \quad (9)$$

The factor X accounts for systematic issues in the conversion of T to λ for a given R, since a range of radii contributes to emission at λ. From the flux-weighted mean radius

$$\langle R \rangle = \frac{\int_{R_0}^{\infty} B(T(R))R^2\,dR}{\int_{R_0}^{\infty} B(T(R))R\,dR}, \quad (10)$$

we derive $X = 2.49$, where R_0 is the inner edge of the disk, $B(T(R))$ is the Planck function, and $T(R)$ is the temperature profile defined in Equation 8.[68]

If we measure τ relative to a reference time delay τ_0 of a light curve with effective wavelength λ_0, then this becomes

$$(\tau - \tau_0) = \frac{1}{c}\left(X\frac{k\lambda_0}{hc} \right)^{4/3} \left(\frac{3GM\dot{M}}{8\pi\sigma} + \frac{(1-A)L_{\rm X}H}{4\pi\sigma} \right)^{1/3} \left[\left(\frac{\lambda}{\lambda_0} \right)^{4/3} - 1 \right]. \quad (11)$$

Therefore, the parameter α in Equation 4 is related to the energy generation rate responsible for heating the disk, while β is predicted to be $4/3$. The absolute size of the disk at λ_0 can be measured by determining τ_0, which is inferred by assuming the corona is located at $\tau = 0$ and fitting the X-rays lags (in which case $\tau_0 = \alpha$).

We can only determine $\dot{M}$ indirectly through an estimate of the bolometric luminosity. We set $L_{\rm Bol} = \eta\dot{M}c^2$, where η is the radiative efficiency for converting rest mass into radiation, and $L_{\rm Bol}$ quantifies all emergent radiation from the AGN, including coronal X-rays (in this sense, our model differs from the typical Shakura & Sunyaev 1973 thin-disk model). A convenient parameterization of $L_{\rm Bol}$ is the Eddington ratio, $\dot{m}_{\rm E} = L_{\rm Bol}/L_{\rm Edd}$. We also simplify Equation 11 by taking $(1-A)L_{\rm X}H/R = \kappa GM\dot{M}/2R$, where κ is the local ratio of external to internal heating, assumed to be constant with radius.

The equation for α is then

$$\alpha = \frac{1}{c}\left(X\frac{k\lambda_0}{hc} \right)^{4/3} \left[\left(\frac{GM}{8\pi\sigma} \right) \left(\frac{L_{\rm Edd}}{\eta c^2} \right) (3+\kappa)\dot{m}_{\rm E} \right]^{1/3}. \quad (12)$$

A common choice for $\dot{m}_{\rm E}$ is 0.1, and we further assume that $\eta = 0.1$ and $\kappa = 1$ for our fiducial calculations (i.e., the X-rays and viscous heating contribute equal amounts of energy to the disk). For a 5.2×10^7 $M_\odot$ SMBH, these assumptions give $\alpha = 0.14$ day. If we increase the accretion rate by setting $\dot{m}_{\rm E} = 1$ and 10, then $\alpha = 0.30$ and 0.65 day, respectively. The lag-wavelength relation for these models is shown in Figure 5, and the curves for $\dot{m}_{\rm E} = 1$–10 bracket our fit to Equation 4 with $\alpha = 0.79 \pm 0.22$ days and $\beta = 0.99 \pm 0.14$. However, it is important to note that the disk probably does not remain geometrically thin at these high accretion rates, and the assumptions of the model do not hold in this regime (Jiang et al. 2014; Sądowski et al. 2014). Equation 12 is relatively insensitive to the ratio of external to internal heating—even if the X-rays contribute a negligible portion of the luminosity ($\kappa = 0$), α would only change by a factor of $(3/4)^{1/3}$.

In Paper II, we found $\alpha = 0.35 \pm 0.04$ day, somewhat smaller than in this study. The smaller value can be explained by correlations between α and β, shown in Figure 9. For the final analysis in Paper II, β was fixed to 4/3, and, if we do the same, we find $\alpha = 0.42 \pm 0.02$ day, in good agreement with Paper II. The fit with fixed β has $\chi^2/{\rm dof} = 1.42$, making the lower value of $\beta = 0.99 \pm 0.14$ statistically preferred. However, this result is driven by the flattening of the lags at the reddest wavelengths. If we exclude the I and z bands from the fit (as well as u and U), we find $\beta = 1.18 \pm 0.19$ and $\alpha = 0.58 \pm 0.20$ day with $\chi^2/{\rm dof} = 0.89$, while fixing $\beta = 4/3$ gives $\alpha = 0.45 \pm 0.02$ day and $\chi^2/{\rm dof} = 0.87$.

We therefore conclude that a reprocessing model can fit the data reasonably well but requires a much larger disk radius than predicted by standard thin-disk models. Fixing $\beta = 4/3$ (in order to match the theoretical temperature profile), our best-fit value of $\alpha = 0.42$ day is a factor of 3.0 larger than the standard prediction with $L/L_{\rm Edd} = 0.1$.

A sufficiently high accretion rate can account for this difference by increasing the size of the accretion disk. We note

[68] Alternative definitions of R exist. For example, a weighting function that better characterizes the radius responding to variable irradiation would replace Equation 8 with $T = T_0(R) + \frac{\partial B(T(R))}{\partial T}\frac{\delta T}{T}T$, and set $\frac{\delta T}{T}$ equal to a constant fractional temperature variation. This yields $X = 3.37$.

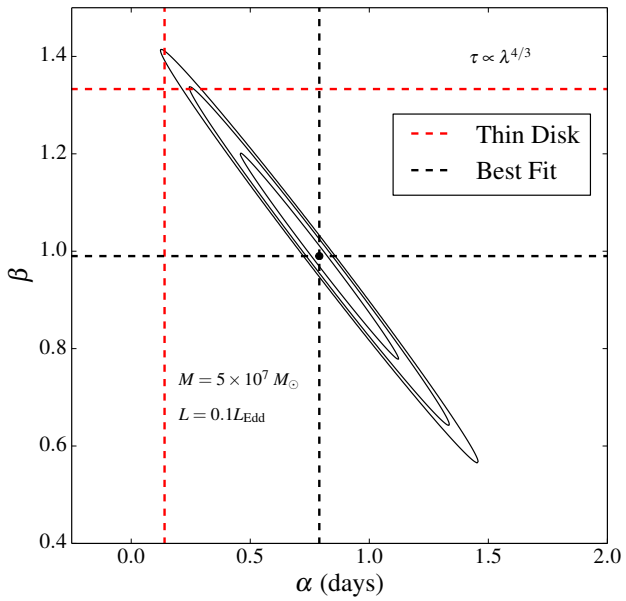

Figure 9. Probability distribution for the parameters α and β of our best-fit model. The contours show the 68, 95, and 99% confidence regions.

that uncertainties in the SMBH mass do not require $\dot{m}_{\rm E}$ to be larger than one, since $\dot{m}_{\rm E} \propto \alpha^3/M^2$ (Equation 12), while the SMBH mass may be up to 1.75 times larger at 3σ than our adopted value. This would still require $\dot{m}_{\rm E}$ to be somewhere in the range $\sim$0.1–1. On the other hand, a comparison of $\dot{m}_{\rm E}$ can be made assuming a thin-disk spectrum and using the observed optical luminosity (e.g., Collin et al. 2002; Netzer 2013, Equation 4.53). From our spectral decompositions, we estimate that $\lambda F_\lambda = 4.57 \times 10^{-11}$ erg cm^{-2} s^{-1} at 5100 Å, which yields $\dot{m}_{\rm E} = 0.05$ at a disk inclination of $\cos i = 0.63$ and radiative efficiency $\eta = 0.1$. The accretion rate cannot be much higher (unless the disk is seen very edge-on), so this result implies that a standard thin-disk model cannot account for both the observed time delays and the monochromatic luminosity at 5100 Å.

The large disk size found here corroborates the results from Paper II and other recent RM studies (Shappee et al. 2014; McHardy et al. 2014; Lira et al. 2015). The measurements of large disk radii are also in good agreement with the sizes inferred from gravitational microlensing experiments (see Figure 6 in Paper II, as well as Poindexter et al. 2008; Morgan et al. 2010; Mosquera et al. 2013). Other sources of tension with the thin-disk/continuum reprocessing model are (1) the weak correlation between the X-ray light curves and UV/optical light curves (Paper II), and (2) the possible flattening of the lags at the longest wavelengths. The latter phenomenon might contain information about the outer edge of the disk, or perhaps be explained by contaminating emission from BLR material along the line of sight (Korista & Goad 2001), and/or emission from the inner edge of the near side of the obscuring torus (Goad et al. 2012).

The intriguing result that accretion disks in AGN might be larger than predicted by standard thin-disk theory depends on only a handful of lensed quasars and three RM AGN (NGC 5548, NGC 2617, and MCG-6-30-15; Shappee et al. 2014; Lira et al. 2015). Thus, it is important to carry out further continuum RM experiments, in order to establish if this is a robust result and determine what physical parameters govern the disk size. It is also possible to recast this kind of experiment in more direct scaling relations, such as the lag-luminosity relations of Sergeev et al. (2005), which can be derived from thin-disk theory (both the disk size and luminosity scale with accretion rate and black hole mass). In fact, the Sergeev et al. (2005) lag-luminosity relations lie somewhat above the prediction for standard thin-disk theory, and the lags reported here would be $\sim$1 day below these relations in most bands. However, the relations are largely based on unresolved lags and have very large uncertainties, so they do not put an interesting constraint on model predictions. A larger sample of AGN with continuum lags derived to the same precision as this study would provide an interesting measurement of the lag-luminosity relations, which can provide a further test of thin-disk theory and establish if larger disk sizes are generic properties of the AGN population.

6. SUMMARY

We have presented results for a ground-based, broad-band photometric monitoring campaign of NGC 5548. Our light curves are of very high quality, achieving cadences of $\lesssim 1$ day in nine optical bands over an entire observing season. Using full optical-wavelength spectra and synthetic photometry, we estimated the relative contribution of host-galaxy starlight, AGN continuum emission, Balmer continuum, and line emission from the BLR to the observed light curves. Our main results are as follows.

1 Significant time delays are detected between the far-UV, near-UV, and optical broad-band light curves. The delay between emission at 1367 Å and 2600 Å is less than 1 day, and the delay between emission at 1367 Å and the V band is about 2 days. Such large time delays are comparable to, and sometimes greater than, the lags of the high-ionization-state emission lines, suggesting that the continuum-emitting source is of a physical size approximately equal to the inner BLR.

2 If similar interband continuum lags exist in other AGN, this also suggests that the size of the BLR is 11–37% larger than would be inferred from optical data alone. However, there do not appear to be other significant systematic effects associated with the optical light curves, and RM SMBH masses are not affected by this result.

3 There is some contamination of the broad-band light curves by BLR emission, with 19% of the u and U bands attributable to the Balmer continuum, and 15–20% of the r and R bands attributable to Hα. The impact of BLR emission on the observed u and U-band lags is $\sim$0.6–1.2 days, but is probably unimportant in the r and R bands. This justifies our decision to exclude the u and U-band lags from our final analysis.

4 The trend of lag with wavelength is broadly consistent with the prediction for continuum reprocessing by a geometrically thin accretion disk with $\tau \propto \lambda^{4/3}$. However, the size of the disk is a factor of 3 larger than the prediction for standard thin-disk theory, assuming that $L = 0.1\,L_{\rm Edd}$. This result appears to corroborate those from other continuum RM projects and gravitational microlensing studies. Further investigations of the accretion-disk structure will benefit from physical modeling of the AGN STORM light curves, and several such studies are planned for upcoming papers in this series (Starkey et al., in prep.; Kochanek et al., in prep.).

The LBT is an international collaboration among institutions in the United States, Italy and Germany. LBT Corporation partners are: The Ohio State University, and The Research Corporation, on behalf of The University of Notre Dame, University of Minnesota and University of Virginia; The University of Arizona on behalf of the Arizona university system; Istituto Nazionale di Astrofisica, Italy; LBT Beteiligungsgesellschaft, Germany, representing the Max-Planck Society, the Astrophysical Institute Potsdam, and Heidelberg University.

This paper used data obtained with the MODS spectrographs built with funding from National Science Foundation (NSF) grant AST-9987045 and the NSF Telescope System Instrumentation Program (TSIP), with additional funds from the Ohio Board of Regents and the Ohio State University Office of Research. This paper made use of the `modsIDL` spectral data reduction pipeline developed in part with funds provided by NSF Grant AST - 1108693.

The Liverpool Telescope is operated on the island of La Palma by Liverpool John Moores University in the Spanish Observatorio del Roque de los Muchachos of the Instituto de Astrofisica de Canarias with financial support from the UK Science and Technology Facilities Council.

KAIT and its ongoing operation were made possible by donations from Sun Microsystems, Inc., the Hewlett-Packard Company, AutoScope Corporation, Lick Observatory, the NSF, the University of California, the Sylvia and Jim Katzman Foundation, and the TABASGO Foundation. Research at Lick Observatory is partially supported by a generous gift from Google.

Support for *HST* program number GO-13330 was provided by NASA through a grant from the Space Telescope Science Institute, which is operated by the Association of Universities for Research in Astronomy, Inc., under NASA contract NAS5-26555. M.M.F., G.D.R., B.M.P., C.J.G., and R.W.P. are grateful for the support of the NSF through grant AST-1008882 to The Ohio State University. A.J.B. and L.P. have been supported by NSF grant AST-1412693. A.V.F. and W.-K.Z. are grateful for financial assistance from NSF grant AST-1211916, the TABASGO Foundation, and the Christopher R. Redlich Fund. M.C. Bentz gratefully acknowledges support through NSF CAREER grant AST-1253702 to Georgia State University. M.C. Bottorff acknowledges HHMI for support through an undergraduate science education grant to Southwestern University. K.D.D. is supported by an NSF Fellowship awarded under grant AST-1302093. R.E. gratefully acknowledges support from NASA under awards NNX13AC26G, NNX13AC63G, and NNX13AE99G. J.M.G. gratefully acknowledges support from NASA under award NNH13CH61C. P.B.H. is supported by NSERC. M.I. acknowledges support from the Creative Initiative program, No. 2008-0060544, of the National Research Foundation of Korea (NRFK) funded by the Korean government (MSIP). M.D.J. acknowledges NSF grant AST-0618209 used for obtaining the 0.91 m telescope at WMO. SRON is financially supported by NWO, the Netherlands Organization for Scientific Research. B.C.K. is partially supported by the UC Center for Galaxy Evolution. C.S.K. acknowledges the support of NSF grant AST-1009756. D.C.L. acknowledges support from NSF grants AST-1009571 and AST-1210311, under which part of this research (photometric observations collected at MLO) was carried out. We thank Nhieu Duong, Harish Khandrika, Richard Mellinger, J. Chuck Horst, Steven Armen, and Eddie Garcia for assistance with the MLO observations. P.L. acknowledges support from Fondecyt grant #1120328. A.P. acknowledges support from a NSF graduate fellowship, a UCSB Dean's Fellowship, and a NASA Einstein Fellowship. J.S.S. acknowledges CNPq, National Council for Scientific and Technological Development (Brazil) for partial support and The Ohio State University for warm hospitality. T.T. has been supported by NSF grant AST-1412315. T.T. and B.C.K. acknowledge support from the Packard Foundation in the form of a Packard Research Fellowship to T.T.; also, T.T. thanks the American Academy in Rome and the Observatory of Monteporzio Catone for kind hospitality. The Dark Cosmology Centre is funded by the Danish National Research Foundation. M.V. gratefully acknowledges support from the Danish Council for Independent Research via grant no. DFF–4002-00275. J.-H.W. acknowledges support by the National Research Foundation of Korea (NRF) grant funded by the Korean government (No. 2010-0027910). E.D.B. is supported by Padua University through grants 60A02-5857/13, 60A02-5833/14, 60A02-4434/15, and CPDA133894. K.H. acknowledges support from STFC grant ST/M001296/1. S.A.K. thanks Dr. I. A. Rakhimov, the Director of Svetloe Observatory, for his support and hospitality.

This research has made use of the NASA/IPAC Extragalactic Database (NED), which is operated by the Jet Propulsion Laboratory, California Institute of Technology, under contract with NASA.

REFERENCES

Abazajian, K. N., Adelman-McCarthy, J. K., Agüeros, M. A., et al. 2009, ApJS, 182, 543
Abramowicz, M. A., Czerny, B., Lasota, J. P., & Szuszkiewicz, E. 1988, ApJ, 332, 646
Alard, C., & Lupton, R. H. 1998, ApJ, 503, 325
Arévalo, P., Uttley, P., Lira, P., et al. 2009, MNRAS, 397, 2004
Barth, A. J., Bennert, V. N., Canalizo, G., et al. 2015, ApJS, 217, 26
Bentz, M. C., & Katz, S. 2015, PASP, 127, 67
Bentz, M. C., Walsh, J. L., Barth, A. J., et al. 2009, ApJ, 705, 199
—. 2010a, ApJ, 716, 993
Bentz, M. C., Horne, K., Barth, A. J., et al. 2010b, ApJ, 720, L46
Bentz, M. C., Denney, K. D., Grier, C. J., et al. 2013, ApJ, 767, 149
Blandford, R. D., & McKee, C. F. 1982, ApJ, 255, 419
Breedt, E., Arévalo, P., McHardy, I. M., et al. 2009, MNRAS, 394, 427
Breedt, E., McHardy, I. M., Arévalo, P., et al. 2010, MNRAS, 403, 605
Brosch, N., Polishook, D., Shporer, A., et al. 2008, Ap&SS, 314, 163
Bruzual, G., & Charlot, S. 2003, MNRAS, 344, 1000
Burbidge, E. M. 1967, ARA&A, 5, 399
Cackett, E. M., Gültekin, K., Bentz, M. C., et al. 2015, ApJ, 810, 86
Cackett, E. M., Horne, K., & Winkler, H. 2007, MNRAS, 380, 669
Cardelli, J. A., Clayton, G. C., & Mathis, J. S. 1989, ApJ, 345, 245
Chakrabarti, S., & Titarchuk, L. G. 1995, ApJ, 455, 623
Chelouche, D. 2013, ApJ, 772, 9
Chelouche, D., & Zucker, S. 2013, ApJ, 769, 124
Chiang, J., & Murray, N. 1996, ApJ, 466, 704
Cid Fernandes, R., Gu, Q., Melnick, J., et al. 2004, MNRAS, 355, 273
Clavel, J., Reichert, G. A., Alloin, D., et al. 1991, ApJ, 366, 64
Collier, S. J., Horne, K., Kaspi, S., et al. 1998, ApJ, 500, 162
Collin, S., Boisson, C., Mouchet, M., et al. 2002, A&A, 388, 771
Collin-Souffrin, S. 1987, A&A, 179, 60
De Rosa, G., Peterson, B. M., Ely, J., et al. 2015, ApJ, 806, 128 (Paper I)
Denney, K. D. 2012, ApJ, 759, 44
Denney, K. D., Peterson, B. M., Dietrich, M., Vestergaard, M., & Bentz, M. C. 2009, ApJ, 692, 246
Denney, K. D., Peterson, B. M., Pogge, R. W., et al. 2010, ApJ, 721, 715
Dietrich, M., Hamann, F., Shields, J. C., et al. 2002, ApJ, 581, 912
Edelson, R., Vaughan, S., Malkan, M., et al. 2014, ApJ, 795, 2
Edelson, R., Gelbord, J. M., Horne, K., et al. 2015, ApJ, 806, 129 (Paper II)
Eracleous, M., Lewis, K. T., & Flohic, H. M. L. G. 2009, New A Rev., 53, 133
Filippenko, A. V., Li, W. D., Treffers, R. R., & Modjaz, M. 2001, in Astronomical Society of the Pacific Conference Series, Vol. 246, IAU Colloq. 183: Small Telescope Astronomy on Global Scales, ed. B. Paczynski, W.-P. Chen, & C. Lemme, 121
Fukugita, M., Ichikawa, T., Gunn, J. E., et al. 1996, AJ, 111, 1748
Gehrels, N., Chincarini, G., Giommi, P., et al. 2004, ApJ, 611, 1005
Goad, M. R., Korista, K. T., & Ruff, A. J. 2012, MNRAS, 426, 3086
Green, J. C., Froning, C. S., Osterman, S., et al. 2012, ApJ, 744, 60
Grier, C. J., Martini, P., Watson, L. C., et al. 2013a, ApJ, 773, 90
Grier, C. J., Peterson, B. M., Horne, K., et al. 2013b, ApJ, 764, 47
Haardt, F., & Maraschi, L. 1991, ApJ, 380, L51

Hartman, J. D., Bakos, G., Stanek, K. Z., & Noyes, R. W. 2004, AJ, 128, 1761
Higginbottom, N., Proga, D., Knigge, C., et al. 2014, ApJ, 789, 19
Hill, J. M., Green, R. F., Ashby, D. S., et al. 2010, in Society of Photo-Optical Instrumentation Engineers (SPIE) Conference Series, Vol. 7733, SPIE, 0
Horne, K., Peterson, B. M., Collier, S. J., & Netzer, H. 2004, PASP, 116, 465
Horne, K., Welsh, W. F., & Peterson, B. M. 1991, ApJ, 367, L5
Jiang, Y.-F., Stone, J. M., & Davis, S. W. 2014, ApJ, 796, 106
Kasliwal, V. P., Vogeley, M. S., & Richards, G. T. 2015, MNRAS, 451, 4328
Kaspi, S., Smith, P. S., Netzer, H., et al. 2000, ApJ, 533, 631
Kelly, B. C., Bechtold, J., & Siemiginowska, A. 2009, ApJ, 698, 895
Kishimoto, M., Antonucci, R., Boisson, C., & Blaes, O. 2004, MNRAS, 354, 1065
Komatsu, E., Smith, K. M., Dunkley, J., et al. 2011, ApJS, 192, 18
Koratkar, A., & Blaes, O. 1999, PASP, 111, 1
Korista, K. T., & Goad, M. R. 2001, ApJ, 553, 695
—. 2004, ApJ, 606, 749
Krolik, J. H., Horne, K., Kallman, T. R., et al. 1991, ApJ, 371, 541
Laor, A., Jannuzi, B. T., Green, R. F., & Boroson, T. A. 1997, ApJ, 489, 656
Li, Y.-R., Wang, J.-M., Ho, L. C., Du, P., & Bai, J.-M. 2013, ApJ, 779, 110
Lira, P., Arévalo, P., Uttley, P., McHardy, I. M. M., & Videla, L. 2015, MNRAS, 454, 368
MacLeod, C. L., Ivezić, Ž., Kochanek, C. S., et al. 2010, ApJ, 721, 1014
Maoz, D., Markowitz, A., Edelson, R., & Nandra, K. 2002, AJ, 124, 1988
Marshall, K., Ryle, W. T., & Miller, H. R. 2008, ApJ, 677, 880
McHardy, I. M., Cameron, D. T., Dwelly, T., et al. 2014, MNRAS, 444, 1469
Mehdipour, M., Kaastra, J. S., Kriss, G. A., et al. 2015, A&A, 575, A22
Morgan, C. W., Kochanek, C. S., Morgan, N. D., & Falco, E. E. 2010, ApJ, 712, 1129
Mosquera, A. M., Kochanek, C. S., Chen, B., et al. 2013, ApJ, 769, 53
Narayan, R., & Yi, I. 1995, ApJ, 452, 710
Netzer, H. 2013, The Physics and Evolution of Active Galactic Nuclei
Novikov, I. D., & Thorne, K. S. 1973, in Black Holes (Les Astres Occlus), ed. C. Dewitt & B. S. Dewitt, 343–450
Onken, C. A., Ferrarese, L., Merritt, D., et al. 2004, ApJ, 615, 645
Pancoast, A., Brewer, B. J., Treu, T., et al. 2014, MNRAS, 445, 3073
Park, D., Kelly, B. C., Woo, J.-H., & Treu, T. 2012a, ApJS, 203, 6
Park, D., Woo, J.-H., Treu, T., et al. 2012b, ApJ, 747, 30
Pei, L., Barth, A. J., Aldering, G. S., et al. 2014, ApJ, 795, 38
Peterson, B. M. 1993, PASP, 105, 247
Peterson, B. M. 2001, in Advanced Lectures on the Starburst-AGN, ed. I. Aretxaga, D. Kunth, & R. Mújica, 3
—. 2014, Space Sci. Rev., 183, 253
Peterson, B. M., Balonek, T. J., Barker, E. S., et al. 1991, ApJ, 368, 119
Peterson, B. M., Ferrarese, L., Gilbert, K. M., et al. 2004, ApJ, 613, 682
Pogge, R. W., Atwood, B., Brewer, D. F., et al. 2010, in Society of Photo-Optical Instrumentation Engineers (SPIE) Conference Series, Vol. 7735, SPIE, 0
Poindexter, S., Morgan, N., & Kochanek, C. S. 2008, ApJ, 673, 34
Poole, T. S., Breeveld, A. A., Page, M. J., et al. 2008, MNRAS, 383, 627
Press, W. H., Teukolsky, S. A., Vetterling, W. T., & Flannery, B. P. 2002, Numerical recipes in C++ : the art of scientific computing
Proga, D., & Kallman, T. R. 2004, ApJ, 616, 688
Proga, D., & Kurosawa, R. 2010, in Astronomical Society of the Pacific Conference Series, Vol. 427, Accretion and Ejection in AGN: a Global View, ed. L. Maraschi, G. Ghisellini, R. Della Ceca, & F. Tavecchio, 41
Rodríguez-Pascual, P. M., Alloin, D., Clavel, J., et al. 1997, ApJS, 110, 9
Sakata, Y., Minezaki, T., Yoshii, Y., et al. 2010, ApJ, 711, 461
Sądowski, A., Narayan, R., McKinney, J. C., & Tchekhovskoy, A. 2014, MNRAS, 439, 503
Schlafly, E. F., & Finkbeiner, D. P. 2011, ApJ, 737, 103
Schlegel, D. J., Finkbeiner, D. P., & Davis, M. 1998, ApJ, 500, 525
Sergeev, S. G., Doroshenko, V. T., Golubinskiy, Y. V., Merkulova, N. I., & Sergeeva, E. A. 2005, ApJ, 622, 129
Shakura, N. I., & Sunyaev, R. A. 1973, A&A, 24, 337
Shappee, B. J., Prieto, J. L., Grupe, D., et al. 2014, ApJ, 788, 48
Shields, G. A. 1978, Nature, 272, 706
Skielboe, A., Pancoast, A., Treu, T., et al. 2015, MNRAS, 454, 144
Steele, I. A., Smith, R. J., Rees, P. C., et al. 2004, in Society of Photo-Optical Instrumentation Engineers (SPIE) Conference Series, Vol. 5489, Ground-based Telescopes, ed. J. M. Oschmann, Jr., 679–692
Sun, W.-H., & Malkan, M. A. 1989, ApJ, 346, 68
Telfer, R. C., Zheng, W., Kriss, G. A., & Davidsen, A. F. 2002, ApJ, 565, 773
Troyer, J., Starkey, D., Cackett, E. M., et al. 2016, MNRAS, 456, 4040
Uttley, P., Edelson, R., McHardy, I. M., Peterson, B. M., & Markowitz, A. 2003, ApJ, 584, L53
Vaughan, S., Edelson, R., Warwick, R. S., & Uttley, P. 2003, MNRAS, 345, 1271
Vestergaard, M., & Peterson, B. M. 2005, ApJ, 625, 688
Vestergaard, M., & Wilkes, B. J. 2001, ApJS, 134, 1
Wanders, I., Peterson, B. M., Alloin, D., et al. 1997, ApJS, 113, 69
Welsh, W. F. 1999, PASP, 111, 1347
Woo, J.-H., Schulze, A., Park, D., et al. 2013, ApJ, 772, 49
Woo, J.-H., Yoon, Y., Park, S., Park, D., & Kim, S. C. 2015, ApJ, 801, 38
Woo, J.-H., Treu, T., Barth, A. J., et al. 2010, ApJ, 716, 269
Zu, Y., Kochanek, C. S., Kozłowski, S., & Udalski, A. 2013, ApJ, 765, 106
Zu, Y., Kochanek, C. S., & Peterson, B. M. 2011, ApJ, 735, 80

APPENDIX—ON INTERPOLATION

Interpolating a light curve requires some assumed model, which may be more or less sophisticated. For example, linear interpolation is a very simple method. However, linear interpolation assumes no additional variability between sampled epochs, and this is known to be an incorrect description of AGN light curves on nightly timescales. The DRW allows for intrinsic variations between sampled epochs by modeling the data covariance, from which we can make a better guess as to what the continuum is doing between the observations and, moreover, assign a meaningful error bar to the prediction.

Figure 10 shows the linear interpolation model of a portion of the *R*-band continuum light curve of NGC 5548 (the *R* band was chosen because it has large gaps). By definition, the linearly interpolated model goes exactly through every data point. It has an "error snake" that matches the error bars of the data at a sampled epoch and can shrink between data points. This is because the model includes only measurement noise, so the error in the model is smallest somewhere in between the data points where it best averages the two measurements. Defining the fractional distance between the interpolated epoch t_j and the data points t_i and t_{i+1} as $x = (t_j - t_i)/(t_{i+1} - t_i)$ so $0 < x < 1$, the error snake for linear interpolation at t_j is given by $\sigma^2(t_j) = (1-x)^2\sigma(t_i)^2 + x^2\sigma(t_{i+1})^2$, which is smallest at $x = 1/2$ for $\sigma(t_i) = \sigma(t_{i+1})$. Because it is required to go through the data points, there are regions of the model light curve (e.g., near day 6740) where the model rapidly "oscillates" in order to pass through nearby points. The principal problems with the linear interpolation model are therefore (1) that the model light curve has much more structure than it should when the light curve is well sampled, and (2) the error snake can decrease in width the farther it gets from the actual data points.

`JAVELIN` uses a covariance model to estimate the statistical properties of light curves. We have used the DRW model because it is simple and describes quasar variability on the timescales sampled by the data (Kelly et al. 2009; MacLeod et al. 2010; Zu et al. 2013). The middle panel of Figure 10 shows the DRW model for the same region of the NGC 5548 light curve. There are two important qualitative changes. First, unlike linear interpolation, the model no longer has to go through the data points. For example, in the region near day 6740, the DRW model is quite smooth because it has decided (statistically) that the three points with larger uncertainties should be viewed as measurement fluctuations rather than intrinsic variability. In contrast, there is the region near day 6758 where the error bars on the points forming a "triangle" are small enough that the model tracks the data points more or less like the linear interpolated model. The second difference is that the error snakes generally grow in the gaps between the data points. This is because `JAVELIN` is accounting for the intrinsic variability as well as the measurement errors. The more distant an actual measurement, the greater the expected variance in the underlying light curve. If the measurement errors are very large (e.g., the point near day 6785), then the error snake can be smaller than the measurement errors because the model predicts the expected range of the light curve better than it was actually measured.

There is evidence from high-cadence *Kepler* light curves that the DRW model overestimates the variability power on short (subweek) timescales (Edelson et al. 2014; Kasliwal et al. 2015). Although the DRW is therefore an incorrect model on short timescales, our data have very different properties from the *Kepler* light curves (1 day cadence instead of 30 minute cadence and $\sim$0.5–1.0% uncertainties instead of $\sim$0.1%), and useful results can be found as long as the covariance model is a reasonable approximation of the true data covariance. An analogy exists here with optimal (Weiner) filters—quoting from *Numerical Recipes* (Press et al. 2002, Chapter 13.3, page 651), "In other words, even a fairly crudely determined optimal filter can give excellent results when applied to data." This is because errors in the covariance model only become significant when the differences are larger than the noise σ. For two structure-function amplitudes SF_1 and SF_2, the fractional changes in the models are of order $|SF_1^2 - SF_2^2|/\sigma^2$. Unless the light curve is of sufficiently high quality to measure the structure function on a given timescale, we will not have any noticeable effects from making even order unity errors in the structure function on those timescales. To go back to the optimal filtering analogy, we get 90% of the gains from being in the ball park, and very little extra from being perfectly correct.

We can illustrate this by using the "Kepler-exponential" model from Zu et al. (2013), which includes a timescale $\tau_{\rm cut}$ below which the power spectrum is cut off. The Kepler-exponential model was designed to explore the *Kepler* results (that AGN light curves have suppressed power on short timescales), and is available as an option in `JAVELIN` (the `JAVELIN` algorithm can use any covariance model desired). The Kepler-exponential model of the *R*-band light curve is shown in Figure 10 with a power cutoff timescale $\tau_{\rm cut} = 1$ day. As expected, it is very difficult to see any differences. The easiest one to spot is that the error snake grows a little faster as it moves away from a data point in the DRW model because it has some extra small-scale power (which actually makes the DRW model a more conservative choice). If we steadily increase $\tau_{\rm cut}$ above 1 day, the Kepler-exponential models start to fit the data poorly because they have too little short-timescale power.

We compared the DRW and Kepler-exponential models quantitatively by assessing how well they predict the data. We generated predicted values for each data point from the interpolation scheme described in §2.3 for each model, and then calculated

$$\chi^2/{\rm dof} = \frac{1}{N-k}\sum_i^N \frac{(y_i - m_i)^2}{\sigma_i^2},$$

where N is the number of data points, k is the number of parameters, y are the data, m are the interpolated values, and σ are the uncertainties (on the data only—the uncertainty on the interpolation is necessarily consistent with the data). We use all data points when calculating the interpolation, and so we emphasize that this definition has nothing to do with the probability of the model: linear interpolation would force this value of $\chi^2/{\rm dof} = 0$, even though it is certainly not correct. Rather, this definition gives an estimate of the consistency of the data with the model. For these fits, we again fixed $\tau_{\rm cut}$ to 1 day.

Table 7 summarizes these results. The two models produce interpolations that are virtually indistinguishable (i.e., nearly equal $\chi^2/{\rm dof}$). Increasing $\tau_{\rm cut}$ to 10 days increases $\chi^2/{\rm dof}$ by a small amount (up to 0.06), and as $\tau_{\rm cut}$ approaches 0 days, we recover the DRW. This means that there is no quantitative advantage to using a random process with suppressed short-timescale power—our data are not good enough to see this effect.

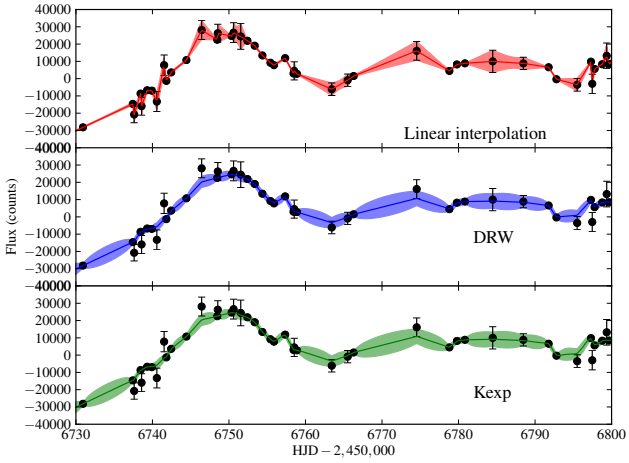

Figure 10. Data and models for the *R*-band continuum in NGC 5548. Top panel: Linear interpolation model. Middle panel: DRW model. Bottom panel: "Kepler-exponential model," which is DRW with a drop in power on the shortest timescales ($\tau_{\rm cut} = 1$ day).

Table 7
Comparison of DRW and Kepler-Exponential Interpolations.

Band	χ^2/dof (DRW)	χ^2/dof (Kexp)
u	0.37	0.34
B	0.29	0.29
g	0.33	0.31
V	0.65	0.73
r	0.40	0.40
R	0.41	0.41
i	0.23	0.22
I	0.28	0.26
z	0.27	0.26

Table 8
Optical Continuum Light Curves

Filter	HJD −2,400,000	F_λ (10^{-15}erg cm^{-2} s^{-1} Å^{-1})	σ_{F_λ}	Telescope ID (as in Table 1)	Differential Counts (DC) (reference counts)	error DC (reference counts)
u	56684.78184	21.609	0.0801	LT	-34438.0	1292.5
u	56685.78986	22.194	0.0651	LT	-24994.0	1050.5
u	56686.774	21.932	0.0439	LT	-29223.0	707.5
u	56689.01575	20.353	2.2099	LCOGT1	-54689.0	35642.0
u	56692.95591	20.373	0.7486	LCOGT1	-54377.0	12074.0
u	56693.79261	21.677	0.0441	LT	-33330.0	710.91
u	56694.77316	21.599	0.0799	LT	-34592.0	1289.4
u	56695.71256	21.757	0.0512	LT	-32054.0	825.29
u	56696.73102	22.242	0.0424	LT	-24221.0	683.47

Table 8 — *Continued*

Filter	HJD $-2,400,000$	F_λ (10^{-15}erg cm^{-2} s^{-1} Å^{-1})	σ_{F_λ}	Telescope ID (as in Table 1)	Differential Counts (DC) (reference counts)	error DC (reference counts)
u	56696.98202	22.452	1.8008	LCOGT1	-20835.0	29045.0
u	56697.75985	22.883	0.054	LT	-13884.0	870.58
u	56698.61098	23.247	0.3089	LCOGT2	-8016.1	4982.8
u	56698.7205	23.002	0.0476	LT	-11961.0	768.36
u	56699.7161	22.876	0.0945	LT	-14005.0	1523.4
u	56700.69467	23.071	0.0887	LT	-10858.0	1431.4
u	56701.56783	22.122	0.0595	LT	-26167.0	959.08
u	56701.8229	24.225	1.715	LCOGT1	7751.7	27661.0
u	56702.64141	22.726	0.1757	LT	-16426.0	2834.4
u	56703.01636	24.725	1.5059	LCOGT1	15821.0	24288.0
u	56703.93372	24.755	1.3439	LCOGT1	16306.0	21675.0
u	56704.83904	23.187	0.9763	LCOGT1	-8980.7	15747.0
u	56705.95302	26.157	1.0671	LCOGT1	38921.0	17211.0
u	56706.98256	22.716	1.6374	LCOGT1	-16586.0	26409.0
u	56708.02483	22.756	1.3991	LCOGT1	-15937.0	22565.0
u	56709.82892	21.826	1.3644	LCOGT1	-30931.0	22006.0
u	56710.66492	22.075	0.0448	LT	-26926.0	722.82
u	56711.01767	22.089	1.5052	LCOGT1	-26694.0	24277.0
u	56711.6892	21.863	0.169	LT	-30343.0	2724.9
u	56711.84103	21.701	1.367	LCOGT1	-32958.0	22048.0
u	56713.72546	21.34	0.0784	LT	-38778.0	1264.7
u	56713.83389	21.865	1.7049	LCOGT1	-30300.0	27497.0
u	56714.72664	21.09	0.0375	LT	-42798.0	605.32
u	56715.91324	20.072	1.0519	LCOGT1	-59232.0	16966.0
u	56716.65527	20.167	0.0578	LT	-57688.0	932.81
u	56717.72878	19.664	0.0674	LT	-65810.0	1086.5
u	56717.96153	17.23	2.0304	LCOGT1	-105060.0	32747.0
u	56718.66619	18.798	0.0599	LT	-79770.0	965.41
u	56719.7146	19.024	0.0434	LT	-76123.0	699.33
u	56721.70947	17.383	0.0695	LT	-102590.0	1121.1
u	56722.73342	17.13	0.0715	LT	-106670.0	1152.7
u	56723.56689	16.783	0.0593	LT	-112270.0	956.44
u	56725.5304	16.218	0.0427	LT	-121380.0	688.0
u	56728.5717	16.711	0.0564	LT	-113440.0	908.88
u	56729.49062	16.266	0.0529	LT	-120610.0	852.89
u	56730.53356	16.813	0.0527	LT	-111780.0	849.97
u	56730.82566	17.027	1.02	LCOGT1	-108330.0	16452.0
u	56732.48996	16.453	0.0715	LT	-117600.0	1152.5
u	56733.48023	16.586	0.0699	LT	-115450.0	1126.8
u	56733.79543	16.871	0.6776	LCOGT1	-110850.0	10929.0
u	56735.85918	16.879	1.6934	LCOGT1	-110730.0	27312.0
u	56736.4999	19.048	0.0613	LT	-75738.0	989.01
u	56736.77891	19.526	1.0602	LCOGT1	-68035.0	17100.0
u	56737.48474	19.78	0.0566	LT	-63932.0	913.05
u	56738.59899	20.516	0.07	LT	-52063.0	1129.6
u	56740.61291	22.85	0.0698	LT	-14418.0	1126.4
u	56740.85129	20.833	2.5729	LCOGT1	-46956.0	41497.0
u	56741.60712	22.579	0.0797	LT	-18787.0	1286.1
u	56741.7108	21.33	1.8256	LCOGT1	-38927.0	29444.0
u	56742.64716	22.899	0.096	LT	-13629.0	1548.4
u	56743.59134	24.381	0.0661	LT	10269.0	1066.1
u	56744.53369	24.168	0.0776	LT	6841.0	1250.9
u	56744.54996	23.15	0.3592	LCOGT2	-9582.2	5794.1
u	56744.69283	23.546	1.7893	LCOGT1	-3194.5	28859.0
u	56746.75457	25.167	1.2237	LCOGT1	22957.0	19736.0
u	56748.7371	22.943	1.7386	LCOGT1	-12911.0	28042.0
u	56749.74633	24.36	1.2729	LCOGT1	9930.9	20530.0
u	56752.57749	25.269	0.0641	LT	24590.0	1033.6
u	56753.57247	24.566	0.0632	LT	13252.0	1019.0
u	56754.55015	23.137	0.0607	LT	-9791.1	978.79
u	56755.55972	22.095	0.0731	LT	-26592.0	1178.6
u	56755.97603	21.882	0.7433	LCOGT1	-30034.0	11988.0
u	56756.50703	21.821	0.0807	LT	-31023.0	1301.4
u	56757.47732	24.341	0.4983	LCOGT2	9623.1	8037.0
u	56759.80043	23.65	1.3506	LCOGT1	-1519.2	21784.0
u	56761.59774	21.636	0.0625	LT	-33993.0	1008.4
u	56762.82444	21.329	1.6439	LCOGT1	-38955.0	26514.0
u	56763.50473	21.888	0.2834	LT	-29938.0	4570.5
u	56763.74795	23.439	1.1814	LCOGT1	-4914.3	19054.0
u	56764.81297	21.482	1.4967	LCOGT1	-36488.0	24139.0
u	56765.57793	22.252	0.0535	LT	-24062.0	863.58
u	56769.51254	22.955	0.0557	LT	-12724.0	898.92
u	56770.52188	23.121	0.0605	LT	-10055.0	976.29
u	56771.50651	23.754	0.0613	LT	158.88	988.24
u	56772.49318	23.681	0.0749	LT	-1015.0	1207.7
u	56772.81537	22.652	1.9586	LCOGT1	-17611.0	31589.0
u	56774.66833	24.13	0.0544	LT	6218.4	877.32
u	56774.75672	24.38	2.4643	LCOGT1	10259.0	39745.0

Table 8 — *Continued*

Filter	HJD $-2,400,000$	F_λ (10^{-15}erg cm^{-2} s^{-1} Å^{-1})	σ_{F_λ}	Telescope ID (as in Table 1)	Differential Counts (DC) (reference counts)	error DC (reference counts)
u	56775.54352	24.081	0.0743	LT	5428.5	1197.9
u	56777.5254	24.293	0.0624	LT	8862.8	1005.7
u	56778.49249	24.166	0.0623	LT	6811.4	1004.7
u	56779.39786	24.066	0.4417	LCOGT2	5198.9	7123.3
u	56779.48233	24.009	0.0652	LT	4267.3	1051.5
u	56779.82162	23.922	1.6181	LCOGT1	2878.0	26097.0
u	56780.48978	24.177	0.0615	LT	6988.0	992.32
u	56780.80668	22.426	1.7734	LCOGT1	-21254.0	28602.0
u	56781.77199	23.784	1.6667	LCOGT1	648.49	26882.0
u	56784.43632	23.946	0.0608	LT	3252.5	981.26
u	56785.47099	24.275	0.0626	LT	8561.1	1009.8
u	56786.47789	23.891	0.0685	LT	2375.6	1104.7
u	56787.39889	23.515	0.0663	LT	-3700.1	1069.6
u	56794.45879	23.095	0.0584	LT	-10462.0	942.68
u	56795.4408	22.944	0.0586	LT	-12895.0	944.67
u	56796.44321	22.966	0.0632	LT	-12541.0	1019.3
u	56797.4459	23.738	0.0607	LT	-91.75	978.68
u	56799.43571	23.687	0.0574	LT	-923.9	925.86
u	56800.4381	23.444	0.0572	LT	-4843.0	922.28
u	56801.42262	23.554	0.0587	LT	-3062.4	946.78
u	56802.43215	23.802	0.0627	LT	940.6	1011.4
u	56803.43584	23.25	0.0621	LT	-7964.2	1000.9
u	56805.4557	23.441	0.0564	LT	-4892.8	910.1
u	56807.43068	23.017	0.0647	LT	-11718.0	1042.9
u	56808.41017	23.826	0.0593	LT	1327.3	956.18
u	56809.42509	23.862	0.0623	LT	1902.7	1005.0
u	56810.42613	23.786	0.0598	LT	680.84	964.47
u	56811.41491	23.895	0.059	LT	2428.0	951.53
u	56812.42491	24.643	0.0594	LT	14493.0	958.25
u	56813.39784	24.209	0.0584	LT	7503.0	941.16
u	56814.45105	24.687	0.0597	LT	15206.0	962.12
u	56815.39866	24.779	0.061	LT	16688.0	984.6
u	56816.40563	24.829	0.0652	LT	17500.0	1052.3
u	56817.40567	25.263	0.0643	LT	24497.0	1037.7
u	56818.41048	26.172	0.0606	LT	39161.0	977.28
u	56819.41057	26.952	0.0622	LT	51734.0	1002.9
u	56822.39121	26.553	0.0646	LT	45311.0	1042.4
u	56823.40216	26.752	0.0654	LT	48514.0	1054.2
u	56825.40992	26.878	0.0669	LT	50544.0	1079.3
u	56826.28286	24.821	0.5891	LCOGT2	17370.0	9500.7
u	56826.38771	25.315	0.0699	LT	25342.0	1128.0
u	56827.39248	24.98	0.0646	LT	19933.0	1042.0
u	56828.39482	25.21	0.0591	LT	23643.0	952.91
u	56829.21472	26.081	0.8029	LCOGT2	37698.0	12949.0
u	56829.40465	24.573	0.0615	LT	13367.0	991.8
u	56830.3974	24.421	0.0595	LT	10920.0	960.26
u	56832.43166	24.431	0.0603	LT	11085.0	972.7
u	56833.39302	24.515	0.0606	LT	12432.0	977.37
u	56834.38758	24.471	0.0613	LT	11727.0	989.34
u	56835.38907	24.178	0.0636	LT	7002.8	1026.4
u	56839.32447	23.537	0.3595	LCOGT2	-3341.6	5798.0
u	56841.40694	24.217	0.0642	LT	7625.2	1036.0
u	56843.38678	23.533	0.0636	LT	-3406.6	1026.0
u	56845.40612	23.291	0.0626	LT	-7298.6	1009.6
u	56847.39677	22.276	0.0678	LT	-23679.0	1094.3
u	56858.38334	22.153	0.0654	LT	-25664.0	1055.4
u	56860.38227	21.712	0.0704	LT	-32781.0	1135.5
u	56861.3813	22.287	0.0612	LT	-23493.0	987.43
u	56862.38184	20.584	0.0609	LT	-50963.0	982.63
u	56863.38026	21.421	0.0592	LT	-37470.0	955.17
u	56864.38028	21.867	0.0685	LT	-30267.0	1105.1
u	56865.37923	22.342	0.0683	LT	-22606.0	1101.0
u	56866.37862	23.087	0.0686	LT	-10590.0	1107.0
u	56867.37845	22.346	0.0595	LT	-22546.0	960.0
u	56868.37844	23.611	0.0608	LT	-2139.7	980.23
u	56869.37782	24.095	0.0621	LT	5658.9	1000.8
u	56871.37598	24.758	0.0621	LT	16361.0	1001.1
u	56872.37488	24.806	0.0639	LT	17123.0	1030.1
u	56873.37485	24.676	0.064	LT	15036.0	1032.9
u	56874.3734	24.601	0.0628	LT	13817.0	1012.9
u	56877.37135	25.401	0.0558	LT	26721.0	899.94
u	56885.36554	27.729	0.0626	LT	64272.0	1009.0
u	56888.36414	27.791	0.0648	LT	65267.0	1044.9
u	56889.36351	27.782	0.0531	LT	65132.0	856.45
u	56892.36096	27.996	0.0567	LT	68575.0	915.17
u	56894.36491	26.564	0.0677	LT	45485.0	1091.6
u	56896.38142	26.664	0.0493	LT	47090.0	795.62
B	56645.63765	13.392	0.0228	WC18	-16159.0	460.55

Table 8 — *Continued*

Filter	HJD $-2,400,000$	F_λ (10^{-15}erg cm^{-2} s^{-1} Å^{-1})	σ_{F_λ}	Telescope ID (as in Table 1)	Differential Counts (DC) (reference counts)	error DC (reference counts)
B	56646.64619	13.397	0.0378	WC18	-16055.0	764.35
B	56647.64841	13.099	0.0294	WC18	-22095.0	595.81
B	56648.61955	13.172	0.0667	WC18	-20619.0	1350.3
B	56650.56036	13.04	0.0363	WC18	-23289.0	734.5
B	56650.63532	12.933	0.189	CrAO	-25459.0	3823.6
B	56651.64689	12.862	0.2432	CrAO	-26876.0	4920.7
B	56653.63342	13.412	0.0598	WC18	-15765.0	1210.1
B	56653.66391	13.141	0.1898	CrAO	-21238.0	3840.3
B	56656.57759	13.841	0.0501	WC18	-7078.9	1013.6
B	56661.64338	12.217	0.3437	CrAO	-39941.0	6954.6
B	56664.03609	12.603	0.1586	RCT	-32126.0	3208.0
B	56665.63278	12.66	0.2088	CrAO	-30977.0	4225.3
B	56666.62893	12.917	0.0606	WC18	-25779.0	1227.1
B	56669.65828	12.791	0.0426	WC18	-28325.0	862.01
B	56670.57212	13.035	0.0487	WC18	-23377.0	986.18
B	56672.60887	13.423	0.2145	CrAO	-15537.0	4340.4
B	56674.61329	13.3	0.074	WC18	-18031.0	1496.3
B	56679.56981	13.567	0.0373	WC18	-12615.0	755.1
B	56682.61032	14.074	0.0413	WC18	-2370.5	836.53
B	56683.00791	14.22	0.0837	WMO	585.57	1692.9
B	56684.03152	14.184	0.0859	WMO	-141.85	1738.8
B	56684.61125	14.196	0.0819	WC18	108.56	1656.4
B	56685.03969	14.175	0.0866	WMO	-321.0	1753.1
B	56686.6565	14.152	0.0501	WC18	-790.61	1013.8
B	56688.52703	13.611	0.09	WC18	-11723.0	1821.7
B	56691.61532	13.533	0.1005	WC18	-13301.0	2034.3
B	56692.59056	13.947	0.3365	CrAO	-4940.0	6808.6
B	56693.59836	13.947	0.4136	CrAO	-4924.2	8367.5
B	56694.65251	14.068	0.2427	CrAO	-2476.9	4910.2
B	56695.65395	13.933	0.503	CrAO	-5211.9	10178.0
B	56698.47632	14.342	0.0485	WC18	3059.0	982.25
B	56699.4915	14.362	0.0426	WC18	3471.3	862.17
B	56700.51826	14.354	0.0409	WC18	3298.4	828.23
B	56701.58127	14.512	0.0315	WC18	6493.0	637.09
B	56705.98773	14.578	0.0709	RCT	7827.7	1435.2
B	56706.99618	14.669	0.0519	RCT	9676.7	1050.4
B	56707.99385	14.616	0.0899	RCT	8609.5	1819.3
B	56708.58501	14.615	0.0433	WC18	8579.3	876.31
B	56709.56658	14.465	0.0506	WC18	5543.8	1023.5
B	56710.54383	14.305	0.1609	CrAO	2301.4	3255.2
B	56710.59783	13.984	0.0435	WC18	-4183.6	879.14
B	56711.60131	13.934	0.2163	CrAO	-5199.6	4376.3
B	56716.49693	13.108	0.0971	WC18	-21909.0	1964.8
B	56721.01552	12.438	0.1432	LCOGT1	-35473.0	2896.8
B	56721.49169	12.196	0.088	WC18	-40351.0	1780.0
B	56721.99948	11.88	0.1979	LCOGT1	-46749.0	4005.2
B	56722.49166	11.725	0.3604	LCOGT4	-49883.0	7292.1
B	56723.4699	11.728	0.0769	WC18	-49835.0	1556.8
B	56723.49188	11.683	0.3628	LCOGT4	-50744.0	7341.4
B	56724.48738	11.447	0.3598	LCOGT2	-55515.0	7280.6
B	56724.62546	11.488	0.2245	CrAO	-54686.0	4542.2
B	56725.82808	11.225	0.2128	WMO	-60012.0	4305.1
B	56726.62712	11.462	0.219	CrAO	-55205.0	4430.6
B	56727.47245	11.691	0.0523	WC18	-50576.0	1058.3
B	56727.50135	11.664	0.3653	LCOGT4	-51131.0	7391.1
B	56727.59782	11.797	0.1876	CrAO	-48438.0	3796.0
B	56728.62372	11.524	0.1781	CrAO	-53950.0	3604.6
B	56729.61433	11.991	0.2409	CrAO	-44506.0	4873.4
B	56730.56953	11.41	0.1676	CrAO	-56257.0	3391.4
B	56730.92161	11.838	0.1791	WMO	-47609.0	3623.4
B	56731.55243	11.688	0.4405	LCOGT3	-50630.0	8913.0
B	56731.56761	11.694	0.2265	CrAO	-50522.0	4582.1
B	56732.46659	12.054	0.215	LCOGT2	-43237.0	4349.5
B	56733.48779	12.236	0.2351	LCOGT4	-39553.0	4756.5
B	56733.93324	11.974	0.1558	RCT	-44853.0	3152.5
B	56733.96388	12.041	0.1654	LCOGT1	-43506.0	3347.2
B	56734.46333	12.29	0.3361	LCOGT3	-38464.0	6799.6
B	56735.48402	12.275	0.3316	LCOGT3	-38771.0	6708.7
B	56735.56102	12.448	0.1181	CrAO	-35269.0	2390.3
B	56736.92805	13.123	0.1032	RCT	-21608.0	2088.9
B	56736.95796	13.169	0.102	LCOGT1	-20672.0	2064.0
B	56737.45565	13.222	0.0255	WC18	-19610.0	515.52
B	56737.46597	13.289	0.2913	LCOGT3	-18237.0	5893.2
B	56737.61136	13.191	0.1281	CrAO	-20233.0	2591.4
B	56737.92657	14.122	0.3869	RCT	-1385.6	7827.8
B	56737.96	13.381	0.0757	LCOGT1	-16392.0	1531.4
B	56738.46522	13.848	0.3024	LCOGT3	-6937.7	6118.7
B	56738.4668	13.626	0.0545	WC18	-11418.0	1102.4

Table 8 — *Continued*

Filter	HJD $-2,400,000$	F_λ (10^{-15}erg cm^{-2} s^{-1} Å^{-1})	σ_{F_λ}	Telescope ID (as in Table 1)	Differential Counts (DC) (reference counts)	error DC (reference counts)
B	56738.57982	13.759	0.1761	CrAO	-8746.3	3562.8
B	56739.32863	13.754	0.0711	WC18	-8828.2	1438.3
B	56739.59459	14.194	0.2064	CrAO	71.82	4176.4
B	56739.91596	14.148	0.0874	RCT	-867.41	1768.4
B	56739.91835	14.095	0.0858	WMO	-1928.6	1736.0
B	56740.57613	14.382	0.2155	CrAO	3872.5	4360.8
B	56741.5253	14.789	0.2885	CrAO	12103.0	5837.2
B	56741.90709	14.784	0.1218	RCT	12011.0	2463.5
B	56742.46715	14.723	0.07	WC18	10770.0	1417.1
B	56742.91176	14.635	0.1591	RCT	8995.6	3219.0
B	56744.4604	15.363	0.0722	WC18	23710.0	1461.1
B	56745.85691	15.29	0.1413	RCT	22242.0	2859.3
B	56746.42943	15.839	0.2956	CrAO	33358.0	5980.0
B	56748.48947	15.921	0.0674	WC18	35017.0	1363.4
B	56750.3646	15.726	0.0874	WC18	31067.0	1768.1
B	56750.60089	15.8	0.237	CrAO	32565.0	4794.9
B	56751.53726	15.808	0.3789	CrAO	32722.0	7666.3
B	56752.43447	15.575	0.0676	WC18	28016.0	1367.1
B	56753.92625	14.857	0.1048	RCT	13476.0	2120.1
B	56754.38909	14.565	0.0494	WC18	7562.7	999.68
B	56755.44294	14.296	0.0518	WC18	2126.0	1048.8
B	56756.47615	14.459	0.2698	CrAO	5422.7	5459.0
B	56756.92239	14.666	0.0986	RCT	9605.5	1994.9
B	56757.3614	14.404	0.0277	WC18	4304.5	559.79
B	56758.52686	14.621	0.2132	CrAO	8703.6	4313.2
B	56760.89217	14.062	0.0634	RCT	-2605.3	1282.3
B	56762.45016	14.043	0.1202	CrAO	-2990.1	2432.2
B	56763.84561	14.059	0.06	RCT	-2671.6	1213.7
B	56764.90845	14.103	0.0619	RCT	-1777.4	1252.2
B	56765.32336	14.025	0.0333	WC18	-3349.1	673.04
B	56765.51256	14.241	0.1089	CrAO	1017.6	2203.5
B	56766.31096	14.166	0.0785	WC18	-511.55	1588.1
B	56769.85204	14.676	0.0986	RCT	9818.1	1994.1
B	56771.80401	14.916	0.0945	RCT	14677.0	1912.8
B	56772.80764	15.011	0.1039	RCT	16593.0	2102.5
B	56778.46091	15.328	0.4788	CrAO	23011.0	9687.5
B	56780.78297	14.852	0.0998	RCT	13384.0	2019.8
B	56784.4668	15.248	0.3471	CrAO	21396.0	7022.1
B	56786.7599	14.982	0.0518	RCT	16009.0	1048.9
B	56787.81675	14.976	0.0518	RCT	15889.0	1047.5
B	56788.47011	15.172	0.1292	CrAO	19854.0	2614.7
B	56788.81867	14.932	0.0744	RCT	14988.0	1505.6
B	56792.49051	14.459	0.4473	CrAO	5417.3	9050.5
B	56793.50159	14.99	0.2484	CrAO	16162.0	5026.5
B	56793.83937	14.805	0.0447	RCT	12422.0	905.38
B	56795.50129	14.534	0.135	CrAO	6948.7	2732.2
B	56795.77306	14.806	0.1	RCT	12444.0	2022.5
B	56797.47623	14.879	0.1319	CrAO	13924.0	2669.6
B	56797.7977	15.104	0.1205	RCT	18484.0	2438.5
B	56798.78371	14.916	0.1255	RCT	14667.0	2538.7
B	56799.35806	15.146	0.5153	CrAO	19333.0	10426.0
B	56799.76081	14.86	0.0995	RCT	13537.0	2012.9
B	56800.34275	14.926	0.0879	WC18	14866.0	1777.5
B	56800.45432	14.974	0.6266	CrAO	15850.0	12678.0
B	56801.41086	14.846	0.0711	WC18	13247.0	1438.4
B	56801.83263	14.789	0.1176	RCT	12112.0	2378.8
B	56802.33922	14.922	0.0983	WC18	14795.0	1988.9
B	56802.35528	14.952	0.3234	CrAO	15395.0	6544.3
B	56803.358	14.992	0.1043	WC18	16203.0	2109.4
B	56804.3879	14.939	0.0553	WC18	15134.0	1118.9
B	56804.76204	14.852	0.1028	RCT	13386.0	2080.6
B	56805.78152	14.854	0.0916	RCT	13428.0	1854.2
B	56811.35298	15.102	0.067	WC18	18427.0	1355.2
B	56815.38556	15.515	0.0308	WC18	26800.0	622.85
B	56817.39469	15.853	0.0927	WC18	33633.0	1876.0
B	56817.41998	15.658	0.1533	CrAO	29690.0	3101.9
B	56818.37099	15.961	0.1579	CrAO	35816.0	3195.2
B	56819.43109	15.868	0.1527	CrAO	33930.0	3088.9
B	56820.33301	16.437	0.0417	WC18	45457.0	844.56
B	56822.32424	16.245	0.0258	WC18	41568.0	522.52
B	56823.36172	16.319	0.032	WC18	43064.0	647.78
B	56824.36529	16.269	0.0493	WC18	42044.0	997.41
B	56824.37139	16.258	0.1702	CrAO	41817.0	3444.3
B	56825.40133	16.08	0.0289	WC18	38225.0	585.7
B	56825.42925	16.004	0.1538	CrAO	36682.0	3112.9
B	56827.39423	15.485	0.0521	WC18	26176.0	1053.9
B	56829.32712	15.125	0.0848	WC18	18893.0	1714.8
B	56831.30382	14.877	0.1066	WC18	13887.0	2157.0

Table 8 — *Continued*

Filter	HJD $-2,400,000$	F_λ (10^{-15}erg cm^{-2} s^{-1} Å^{-1})	σ_{F_λ}	Telescope ID (as in Table 1)	Differential Counts (DC) (reference counts)	error DC (reference counts)
B	56832.29724	14.858	0.11	WC18	13502.0	2226.2
B	56834.34737	15.109	0.1109	WC18	18576.0	2243.7
B	56834.39826	15.174	0.364	CrAO	19898.0	7365.8
B	56835.40363	14.935	0.0548	WC18	15059.0	1108.6
B	56835.41493	15.018	0.3215	CrAO	16736.0	6505.3
B	56836.3355	14.89	0.0757	WC18	14157.0	1531.2
B	56837.33639	15.005	0.0746	WC18	16464.0	1508.9
B	56837.41251	15.118	0.2916	CrAO	18762.0	5900.7
B	56839.36431	14.91	0.052	WC18	14544.0	1051.5
B	56844.35805	14.689	0.0318	WC18	10071.0	642.92
B	56845.27649	14.537	0.0474	WC18	7004.1	958.78
B	56846.34947	14.406	0.0517	WC18	4347.5	1045.1
B	56848.29334	14.209	0.0277	WC18	359.27	561.05
B	56850.3344	14.039	0.047	WC18	-3076.3	951.95
B	56851.30912	13.763	0.0174	WC18	-8655.3	352.44
B	56852.28704	13.853	0.0278	WC18	-6839.1	563.11
B	56853.30153	13.591	0.0345	WC18	-12141.0	698.85
B	56854.29472	13.416	0.0299	WC18	-15685.0	604.98
B	56857.2743	13.984	0.0743	WC18	-4183.7	1502.4
B	56858.29436	14.287	0.0363	WC18	1942.3	735.15
B	56866.33554	14.593	0.0785	WC18	8134.2	1587.6
B	56867.30495	14.836	0.0565	WC18	13052.0	1143.3
B	56869.30869	14.971	0.0744	WC18	15788.0	1505.0
g	56684.78031	13.961	0.1173	LT	-8759.7	1384.1
g	56685.78609	13.999	0.0163	LT	-8305.6	192.33
g	56686.77136	13.949	0.0491	LT	-8892.6	579.47
g	56687.88287	14.078	0.1956	LCOGT1	-7372.4	2308.2
g	56689.01733	14.013	0.2152	LCOGT1	-8144.1	2539.7
g	56689.84005	13.807	0.199	LCOGT1	-10577.0	2348.6
g	56692.94828	13.913	0.1892	LCOGT1	-9317.6	2233.2
g	56693.78997	13.556	0.018	LT	-13534.0	212.56
g	56694.77052	13.742	0.0278	LT	-11342.0	327.82
g	56695.70991	13.882	0.0477	LT	-9689.0	563.01
g	56696.25188	13.844	0.3256	LCOGT5	-10131.0	3842.6
g	56696.72838	13.912	0.0206	LT	-9330.6	242.74
g	56696.98357	14.217	0.1853	LCOGT1	-5733.2	2186.4
g	56697.26607	14.114	0.2326	LCOGT5	-6947.0	2744.4
g	56697.75721	14.082	0.0141	LT	-7328.2	166.06
g	56698.2535	14.228	0.3132	LCOGT6	-5606.2	3696.2
g	56698.60902	14.162	0.0866	LCOGT2	-6380.8	1022.3
g	56698.71785	14.16	0.0161	LT	-6407.6	190.25
g	56699.71346	14.234	0.0153	LT	-5528.2	180.65
g	56700.69203	14.274	0.0876	LT	-5066.5	1033.5
g	56701.27577	13.92	0.3988	LCOGT6	-9241.0	4706.8
g	56701.56631	14.389	0.0164	LT	-3700.0	193.29
g	56701.83042	14.246	0.1769	LCOGT1	-5394.5	2087.6
g	56702.63876	14.293	0.0156	LT	-4832.9	184.59
g	56703.01457	14.306	0.1867	LCOGT1	-4688.9	2203.1
g	56703.88024	14.434	0.1697	LCOGT1	-3171.0	2003.2
g	56704.83738	14.445	0.1714	LCOGT1	-3045.9	2022.6
g	56705.95135	14.395	0.174	LCOGT1	-3637.6	2053.1
g	56706.98093	14.586	0.1736	LCOGT1	-1382.3	2049.1
g	56708.02307	14.447	0.1836	LCOGT1	-3022.8	2166.1
g	56709.2503	13.975	0.2566	LCOGT5	-8594.6	3027.7
g	56709.82729	14.248	0.187	LCOGT1	-5366.6	2207.0
g	56710.66228	13.859	0.0532	LT	-9957.0	627.63
g	56711.68656	13.688	0.0185	LT	-11982.0	217.85
g	56711.92226	13.312	0.2232	LCOGT1	-16418.0	2633.9
g	56712.27343	13.782	0.4586	LCOGT6	-10873.0	5412.6
g	56713.26581	13.76	0.3937	LCOGT5	-11131.0	4645.8
g	56713.72281	13.613	0.0143	LT	-12867.0	168.66
g	56713.91844	14.009	0.189	LCOGT1	-8185.4	2230.9
g	56714.72606	13.515	0.0272	LT	-14018.0	320.41
g	56715.27919	13.844	0.3856	LCOGT5	-10138.0	4550.0
g	56715.8309	13.836	0.2149	LCOGT1	-10225.0	2536.2
g	56716.65823	13.199	0.0656	LT	-17753.0	774.21
g	56717.73236	12.958	0.0218	LT	-20594.0	256.9
g	56717.95168	12.649	0.2693	LCOGT1	-24243.0	3177.8
g	56718.66976	12.93	0.0238	LT	-20927.0	280.9
g	56719.59986	12.674	0.2155	LCOGT2	-23938.0	2543.5
g	56720.69136	12.655	0.0226	LT	-24172.0	267.13
g	56721.71304	12.395	0.0203	LT	-27236.0	239.28
g	56722.73699	12.039	0.0233	LT	-31435.0	275.33
g	56723.57046	12.086	0.0214	LT	-30884.0	252.91
g	56724.5283	12.153	0.0204	LT	-30095.0	241.14
g	56725.53398	11.918	0.0157	LT	-32866.0	185.63
g	56726.16793	12.0	0.5262	LCOGT5	-31894.0	6210.1
g	56727.14814	11.863	0.6233	LCOGT5	-33520.0	7355.6

Table 8 — *Continued*

Filter	HJD $-2,400,000$	F_λ (10^{-15}erg cm^{-2} s^{-1} Å^{-1})	σ_{F_λ}	Telescope ID (as in Table 1)	Differential Counts (DC) (reference counts)	error DC (reference counts)
g	56728.57528	12.158	0.0188	LT	-30037.0	221.56
g	56729.4942	12.158	0.0183	LT	-30029.0	216.38
g	56730.53713	12.266	0.0173	LT	-28757.0	204.14
g	56730.8288	11.981	0.445	LCOGT1	-32119.0	5251.1
g	56733.79888	11.84	0.3544	LCOGT1	-33782.0	4182.0
g	56734.4792	12.55	0.0209	LT	-25409.0	246.69
g	56735.49729	12.837	0.0213	LT	-22017.0	251.52
g	56735.85749	13.019	0.5342	LCOGT1	-19871.0	6303.7
g	56736.50348	13.646	0.0201	LT	-12472.0	237.55
g	56736.77008	12.761	0.323	LCOGT1	-22921.0	3811.7
g	56740.85991	14.375	0.2347	LCOGT1	-3871.5	2770.1
g	56741.61068	14.15	0.0222	LT	-6521.6	262.33
g	56741.71428	14.343	0.2254	LCOGT1	-4252.7	2660.1
g	56743.5949	14.792	0.023	LT	1047.9	271.23
g	56744.6963	14.929	0.2065	LCOGT1	2664.2	2437.3
g	56746.83397	15.082	0.213	LCOGT1	4478.3	2513.3
g	56747.96827	15.504	0.2266	LCOGT1	9456.9	2674.1
g	56748.75496	14.933	0.1979	LCOGT1	2710.8	2335.0
g	56749.75212	15.101	0.172	LCOGT1	4697.8	2030.0
g	56751.98056	14.874	0.1886	LCOGT1	2019.4	2226.2
g	56752.58106	15.141	0.0332	LT	5175.2	391.28
g	56753.57604	14.791	0.0306	LT	1035.0	361.41
g	56754.55372	14.521	0.0274	LT	-2146.0	323.74
g	56755.56329	14.049	0.0212	LT	-7713.7	250.42
g	56755.97918	14.117	0.1964	LCOGT1	-6918.0	2317.8
g	56756.47692	14.193	0.1584	LCOGT2	-6014.7	1869.0
g	56757.13872	14.389	0.4853	LCOGT6	-3710.2	5726.9
g	56757.46899	14.304	0.0923	LCOGT2	-4705.5	1089.0
g	56758.74467	14.34	0.1883	LCOGT1	-4285.4	2221.7
g	56759.88442	14.032	0.1982	LCOGT1	-7919.3	2338.8
g	56760.20359	13.704	0.5373	LCOGT6	-11794.0	6340.9
g	56761.60131	13.948	0.0202	LT	-8911.8	238.11
g	56762.46791	14.264	0.023	LT	-5184.3	271.95
g	56762.78357	14.077	0.1814	LCOGT1	-7392.6	2140.3
g	56763.55634	14.296	0.0212	LT	-4800.2	250.7
g	56763.75145	14.258	0.1772	LCOGT1	-5247.9	2091.6
g	56764.82036	14.209	0.1788	LCOGT1	-5823.7	2109.9
g	56765.04045	14.136	0.4198	LCOGT5	-6688.7	4954.6
g	56765.5815	14.012	0.0218	LT	-8151.9	256.96
g	56765.87464	14.106	0.1845	LCOGT1	-7040.5	2177.7
g	56770.52544	14.266	0.0299	LT	-5154.4	352.29
g	56770.77986	14.534	0.1793	LCOGT1	-1992.8	2116.3
g	56771.51007	14.615	0.0303	LT	-1037.7	357.38
g	56772.07535	14.842	0.3716	LCOGT6	1638.7	4385.5
g	56772.49675	14.555	0.023	LT	-1740.3	271.52
g	56772.82431	14.586	0.1994	LCOGT1	-1378.9	2353.2
g	56773.83144	14.698	0.1858	LCOGT1	-59.04	2192.6
g	56774.75914	14.682	0.2383	LCOGT1	-242.35	2811.7
g	56775.54709	14.881	0.0217	LT	2104.8	256.12
g	56776.07454	15.082	0.265	LCOGT6	4475.1	3127.2
g	56777.02149	14.913	0.4864	LCOGT5	2478.1	5740.3
g	56777.52898	14.646	0.0285	LT	-676.79	336.72
g	56778.49606	14.665	0.0261	LT	-453.29	307.77
g	56779.39684	14.657	0.1185	LCOGT2	-545.68	1398.9
g	56779.4859	14.65	0.0252	LT	-621.69	297.84
g	56779.85156	14.536	0.1926	LCOGT1	-1969.9	2272.9
g	56780.49336	14.625	0.0299	LT	-923.43	352.66
g	56780.81515	14.588	0.1931	LCOGT1	-1359.1	2279.0
g	56781.49256	14.633	0.0307	LT	-826.3	361.77
g	56782.44577	14.378	0.0279	LT	-3831.9	329.49
g	56782.7409	14.478	0.2049	LCOGT1	-2658.7	2418.5
g	56783.4506	14.521	0.0282	LT	-2150.1	332.96
g	56784.43989	14.749	0.0323	LT	543.94	381.54
g	56785.47458	14.874	0.0298	LT	2017.4	351.25
g	56786.48146	14.684	0.0286	LT	-219.59	337.23
g	56787.40246	14.572	0.022	LT	-1547.9	260.22
g	56790.45804	14.528	0.02	LT	-2066.2	236.59
g	56793.46403	14.617	0.0207	LT	-1012.8	243.81
g	56794.46237	14.552	0.0282	LT	-1781.6	333.37
g	56795.44438	14.342	0.0354	LT	-4261.8	417.21
g	56796.44679	14.478	0.037	LT	-2650.9	436.96
g	56797.44947	14.572	0.0389	LT	-1540.0	459.0
g	56798.44237	14.722	0.0341	LT	226.56	402.79
g	56799.43929	14.602	0.0323	LT	-1190.4	381.16
g	56800.44167	14.572	0.0323	LT	-1546.6	381.08
g	56801.42619	14.536	0.0341	LT	-1973.3	401.93
g	56802.43572	14.516	0.0215	LT	-2207.6	253.79
g	56803.43941	14.539	0.0299	LT	-1935.1	353.02

Table 8 — *Continued*

Filter	HJD $-2,400,000$	F_λ (10^{-15}erg cm^{-2} s^{-1} Å^{-1})	σ_{F_λ}	Telescope ID (as in Table 1)	Differential Counts (DC) (reference counts)	error DC (reference counts)
g	56805.45929	14.516	0.0324	LT	-2210.6	382.64
g	56806.43246	14.541	0.0234	LT	-1910.4	275.9
g	56807.43426	14.455	0.023	LT	-2920.6	271.4
g	56808.41375	14.658	0.03	LT	-529.85	353.71
g	56809.42867	14.679	0.0305	LT	-279.1	360.2
g	56810.42973	14.644	0.0363	LT	-690.53	427.8
g	56813.40141	14.582	0.032	LT	-1428.7	378.1
g	56814.45463	14.841	0.0289	LT	1632.1	341.59
g	56815.40223	15.082	0.0315	LT	4468.2	371.44
g	56816.4092	15.101	0.0329	LT	4697.8	388.13
g	56816.63585	14.827	0.1742	LCOGT1	1469.3	2055.2
g	56817.40923	15.363	0.0282	LT	7791.2	332.57
g	56817.83107	15.248	0.2311	LCOGT1	6429.1	2726.8
g	56818.41406	15.298	0.0256	LT	7016.6	302.36
g	56819.41414	15.733	0.0259	LT	12152.0	305.51
g	56822.39478	15.74	0.0291	LT	12237.0	343.78
g	56823.40574	15.714	0.0339	LT	11933.0	400.39
g	56824.39957	15.753	0.0321	LT	12395.0	378.75
g	56825.41351	15.723	0.0394	LT	12038.0	465.08
g	56826.28815	15.38	0.1268	LCOGT2	7990.9	1496.6
g	56826.39129	15.305	0.0359	LT	7103.1	423.19
g	56827.39605	15.166	0.0345	LT	5469.6	407.41
g	56828.39839	15.059	0.0314	LT	4198.5	370.8
g	56829.40822	14.761	0.0332	LT	689.74	392.16
g	56830.40097	14.707	0.0368	LT	43.23	434.58
g	56831.39238	14.668	0.0331	LT	-413.25	390.94
g	56832.43523	14.649	0.0302	LT	-637.08	356.95
g	56833.39659	14.757	0.0276	LT	638.35	326.07
g	56834.39117	14.909	0.0276	LT	2436.8	326.25
g	56835.39264	14.627	0.0284	LT	-901.15	334.57
g	56837.23078	14.685	0.126	LCOGT2	-212.55	1486.4
g	56839.33334	14.648	0.1076	LCOGT2	-647.58	1269.4
g	56841.41052	14.786	0.0308	LT	977.99	363.84
g	56843.39036	14.545	0.0303	LT	-1864.2	357.52
g	56845.40969	14.491	0.0317	LT	-2495.6	374.51
g	56847.40034	14.168	0.0221	LT	-6312.1	261.33
g	56848.85142	13.626	0.5765	LCOGT6	-12712.0	6803.6
g	56858.38691	14.099	0.0335	LT	-7122.3	395.2
g	56860.38584	14.178	0.033	LT	-6192.2	389.77
g	56861.38487	14.088	0.0277	LT	-7258.6	327.32
g	56862.38541	14.014	0.0352	LT	-8135.8	415.09
g	56863.38384	13.759	0.0261	LT	-11145.0	307.6
g	56864.38385	13.922	0.0342	LT	-9218.7	403.69
g	56864.68837	13.747	0.2486	LCOGT1	-11283.0	2934.0
g	56865.38279	14.296	0.0334	LT	-4797.7	394.69
g	56866.38219	14.63	0.0332	LT	-862.67	391.26
g	56867.38201	14.595	0.0255	LT	-1276.3	301.4
g	56867.86188	15.256	0.6709	LCOGT5	6530.6	7917.4
g	56868.38218	14.678	0.032	LT	-297.96	377.32
g	56868.85691	14.899	0.462	LCOGT6	2310.4	5452.3
g	56869.38156	14.839	0.0348	LT	1608.7	410.46
g	56869.86692	15.077	0.4622	LCOGT6	4409.0	5454.0
g	56871.37971	14.923	0.0245	LT	2593.2	289.38
g	56871.85771	15.089	0.3054	LCOGT6	4554.6	3604.2
g	56872.37864	15.101	0.0259	LT	4703.1	305.48
g	56873.37859	14.885	0.0318	LT	2145.0	375.55
g	56874.37715	15.162	0.0308	LT	5414.5	363.72
g	56875.37785	15.16	0.0209	LT	5397.1	246.57
g	56878.37584	15.409	0.0225	LT	8328.7	265.06
g	56879.37326	15.648	0.0213	LT	11153.0	251.15
g	56880.37272	16.097	0.022	LT	16451.0	259.92
g	56883.37733	16.372	0.032	LT	19698.0	378.07
g	56884.3701	16.155	0.0293	LT	17140.0	345.78
g	56885.36928	16.157	0.0247	LT	17156.0	292.06
g	56886.36777	16.204	0.033	LT	17715.0	389.19
g	56887.36737	16.094	0.0259	LT	16415.0	305.95
g	56891.36442	16.214	0.0335	LT	17834.0	395.24
g	56892.3647	16.162	0.0272	LT	17221.0	320.51
g	56893.36382	15.998	0.0269	LT	15286.0	316.98
g	56894.36866	15.735	0.0217	LT	12175.0	256.31
g	56895.36134	15.787	0.0304	LT	12792.0	359.04
V	56645.62464	12.908	0.0201	WC18	-4676.7	338.64
V	56646.61467	12.659	0.0297	WC18	-8876.5	500.65
V	56647.63377	12.79	0.0311	WC18	-6668.4	524.11
V	56650.55074	12.712	0.0562	WC18	-7973.6	945.71
V	56653.59967	12.693	0.0399	WC18	-8293.5	671.57
V	56655.5119	12.394	0.0242	WC18	-13338.0	406.77
V	56656.53193	12.292	0.0348	WC18	-15051.0	585.0

Table 8 — *Continued*

Filter	HJD $-2,400,000$	F_λ (10^{-15}erg cm^{-2} s^{-1} Å^{-1})	σ_{F_λ}	Telescope ID (as in Table 1)	Differential Counts (DC) (reference counts)	error DC (reference counts)
V	56664.04392	12.621	0.0438	RCT	-9507.9	736.71
V	56665.0498	12.59	0.0507	RCT	-10035.0	853.23
V	56666.93406	13.248	0.1478	LCOGT1	1034.5	2488.1
V	56669.63576	12.644	0.0628	WC18	-9124.4	1057.3
V	56670.58014	12.403	0.0988	WC18	-13183.0	1663.6
V	56670.9226	12.588	0.0664	FWO	-10069.0	1117.6
V	56671.92315	13.063	0.0567	FWO	-2071.8	955.05
V	56672.94535	12.67	0.0947	FWO	-8682.1	1594.3
V	56673.93136	12.511	0.0444	LCOGT1	-11361.0	746.62
V	56674.572	12.812	0.0272	WC18	-6298.9	458.09
V	56674.94543	12.636	0.0421	LCOGT1	-9250.0	708.19
V	56677.94479	13.027	0.0686	FWO	-2674.9	1154.8
V	56677.94628	12.969	0.0694	LCOGT1	-3647.1	1168.0
V	56678.93068	12.942	0.0446	LCOGT1	-4107.5	750.62
V	56679.54685	12.95	0.0216	WC18	-3972.4	363.9
V	56679.92625	12.962	0.0798	FWO	-3776.3	1343.4
V	56681.01742	12.948	0.3584	KAIT	-3999.4	6031.8
V	56682.60277	13.328	0.0267	WC18	2396.4	449.69
V	56683.00125	13.339	0.1176	WMO	2578.6	1978.6
V	56684.0336	13.335	0.088	WMO	2508.7	1481.8
V	56684.58897	13.339	0.054	WC18	2578.9	909.5
V	56684.91572	13.286	0.0668	FWO	1677.8	1124.4
V	56685.04175	13.38	0.0886	WMO	3268.3	1490.7
V	56686.61526	13.372	0.0503	WC18	3131.8	845.98
V	56687.89097	13.149	0.0809	FWO	-625.18	1361.8
V	56687.95648	13.417	0.0671	LCOGT1	3893.9	1129.3
V	56688.5044	13.047	0.0591	WC18	-2343.1	994.12
V	56688.93635	13.238	0.0588	LCOGT1	875.31	989.64
V	56691.62226	12.916	0.0339	WC18	-4539.6	571.2
V	56692.87101	13.015	0.1145	LCOGT1	-2872.8	1926.6
V	56693.82884	12.926	0.0496	LCOGT1	-4380.2	835.57
V	56693.89079	13.128	0.0782	FWO	-971.76	1315.5
V	56697.55422	13.34	0.0682	WC18	2590.6	1148.6
V	56697.82079	13.304	0.0505	LCOGT1	1976.2	849.26
V	56697.8325	13.275	0.0811	FWO	1497.8	1365.0
V	56698.52913	13.372	0.0397	WC18	3134.4	668.85
V	56699.46554	13.48	0.0313	WC18	4942.5	526.2
V	56700.49535	13.461	0.0337	WC18	4622.5	566.47
V	56700.99825	13.684	0.2324	KAIT	8381.5	3911.2
V	56701.035	13.498	0.0553	RCT	5244.6	931.15
V	56701.55568	13.462	0.023	WC18	4643.5	387.9
V	56701.8164	13.487	0.0359	LCOGT1	5056.6	604.01
V	56701.8256	13.423	0.0538	FWO	3989.3	906.08
V	56701.9778	13.657	0.2688	KAIT	7921.5	4523.9
V	56702.53063	13.479	0.0283	WC18	4930.6	476.66
V	56702.8079	13.469	0.0356	LCOGT1	4760.6	599.65
V	56703.8555	13.542	0.069	FWO	5991.5	1161.3
V	56704.79649	13.734	0.0439	LCOGT1	9225.0	739.27
V	56705.85883	13.553	0.0492	LCOGT1	6182.4	827.33
V	56706.84653	13.62	0.0486	LCOGT1	7304.7	817.4
V	56707.0072	13.484	0.0351	RCT	5018.8	590.05
V	56707.88099	13.807	0.058	FWO	10454.0	975.52
V	56708.00481	13.554	0.0321	RCT	6185.9	539.86
V	56708.62443	13.492	0.0352	WC18	5140.2	592.93
V	56708.8864	13.725	0.2755	KAIT	9065.6	4636.7
V	56708.92011	13.251	0.0896	LOAO	1097.1	1507.6
V	56709.00386	13.48	0.0309	RCT	4952.1	519.51
V	56709.58949	13.372	0.0262	WC18	3131.8	440.22
V	56709.8115	13.395	0.0366	LCOGT1	3515.6	615.98
V	56709.85646	13.528	0.0548	FWO	5747.0	922.06
V	56709.96162	13.615	0.0516	LOAO	7221.3	867.71
V	56710.00608	13.274	0.0325	RCT	1473.6	546.82
V	56710.47224	13.308	0.0375	WC18	2052.7	631.41
V	56710.92726	13.328	0.2278	KAIT	2392.6	3834.1
V	56711.00907	13.038	0.0582	LOAO	-2493.7	979.49
V	56711.79904	13.381	0.0816	LCOGT1	3282.9	1373.2
V	56711.8909	13.472	0.3458	KAIT	4819.6	5819.5
V	56712.00111	13.301	0.0521	LOAO	1939.2	876.93
V	56712.20821	13.331	0.0729	LCOGT6	2436.1	1227.6
V	56712.91193	13.439	0.3006	KAIT	4261.3	5059.9
V	56713.19762	13.173	0.0687	LCOGT5	-223.16	1156.0
V	56713.81538	13.168	0.0585	LCOGT1	-311.24	984.13
V	56714.21081	13.016	0.1124	LCOGT5	-2862.6	1891.8
V	56714.45903	12.988	0.0355	WC18	-3327.2	597.39
V	56715.02663	13.066	0.0481	RCT	-2016.4	808.84
V	56715.54025	13.198	0.0764	LCOGT3	192.72	1285.6
V	56715.81971	12.902	0.0799	LCOGT1	-4788.9	1345.2
V	56715.89472	12.62	0.0647	FWO	-9529.7	1089.6

Table 8 — *Continued*

Filter	HJD $-2,400,000$	F_λ (10^{-15}erg cm^{-2} s^{-1} Å^{-1})	σ_{F_λ}	Telescope ID (as in Table 1)	Differential Counts (DC) (reference counts)	error DC (reference counts)
V	56716.00845	12.929	0.0503	RCT	-4320.0	845.93
V	56716.84624	12.957	0.0896	LCOGT1	-3850.8	1508.0
V	56716.91669	12.496	0.0584	FWO	-11617.0	982.89
V	56717.90183	12.463	0.0653	FWO	-12178.0	1098.5
V	56718.46525	12.464	0.0467	WC18	-12155.0	786.46
V	56722.93956	11.669	0.0972	FWO	-25533.0	1635.5
V	56723.44704	11.586	0.0419	WC18	-26929.0	705.74
V	56723.87681	11.55	0.1031	FWO	-27540.0	1735.6
V	56725.85614	11.526	0.0934	WMO	-27946.0	1571.3
V	56727.4496	11.572	0.0371	WC18	-27169.0	624.78
V	56729.82751	11.87	0.1018	FWO	-22157.0	1713.2
V	56730.87228	11.873	0.0905	FWO	-22094.0	1523.3
V	56730.91885	11.93	0.0951	WMO	-21135.0	1600.2
V	56731.87819	11.849	0.2929	KAIT	-22503.0	4929.4
V	56731.89093	12.099	0.1134	LOAO	-18303.0	1908.5
V	56732.49732	12.056	0.0258	WC18	-19018.0	434.97
V	56733.03934	11.503	0.2593	KAIT	-28320.0	4364.7
V	56733.81337	11.726	0.0917	LOAO	-24573.0	1543.9
V	56734.8749	12.002	0.0905	FWO	-19924.0	1523.1
V	56734.93954	12.279	0.1102	LOAO	-15272.0	1854.9
V	56735.77574	12.66	0.0481	FWO	-8859.7	809.77
V	56735.94263	12.559	0.0332	RCT	-10551.0	559.07
V	56737.4327	12.63	0.0192	WC18	-9351.4	322.85
V	56738.44405	12.825	0.0276	WC18	-6080.8	465.09
V	56738.99077	13.007	0.0367	LCOGT1	-3015.5	618.47
V	56739.92102	13.332	0.0861	WMO	2449.1	1448.4
V	56739.92692	13.34	0.0395	RCT	2594.6	665.6
V	56739.95124	13.337	0.2922	KAIT	2538.7	4917.0
V	56740.97243	13.431	0.0585	LCOGT1	4129.6	984.53
V	56741.73763	13.66	0.0543	FWO	7975.7	914.12
V	56741.87938	13.491	0.0833	WMO	5132.2	1402.4
V	56741.91613	13.509	0.049	RCT	5427.9	825.29
V	56741.95456	13.447	0.0806	LCOGT1	4382.8	1356.6
V	56742.44415	13.66	0.0434	WC18	7969.5	730.62
V	56742.91724	13.529	0.0651	LOAO	5770.3	1094.9
V	56742.99643	13.745	0.0681	LCOGT1	9404.6	1145.7
V	56744.43787	13.954	0.0423	WC18	12924.0	712.73
V	56744.51056	13.805	0.0743	LCOGT2	10412.0	1250.3
V	56744.93717	13.925	0.053	RCT	12437.0	891.71
V	56744.99568	14.01	0.0656	LCOGT1	13866.0	1103.5
V	56745.80353	14.134	0.0652	FWO	15954.0	1096.5
V	56745.86784	14.079	0.0478	RCT	15021.0	804.43
V	56746.69823	14.183	0.0835	FWO	16783.0	1405.4
V	56748.46653	14.361	0.0379	WC18	19773.0	638.48
V	56750.38294	14.405	0.0344	WC18	20514.0	578.32
V	56752.4092	14.113	0.0407	WC18	15594.0	685.41
V	56753.31809	13.975	0.0282	WC18	13275.0	474.65
V	56753.49783	13.775	0.1084	LCOGT2	9919.3	1825.1
V	56753.93723	13.8	0.0526	RCT	10330.0	885.98
V	56753.98618	13.695	0.1622	KAIT	8572.5	2729.3
V	56754.36599	13.593	0.0304	WC18	6846.4	511.65
V	56754.98449	13.435	0.259	KAIT	4182.4	4359.1
V	56755.42016	13.508	0.033	WC18	5410.0	555.7
V	56755.52628	13.526	0.0896	LCOGT3	5724.8	1508.6
V	56755.87897	13.509	0.0882	WMO	5429.6	1483.6
V	56756.72951	13.723	0.0539	FWO	9040.5	906.54
V	56756.93335	13.581	0.0483	RCT	6650.1	813.63
V	56756.97733	13.783	0.3578	KAIT	10045.0	6022.5
V	56757.33825	13.458	0.0177	WC18	4580.1	298.66
V	56757.43267	13.627	0.086	LCOGT3	7417.4	1448.0
V	56757.95782	13.677	0.2035	KAIT	8266.0	3425.0
V	56758.47171	13.423	0.0725	WC18	3992.6	1220.8
V	56758.50554	13.34	0.0599	LCOGT2	2585.9	1008.8
V	56758.88531	13.447	0.084	WMO	4388.4	1414.2
V	56758.97678	13.535	0.1016	LCOGT1	5874.7	1710.6
V	56759.92371	13.569	0.2396	KAIT	6451.3	4032.0
V	56760.57987	13.436	0.0972	LCOGT3	4197.5	1635.8
V	56760.93829	13.262	0.3531	KAIT	1271.5	5943.3
V	56761.51975	13.501	0.0907	LCOGT3	5304.8	1525.7
V	56762.79873	13.461	0.0602	FWO	4628.4	1013.6
V	56765.93817	13.461	0.3399	KAIT	4627.9	5719.9
V	56766.3768	13.284	0.0188	WC18	1644.2	316.68
V	56766.79603	13.143	0.0925	LOAO	-720.6	1556.0
V	56766.93552	13.743	0.5031	KAIT	9374.3	8467.6
V	56767.01315	13.149	0.0804	LCOGT6	-623.64	1353.3
V	56767.87074	13.192	0.0717	LOAO	105.34	1206.7
V	56767.89266	13.304	0.0523	RCT	1976.4	880.38
V	56767.9407	13.15	0.2164	KAIT	-612.89	3641.7

Table 8 — *Continued*

Filter	HJD $-2,400,000$	F_λ (10^{-15}erg cm^{-2} s^{-1} Å^{-1})	σ_{F_λ}	Telescope ID (as in Table 1)	Differential Counts (DC) (reference counts)	error DC (reference counts)
V	56767.98214	13.32	0.0504	LCOGT1	2259.6	848.39
V	56768.33497	13.282	0.0402	WC18	1609.2	676.16
V	56768.83934	13.465	0.0606	LOAO	4696.4	1020.7
V	56768.96374	13.596	0.3396	KAIT	6895.2	5715.7
V	56769.25698	13.387	0.0491	WC18	3373.0	825.71
V	56769.863	13.582	0.0459	RCT	6656.0	772.4
V	56769.95002	13.541	0.0854	LCOGT1	5965.8	1437.0
V	56770.27989	13.525	0.086	MO15	5703.7	1446.6
V	56770.67784	13.663	0.0628	FWO	8018.4	1057.5
V	56770.94507	13.552	0.0814	LCOGT1	6153.2	1369.1
V	56771.81506	13.759	0.0477	RCT	9640.3	802.53
V	56772.4603	13.663	0.0898	LCOGT3	8027.1	1510.7
V	56772.92254	13.807	0.1098	LCOGT1	10455.0	1847.3
V	56773.24453	13.796	0.0416	WC18	10268.0	700.35
V	56773.68983	13.93	0.0584	FWO	12514.0	983.47
V	56774.27225	13.847	0.0467	WC18	11119.0	786.44
V	56774.2731	13.947	0.0969	MO15	12799.0	1631.0
V	56774.65979	13.935	0.0629	HLCO	12604.0	1058.3
V	56775.27574	13.905	0.0542	WC18	12100.0	912.36
V	56775.29497	13.945	0.1167	MO15	12774.0	1964.1
V	56775.99862	13.863	0.1085	LCOGT6	11400.0	1825.4
V	56776.25723	13.858	0.0468	WC18	11313.0	788.08
V	56777.25371	13.8	0.0454	WC18	10336.0	763.69
V	56777.69865	13.743	0.0588	FWO	9371.2	988.76
V	56777.93899	13.753	0.0774	LCOGT1	9535.0	1302.8
V	56778.25389	13.797	0.0508	WC18	10275.0	854.45
V	56779.28349	13.77	0.0473	WC18	9827.0	795.87
V	56779.78602	13.711	0.1453	WMO	8834.9	2445.6
V	56779.91881	13.528	0.2402	KAIT	5754.1	4042.5
V	56779.92352	13.726	0.0853	LCOGT1	9087.5	1436.2
V	56780.22741	13.885	0.0977	MO15	11770.0	1643.8
V	56780.26593	13.756	0.0488	WC18	9589.4	821.66
V	56780.66161	13.867	0.0581	FWO	11452.0	977.39
V	56780.79391	13.784	0.0501	RCT	10059.0	842.9
V	56780.835	13.809	0.0865	WMO	10485.0	1456.3
V	56780.95307	13.817	0.0959	LCOGT1	10616.0	1614.5
V	56781.2496	13.74	0.0427	WC18	9323.4	718.71
V	56781.69734	13.836	0.0588	FWO	10939.0	989.79
V	56781.73245	13.764	0.0559	HLCO	9718.5	940.78
V	56781.95313	13.693	0.1345	LCOGT1	8535.1	2263.3
V	56782.39884	13.729	0.0589	WC18	9136.6	990.88
V	56782.70281	13.773	0.0536	HLCO	9873.7	902.1
V	56783.2823	13.675	0.0785	MO15	8223.4	1321.7
V	56783.63788	13.724	0.0577	FWO	9047.4	970.9
V	56783.65769	13.691	0.0503	HLCO	8497.7	846.55
V	56783.88948	13.707	0.124	LCOGT1	8762.1	2086.8
V	56784.64367	13.824	0.0549	HLCO	10730.0	924.3
V	56784.88003	13.779	0.0667	LCOGT1	9977.6	1122.8
V	56785.63644	13.996	0.0656	HLCO	13630.0	1104.1
V	56785.87493	13.928	0.0668	RCT	12489.0	1124.0
V	56785.92903	13.911	0.0939	LCOGT1	12195.0	1579.6
V	56786.76923	13.852	0.0352	RCT	11201.0	593.21
V	56786.94235	13.56	0.0696	LCOGT1	6288.9	1170.9
V	56787.26931	13.832	0.0572	MO15	10871.0	962.03
V	56787.82769	13.766	0.032	RCT	9755.1	538.81
V	56787.91521	13.724	0.1367	LCOGT1	9047.1	2300.4
V	56788.25572	13.829	0.0615	MO15	10823.0	1034.5
V	56788.66999	13.824	0.0542	FWO	10728.0	912.77
V	56788.83197	13.783	0.0306	RCT	10053.0	515.53
V	56789.21464	13.636	0.0656	MO15	7574.8	1104.2
V	56789.439	13.774	0.0889	LCOGT3	9897.0	1496.0
V	56789.69919	13.707	0.0491	HLCO	8758.4	825.95
V	56789.83302	13.75	0.2684	KAIT	9496.4	4516.8
V	56789.93702	13.681	0.0487	LCOGT1	8322.3	819.05
V	56790.28242	13.509	0.0448	MO15	5441.8	753.72
V	56790.35273	13.611	0.0709	LCOGT2	7148.0	1193.1
V	56791.77294	13.676	0.0824	WMO	8245.5	1386.9
V	56791.92149	13.482	0.0493	LCOGT1	4982.5	829.64
V	56792.67079	13.531	0.0506	FWO	5805.4	851.43
V	56792.92481	13.594	0.0626	LCOGT1	6871.6	1054.0
V	56793.56782	13.627	0.1568	LCOGT8	7427.4	2639.1
V	56793.65918	13.738	0.0533	FWO	9282.6	897.07
V	56793.76694	13.749	0.0469	HLCO	9469.7	788.96
V	56793.85033	13.775	0.0269	RCT	9911.8	452.77
V	56793.88441	13.728	0.1863	KAIT	9121.5	3136.0
V	56794.66711	13.723	0.0537	FWO	9034.7	903.19
V	56794.87513	13.841	0.2758	KAIT	11025.0	4642.5
V	56795.31253	13.745	0.0781	LCOGT2	9410.6	1314.6

Table 8 — *Continued*

Filter	HJD $-2,400,000$	F_λ (10^{-15}erg cm^{-2} s^{-1} Å^{-1})	σ_{F_λ}	Telescope ID (as in Table 1)	Differential Counts (DC) (reference counts)	error DC (reference counts)
V	56795.3344	13.616	0.0274	WC18	7241.2	460.42
V	56795.63368	13.674	0.0612	FWO	8216.5	1030.1
V	56795.78421	13.711	0.0342	RCT	8834.8	575.79
V	56795.88222	13.394	0.2886	KAIT	3491.0	4856.7
V	56795.91773	13.6	0.0428	LCOGT1	6968.2	720.66
V	56796.3058	13.61	0.0647	WC18	7127.0	1088.2
V	56796.6691	13.681	0.0614	FWO	8329.9	1033.0
V	56796.90208	13.624	0.0482	LCOGT1	7372.7	811.48
V	56797.54744	13.694	0.163	LCOGT8	8540.2	2743.5
V	56797.72321	13.79	0.0544	HLCO	10156.0	915.88
V	56797.78014	13.628	0.0862	WMO	7431.9	1451.3
V	56797.80541	13.77	0.0538	RCT	9830.9	904.68
V	56798.6396	13.794	0.0632	FWO	10239.0	1064.1
V	56798.6441	13.794	0.0563	HLCO	10237.0	946.96
V	56798.77223	13.784	0.0914	WMO	10061.0	1538.1
V	56798.79282	13.79	0.0522	RCT	10163.0	877.75
V	56798.79355	13.581	0.0733	LOAO	6643.6	1233.2
V	56799.65095	13.753	0.0653	FWO	9541.0	1098.6
V	56799.67215	13.681	0.0509	HLCO	8334.6	857.18
V	56799.68507	13.752	0.0916	WMO	9531.3	1541.1
V	56799.77192	13.756	0.0503	RCT	9589.6	846.77
V	56799.78915	13.703	0.0532	LOAO	8701.3	896.09
V	56799.84835	13.758	0.2212	KAIT	9625.9	3722.0
V	56800.24098	13.715	0.0737	MO15	8908.1	1240.6
V	56800.37819	13.665	0.0331	WC18	8062.4	557.25
V	56800.65409	13.722	0.0519	HLCO	9026.6	873.47
V	56800.74525	13.744	0.0883	WMO	9386.2	1485.3
V	56800.86929	13.604	0.257	KAIT	7029.3	4326.0
V	56800.87271	13.59	0.0578	LOAO	6802.5	972.69
V	56800.9394	13.792	0.1251	LCOGT6	10203.0	2105.6
V	56801.26451	13.591	0.0899	MO15	6814.0	1512.3
V	56801.42282	13.724	0.0348	WC18	9055.4	585.67
V	56801.70601	13.708	0.067	FWO	8779.0	1127.9
V	56801.7137	13.674	0.0521	HLCO	8217.3	876.42
V	56801.84161	13.795	0.0497	RCT	10244.0	836.24
V	56801.95353	13.801	0.1507	LCOGT6	10356.0	2537.0
V	56802.30494	13.554	0.0934	MO15	6194.3	1572.2
V	56802.35474	13.722	0.045	WC18	9020.0	757.9
V	56802.84988	13.428	0.22	KAIT	4070.2	3702.2
V	56802.88462	13.812	0.1021	LCOGT1	10527.0	1718.5
V	56803.32685	13.758	0.074	MO15	9618.6	1245.2
V	56803.36872	13.674	0.047	WC18	8206.1	790.98
V	56803.74058	13.764	0.05	RCT	9719.0	842.32
V	56803.84495	13.644	0.2997	KAIT	7699.2	5044.8
V	56803.89132	13.792	0.1275	LCOGT1	10198.0	2145.6
V	56804.25645	13.611	0.0693	MO15	7152.2	1165.6
V	56804.39505	13.7	0.0296	WC18	8643.7	497.34
V	56804.77104	13.782	0.0729	RCT	10026.0	1226.7
V	56804.83829	13.662	0.1925	KAIT	8006.1	3240.4
V	56805.20274	13.772	0.0947	MO15	9858.1	1593.8
V	56805.53784	13.634	0.1581	LCOGT8	7530.6	2661.2
V	56805.79256	13.739	0.044	RCT	9304.2	741.05
V	56805.86049	13.639	0.2941	KAIT	7613.9	4949.1
V	56806.68272	13.728	0.0683	FWO	9124.1	1149.3
V	56806.84127	13.72	0.3021	KAIT	8983.5	5085.2
V	56806.87802	13.747	0.1	LCOGT1	9437.3	1682.3
V	56807.6917	13.779	0.0682	FWO	9970.6	1147.8
V	56807.86497	13.631	0.1794	KAIT	7484.0	3019.3
V	56808.83005	13.696	0.232	KAIT	8582.2	3904.2
V	56809.6595	13.907	0.0599	FWO	12135.0	1008.9
V	56809.83977	13.467	0.2882	KAIT	4726.3	4850.4
V	56810.33061	13.789	0.0702	WC18	10142.0	1180.8
V	56810.54012	13.849	0.1791	LCOGT8	11152.0	3013.7
V	56810.64144	13.913	0.0594	FWO	12226.0	1000.4
V	56810.79568	13.816	0.2084	KAIT	10599.0	3507.4
V	56811.33046	13.809	0.0421	WC18	10481.0	708.78
V	56811.70043	13.891	0.0643	FWO	11871.0	1083.0
V	56812.65419	13.849	0.063	HLCO	11151.0	1059.8
V	56812.70955	13.84	0.0634	FWO	11011.0	1066.9
V	56812.88843	13.829	0.0854	WMO	10825.0	1436.7
V	56813.71037	13.91	0.0593	HLCO	12181.0	997.26
V	56813.73092	13.868	0.0682	FWO	11481.0	1148.4
V	56813.76487	13.86	0.0837	WMO	11338.0	1408.2
V	56814.66602	13.928	0.0632	FWO	12493.0	1064.0
V	56814.71878	13.947	0.0856	WMO	12810.0	1440.4
V	56814.76654	13.818	0.0876	LCOGT1	10628.0	1474.5
V	56815.40007	14.064	0.0397	WC18	14774.0	668.68
V	56815.64647	14.091	0.0602	FWO	15224.0	1013.5

Table 8 — *Continued*

Filter	HJD $-2,400,000$	F_λ (10^{-15}erg cm^{-2} s^{-1} Å^{-1})	σ_{F_λ}	Telescope ID (as in Table 1)	Differential Counts (DC) (reference counts)	error DC (reference counts)
V	56815.81091	14.064	0.0877	LCOGT1	14782.0	1476.5
V	56816.67696	14.255	0.0875	LCOGT1	17996.0	1472.7
V	56816.73004	14.043	0.0548	FWO	14423.0	921.7
V	56817.32662	14.303	0.0868	MO15	18797.0	1460.5
V	56817.38541	14.28	0.031	WC18	18418.0	522.0
V	56818.29284	14.372	0.0837	MO15	19953.0	1407.9
V	56818.30927	14.593	0.0279	WC18	23684.0	469.98
V	56818.62851	14.522	0.072	LCOGT1	22489.0	1211.2
V	56818.80952	14.665	0.0982	WMO	24889.0	1651.9
V	56819.26963	14.654	0.1356	LCOGT2	24709.0	2281.3
V	56819.29232	14.906	0.1072	MO15	28948.0	1803.7
V	56819.71156	14.803	0.1006	FWO	27219.0	1693.8
V	56819.81719	14.911	0.0716	LCOGT1	29037.0	1205.2
V	56820.74132	14.901	0.0902	WMO	28859.0	1517.6
V	56820.7785	15.003	0.3082	KAIT	30586.0	5186.1
V	56820.80255	14.904	0.0872	LCOGT1	28912.0	1468.1
V	56821.32277	14.987	0.1139	LCOGT2	30306.0	1916.5
V	56821.35255	14.895	0.0252	WC18	28755.0	423.56
V	56821.74935	14.662	0.2622	KAIT	24833.0	4413.5
V	56822.30869	14.688	0.0465	WC18	25284.0	782.71
V	56822.67602	14.814	0.1067	FWO	27397.0	1795.9
V	56823.34616	14.73	0.0376	WC18	25989.0	633.11
V	56823.74657	14.734	0.2944	KAIT	26058.0	4955.5
V	56824.39947	14.702	0.0304	WC18	25508.0	512.45
V	56824.73701	14.709	0.273	KAIT	25636.0	4595.3
V	56825.37379	14.637	0.0334	WC18	24411.0	561.47
V	56825.75026	14.48	0.0936	HLCO	21770.0	1574.7
V	56826.64786	14.18	0.0909	HLCO	16724.0	1530.4
V	56826.6592	14.233	0.2088	LCOGT8	17627.0	3514.3
V	56826.68166	14.147	0.0676	FWO	16167.0	1137.9
V	56827.39605	14.199	0.0438	WC18	17055.0	736.61
V	56827.61224	14.09	0.1965	LCOGT8	15214.0	3306.4
V	56827.66844	14.27	0.1126	HLCO	18234.0	1894.8
V	56827.77405	14.092	0.0882	WMO	15249.0	1484.9
V	56828.29554	14.15	0.121	MO15	16217.0	2036.4
V	56828.78045	14.112	0.0845	WMO	15582.0	1422.1
V	56829.27609	13.952	0.1908	MO15	12890.0	3212.0
V	56829.30462	14.059	0.0619	WC18	14690.0	1041.9
V	56829.74715	13.971	0.1364	MLO	13205.0	2296.3
V	56829.74886	13.745	0.0503	HLCO	9399.7	846.16
V	56830.24214	13.956	0.1384	LCOGT2	12954.0	2329.5
V	56830.30394	14.003	0.1048	MO15	13745.0	1763.1
V	56830.76769	13.954	0.0527	LOAO	12923.0	886.21
V	56831.27387	14.004	0.1226	MO15	13773.0	2063.8
V	56831.28128	13.797	0.0705	WC18	10278.0	1187.3
V	56831.62063	13.797	0.1745	LCOGT8	10277.0	2936.1
V	56832.26813	13.775	0.1096	MO15	9904.6	1843.9
V	56832.27471	13.788	0.0723	WC18	10124.0	1217.6
V	56832.48332	13.874	0.1816	LCOGT8	11572.0	3056.7
V	56832.81541	13.973	0.0834	WMO	13237.0	1403.9
V	56833.48159	13.831	0.1763	LCOGT8	10846.0	2966.5
V	56833.73859	13.906	0.2171	KAIT	12110.0	3653.5
V	56833.82215	13.821	0.0844	WMO	10685.0	1421.0
V	56834.32497	13.824	0.0742	WC18	10730.0	1249.0
V	56834.66259	13.851	0.0561	HLCO	11189.0	943.75
V	56835.38083	13.768	0.0355	WC18	9801.6	597.35
V	56835.71455	13.733	0.2746	KAIT	9211.7	4621.9
V	56836.31307	13.756	0.049	WC18	9590.5	824.15
V	56836.62368	13.788	0.1718	LCOGT8	10127.0	2891.2
V	56836.70019	13.605	0.0557	FWO	7042.6	937.03
V	56836.72459	13.916	0.2128	KAIT	12290.0	3580.9
V	56836.81204	13.778	0.127	MLO	9960.4	2136.8
V	56837.31374	13.739	0.0482	WC18	9305.8	811.87
V	56837.62027	13.859	0.1793	LCOGT8	11320.0	3017.1
V	56837.65243	13.744	0.0564	FWO	9395.5	948.41
V	56837.71889	13.68	0.1851	MLO	8309.1	3115.9
V	56837.7699	13.859	0.0967	WMO	11324.0	1628.2
V	56838.29949	13.979	0.1204	MO15	13350.0	2026.2
V	56838.62409	13.857	0.058	FWO	11289.0	976.95
V	56838.75443	13.61	0.2129	KAIT	7134.6	3582.6
V	56838.77249	13.808	0.0872	WMO	10470.0	1467.8
V	56839.34175	13.789	0.0338	WC18	10155.0	569.5
V	56839.47767	13.825	0.1754	LCOGT8	10748.0	2951.9
V	56839.61735	13.799	0.0543	FWO	10313.0	913.4
V	56839.69027	13.87	0.0511	LOAO	11516.0	860.2
V	56839.72196	13.744	0.4271	KAIT	9388.3	7188.6
V	56839.7546	13.801	0.0939	WMO	10342.0	1580.3
V	56840.25543	13.708	0.1011	MO15	8790.6	1701.8

Table 8 — *Continued*

Filter	HJD $-2,400,000$	F_λ (10^{-15}erg cm^{-2} s^{-1} Å^{-1})	σ_{F_λ}	Telescope ID (as in Table 1)	Differential Counts (DC) (reference counts)	error DC (reference counts)
V	56840.60956	14.005	0.2501	LCOGT7	13785.0	4209.1
V	56840.6582	13.846	0.0605	FWO	11107.0	1017.8
V	56840.69592	13.875	0.0579	LOAO	11599.0	974.56
V	56840.71376	13.753	0.2608	KAIT	9548.8	4389.4
V	56840.77846	13.917	0.0862	WMO	12295.0	1451.4
V	56841.65783	13.786	0.0539	FWO	10101.0	907.01
V	56841.72252	13.807	0.1895	KAIT	10454.0	3189.5
V	56841.83064	13.866	0.086	WMO	11445.0	1447.5
V	56842.4704	13.824	0.1731	LCOGT8	10737.0	2912.7
V	56844.35881	13.669	0.0205	WC18	8124.8	344.62
V	56844.68909	13.672	0.0549	FWO	8179.9	924.06
V	56844.7216	13.902	0.1815	KAIT	12048.0	3055.1
V	56845.27055	13.633	0.0741	MO15	7514.7	1247.3
V	56845.27778	13.557	0.0206	WC18	6235.4	345.87
V	56845.59875	13.446	0.2523	LCOGT7	4365.8	4245.6
V	56845.72644	13.597	0.2009	KAIT	6914.7	3380.6
V	56846.22088	13.734	0.0817	MO15	9216.5	1374.4
V	56846.23839	13.542	0.0827	LCOGT3	5991.7	1391.2
V	56846.33736	13.607	0.0146	WC18	7088.2	244.88
V	56846.63741	13.618	0.0545	FWO	7272.1	916.9
V	56846.78517	13.526	0.0834	WMO	5717.1	1403.7
V	56847.25429	13.568	0.0627	MO15	6420.4	1055.6
V	56847.65788	13.426	0.0543	FWO	4038.3	914.4
V	56848.28878	13.465	0.0385	WC18	4701.5	648.6
V	56848.63379	13.404	0.0574	FWO	3660.2	965.28
V	56848.71618	13.505	0.301	KAIT	5364.8	5066.6
V	56850.29445	13.339	0.0307	WC18	2571.1	515.92
V	56850.32754	13.216	0.0778	LCOGT3	507.23	1308.9
V	56850.58796	13.275	0.2533	LCOGT7	1494.5	4263.1
V	56850.62787	13.19	0.0743	FWO	67.99	1251.0
V	56850.71763	13.237	0.3314	KAIT	855.16	5576.5
V	56851.58091	13.061	0.2592	LCOGT7	-2109.3	4362.9
V	56851.63369	13.13	0.0528	FWO	-941.64	889.39
V	56852.2788	12.99	0.0193	WC18	-3297.8	324.41
V	56852.62822	13.141	0.0568	FWO	-764.23	955.57
V	56853.308	12.907	0.0174	WC18	-4700.1	292.04
V	56854.31514	12.77	0.0219	WC18	-6998.3	368.46
V	56854.7073	12.509	0.3259	KAIT	-11399.0	5484.3
V	56855.5424	12.734	0.2817	LCOGT7	-7616.7	4741.3
V	56855.71651	12.83	0.3435	KAIT	-5993.6	5781.7
V	56855.7628	12.864	0.1257	WMO	-5427.1	2114.8
V	56856.69843	12.816	0.0938	MLO	-6227.0	1578.0
V	56856.70253	12.91	0.2918	KAIT	-4647.9	4910.1
V	56856.75024	12.787	0.0835	WMO	-6719.6	1405.6
V	56857.26602	13.185	0.0747	WC18	-22.49	1256.6
V	56857.55618	12.979	0.2727	LCOGT7	-3482.3	4589.7
V	56857.71842	13.241	0.2855	KAIT	924.1	4805.5
V	56858.28722	13.301	0.0386	WC18	1927.2	649.87
V	56858.71157	13.294	0.6286	KAIT	1823.6	10580.0
V	56859.29561	13.426	0.1123	LCOGT3	4043.4	1890.1
V	56860.63459	13.308	0.0809	FWO	2054.7	1362.2
V	56860.72567	13.337	0.4276	KAIT	2532.2	7196.2
V	56861.20086	13.069	0.0784	MO15	-1967.0	1320.2
V	56861.62344	13.213	0.0537	FWO	449.89	904.36
V	56861.67183	12.989	0.1569	MLO	-3309.9	2641.1
V	56861.69092	12.997	0.9013	KAIT	-3174.9	15169.0
V	56862.69153	12.907	0.1588	MLO	-4704.3	2672.9
V	56862.70101	13.267	0.2701	KAIT	1359.4	4545.6
V	56863.23803	12.746	0.1106	MO15	-7414.4	1861.6
V	56863.62566	13.195	0.0883	FWO	147.86	1485.6
V	56863.70811	13.322	0.2108	KAIT	2292.9	3547.2
V	56863.7444	13.161	0.2562	WMO	-420.1	4312.0
V	56864.51044	13.17	0.2684	LCOGT7	-263.5	4516.9
V	56864.62645	13.11	0.0842	FWO	-1274.1	1417.7
V	56864.69856	13.381	0.5612	KAIT	3282.7	9444.9
V	56865.63124	13.474	0.09	FWO	4853.2	1514.3
V	56865.69358	13.945	0.2817	KAIT	12764.0	4740.6
V	56866.32975	13.618	0.0579	WC18	7266.2	973.65
V	56866.63591	13.506	0.0686	FWO	5382.1	1154.8
V	56867.27824	13.581	0.1103	LCOGT3	6638.6	1856.1
V	56867.2824	13.681	0.0389	WC18	8328.1	654.16
V	56867.504	13.746	0.2565	LCOGT7	9425.3	4316.2
V	56867.69059	13.586	0.3012	KAIT	6728.9	5068.6
V	56868.6943	13.632	0.4023	KAIT	7497.7	6770.2
V	56869.27924	13.805	0.03	WC18	10408.0	504.72
V	56870.16673	14.189	0.0837	MO15	16872.0	1408.2
V	56870.71582	14.446	0.4149	KAIT	21205.0	6982.2
V	56871.20229	14.13	0.0997	MO15	15886.0	1678.4

Table 8 — *Continued*

Filter	HJD $-2,400,000$	F_λ (10^{-15}erg cm^{-2} s^{-1} Å^{-1})	σ_{F_λ}	Telescope ID (as in Table 1)	Differential Counts (DC) (reference counts)	error DC (reference counts)
V	56871.68576	13.771	0.2519	KAIT	9847.3	4240.0
V	56871.86753	14.088	0.1547	LCOGT5	15175.0	2604.3
V	56872.18532	14.138	0.0852	MO15	16013.0	1434.2
V	56872.86835	13.935	0.0993	LCOGT6	12606.0	1671.6
V	56873.18419	14.1	0.0748	MO15	15374.0	1259.1
V	56874.1623	14.31	0.0812	MO15	18912.0	1367.0
V	56874.6786	13.873	0.2814	KAIT	11555.0	4735.2
V	56874.73614	14.033	0.1183	MLO	14255.0	1990.3
V	56874.85039	14.271	0.1385	LCOGT5	18264.0	2330.6
V	56875.74626	14.109	0.1184	MLO	15535.0	1992.0
V	56875.86377	13.99	0.1222	LCOGT5	13536.0	2056.4
V	56883.67206	14.74	0.1922	MLO	26154.0	3234.7
V	56884.72156	14.857	0.1566	MLO	28122.0	2636.4
V	56890.65148	14.856	0.1734	MLO	28096.0	2918.7
V	56891.66975	14.875	0.154	MLO	28422.0	2592.7
V	56892.66685	14.761	0.1625	MLO	26508.0	2735.6
V	56900.64005	13.592	0.1354	MLO	6834.3	2278.1
V	56904.64346	13.45	0.0997	MLO	4445.3	1677.4
V	56905.64603	13.4	0.0976	MLO	3604.1	1642.4
V	56906.65923	13.51	0.0926	MLO	5449.7	1557.7
V	56920.61529	13.354	0.0985	MLO	2827.3	1658.3
V	56933.61558	13.007	0.0807	MLO	-3016.1	1358.6
r	56684.77966	15.726	0.0141	LT	-16832.0	491.06
r	56685.78544	15.52	0.0264	LT	-23984.0	915.05
r	56686.77071	15.586	0.0515	LT	-21698.0	1786.4
r	56687.88332	15.728	0.0984	LCOGT1	-16766.0	3414.5
r	56689.01806	15.707	0.0921	LCOGT1	-17482.0	3194.9
r	56689.84075	15.766	0.0913	LCOGT1	-15418.0	3170.1
r	56692.94899	15.638	0.0837	LCOGT1	-19877.0	2904.5
r	56693.78932	15.304	0.0107	LT	-31473.0	372.43
r	56694.76987	15.42	0.0234	LT	-27435.0	812.1
r	56695.70926	15.483	0.0322	LT	-25267.0	1118.2
r	56696.72772	15.625	0.0125	LT	-20331.0	432.35
r	56696.98428	15.768	0.0873	LCOGT1	-15377.0	3028.8
r	56697.75655	15.663	0.0213	LT	-19023.0	738.08
r	56698.25458	15.354	0.6102	LCOGT6	-29733.0	21177.0
r	56698.60973	15.654	0.4081	LCOGT2	-19313.0	14163.0
r	56698.7172	15.598	0.0677	LT	-21266.0	2350.9
r	56699.7128	15.659	0.0156	LT	-19165.0	540.45
r	56700.59946	15.875	0.0853	LCOGT4	-11668.0	2962.1
r	56700.69138	15.835	0.0155	LT	-13035.0	536.78
r	56701.56565	15.919	0.0283	LT	-10109.0	983.1
r	56701.60387	15.744	0.0885	LCOGT4	-16208.0	3072.2
r	56701.83115	15.886	0.0823	LCOGT1	-11258.0	2855.9
r	56702.6381	15.818	0.0442	LT	-13647.0	1534.5
r	56703.01559	15.814	0.1016	LCOGT1	-13780.0	3526.0
r	56704.83831	15.908	0.0855	LCOGT1	-10491.0	2968.8
r	56705.60934	15.918	0.069	LCOGT4	-10174.0	2396.4
r	56705.95231	15.806	0.1026	LCOGT1	-14051.0	3560.0
r	56706.9819	16.095	0.0873	LCOGT1	-4007.5	3028.6
r	56708.02408	15.907	0.1007	LCOGT1	-10527.0	3496.1
r	56709.82822	15.854	0.0999	LCOGT1	-12394.0	3465.7
r	56710.66162	15.756	0.0093	LT	-15781.0	321.53
r	56711.01696	15.831	0.1215	LCOGT1	-13184.0	4216.0
r	56711.68589	15.626	0.0444	LT	-20293.0	1541.4
r	56711.9232	15.708	0.088	LCOGT1	-17459.0	3054.3
r	56712.27457	15.731	0.3907	LCOGT6	-16640.0	13561.0
r	56713.72216	15.518	0.0311	LT	-24053.0	1078.3
r	56713.91937	15.678	0.0887	LCOGT1	-18506.0	3079.0
r	56714.72585	15.488	0.0387	LT	-25092.0	1343.2
r	56715.91254	15.459	0.1455	LCOGT1	-26096.0	5048.2
r	56716.64153	15.424	0.1039	LCOGT4	-27292.0	3604.8
r	56716.66435	15.293	0.0218	LT	-31853.0	755.76
r	56717.73301	15.075	0.0227	LT	-39408.0	787.98
r	56717.95355	15.415	0.219	LCOGT1	-27627.0	7601.0
r	56718.56212	15.165	0.2354	LCOGT4	-36281.0	8169.6
r	56718.67042	15.025	0.0187	LT	-41157.0	649.25
r	56719.60173	14.275	0.9817	LCOGT2	-67193.0	34070.0
r	56721.7137	14.499	0.0137	LT	-59414.0	475.5
r	56722.73766	14.419	0.0126	LT	-62170.0	436.94
r	56723.57112	14.425	0.0153	LT	-61962.0	532.01
r	56728.57593	14.16	0.0144	LT	-71179.0	498.54
r	56729.49486	14.353	0.0148	LT	-64460.0	514.46
r	56730.53779	14.283	0.0143	LT	-66889.0	497.5
r	56730.83005	14.268	0.1139	LCOGT1	-67424.0	3953.5
r	56732.49418	14.292	0.0106	LT	-66604.0	367.56
r	56733.48447	14.443	0.0089	LT	-61354.0	310.37
r	56733.80024	14.226	0.1135	LCOGT1	-68882.0	3938.7

Table 8 — *Continued*

Filter	HJD $-2,400,000$	F_λ (10^{-15}erg cm^{-2} s^{-1} Å^{-1})	σ_{F_λ}	Telescope ID (as in Table 1)	Differential Counts (DC) (reference counts)	error DC (reference counts)
r	56734.47987	14.444	0.0105	LT	-61323.0	365.06
r	56735.49794	14.529	0.0108	LT	-58349.0	375.15
r	56735.85885	14.505	0.1059	LCOGT1	-59212.0	3674.9
r	56736.50413	14.627	0.0124	LT	-54982.0	431.02
r	56736.77144	14.674	0.102	LCOGT1	-53330.0	3540.8
r	56737.48897	14.839	0.0143	LT	-47610.0	497.18
r	56740.86129	15.865	0.1474	LCOGT1	-11996.0	5117.2
r	56741.61133	15.566	0.0135	LT	-22375.0	467.42
r	56741.71564	15.858	0.1384	LCOGT1	-12226.0	4803.3
r	56742.65138	16.059	0.013	LT	-5261.2	449.63
r	56743.57966	15.969	0.1985	LCOGT4	-8375.6	6890.4
r	56743.59556	16.147	0.0199	LT	-2213.6	690.37
r	56744.53792	16.28	0.0204	LT	2397.1	706.94
r	56744.56821	16.281	0.7094	LCOGT2	2444.7	24622.0
r	56744.69766	16.036	0.1333	LCOGT1	-6069.0	4625.5
r	56746.79678	16.134	0.0963	LCOGT1	-2649.0	3343.4
r	56747.95649	16.145	0.1066	LCOGT1	-2267.1	3699.4
r	56748.75635	16.156	0.1221	LCOGT1	-1914.0	4236.2
r	56749.7535	16.185	0.1	LCOGT1	-909.05	3470.9
r	56751.98194	16.167	0.1139	LCOGT1	-1500.5	3953.6
r	56752.16505	16.624	0.5347	LCOGT6	14337.0	18558.0
r	56755.56395	15.836	0.0164	LT	-12989.0	570.88
r	56755.98044	15.916	0.1016	LCOGT1	-10221.0	3526.9
r	56756.49376	16.135	0.766	LCOGT2	-2642.0	26585.0
r	56756.51125	15.956	0.0153	LT	-8827.8	530.91
r	56757.13977	15.944	0.3301	LCOGT6	-9262.9	11457.0
r	56758.74605	15.749	0.1061	LCOGT1	-16036.0	3681.2
r	56759.88579	15.721	0.0969	LCOGT1	-17002.0	3363.9
r	56760.20496	15.828	0.2872	LCOGT6	-13266.0	9968.8
r	56761.60196	15.567	0.0154	LT	-22347.0	535.89
r	56762.78497	15.615	0.1203	LCOGT1	-20690.0	4173.8
r	56763.75958	15.439	0.0964	LCOGT1	-26798.0	3344.1
r	56764.78634	15.523	0.1382	LCOGT1	-23877.0	4795.3
r	56765.53891	15.505	0.0886	LCOGT4	-24494.0	3074.4
r	56765.58216	15.581	0.0189	LT	-21849.0	657.11
r	56765.87606	15.456	0.2445	LCOGT1	-26196.0	8484.2
r	56766.40033	15.875	0.1188	LCOGT4	-11668.0	4122.5
r	56770.5261	15.83	0.0245	LT	-13220.0	851.45
r	56770.78129	15.873	0.0974	LCOGT1	-11711.0	3381.2
r	56771.51073	15.914	0.0243	LT	-10289.0	844.78
r	56772.49741	15.963	0.0147	LT	-8590.8	508.69
r	56772.82574	15.957	0.1201	LCOGT1	-8790.0	4169.4
r	56773.38818	15.844	0.1686	LCOGT4	-12733.0	5851.4
r	56773.83291	15.962	0.1037	LCOGT1	-8647.3	3599.1
r	56774.76016	16.011	0.1743	LCOGT1	-6943.9	6051.0
r	56775.40551	15.971	0.1551	LCOGT4	-8329.3	5383.4
r	56775.54774	16.173	0.0163	LT	-1307.7	567.1
r	56776.07596	16.292	0.1746	LCOGT6	2825.9	6060.3
r	56777.52964	16.23	0.0237	LT	661.55	821.8
r	56778.49671	16.277	0.0251	LT	2314.4	870.1
r	56779.39649	15.975	0.5987	LCOGT2	-8181.4	20778.0
r	56779.48655	16.049	0.0197	LT	-5621.4	683.42
r	56779.85167	16.001	0.1165	LCOGT1	-7267.1	4041.9
r	56780.49401	16.195	0.0254	LT	-529.89	883.02
r	56780.81477	15.992	0.1124	LCOGT1	-7599.1	3899.9
r	56781.49321	16.092	0.0247	LT	-4127.1	858.37
r	56782.44643	15.954	0.0227	LT	-8919.0	788.5
r	56782.74049	15.929	0.1284	LCOGT1	-9770.3	4455.0
r	56783.45126	16.069	0.0232	LT	-4907.5	805.99
r	56784.44055	16.067	0.0239	LT	-5003.1	828.85
r	56785.47523	16.031	0.0194	LT	-6233.2	672.93
r	56786.48211	16.077	0.0182	LT	-4644.9	632.95
r	56787.40311	15.971	0.015	LT	-8335.1	520.03
r	56790.45869	15.832	0.0141	LT	-13155.0	490.1
r	56791.4332	15.833	0.0102	LT	-13114.0	354.19
r	56794.46302	15.879	0.0239	LT	-11504.0	831.1
r	56795.44503	15.825	0.0292	LT	-13395.0	1011.8
r	56796.44744	15.777	0.0302	LT	-15045.0	1047.2
r	56800.44233	16.182	0.0258	LT	-1007.6	896.36
r	56801.42684	15.996	0.0215	LT	-7448.1	746.11
r	56803.44006	16.003	0.0277	LT	-7225.0	961.81
r	56805.45996	15.892	0.0241	LT	-11069.0	836.56
r	56806.43311	15.932	0.0207	LT	-9688.2	718.94
r	56807.43492	15.852	0.0163	LT	-12460.0	567.02
r	56808.4144	16.037	0.0289	LT	-6034.7	1003.3
r	56809.42932	16.159	0.0224	LT	-1787.7	777.47
r	56810.43044	16.153	0.0314	LT	-2018.8	1090.4
r	56811.41922	16.112	0.0291	LT	-3431.1	1008.3

Table 8 — *Continued*

Filter	HJD $-2,400,000$	F_λ (10^{-15}erg cm^{-2} s^{-1} Å^{-1})	σ_{F_λ}	Telescope ID (as in Table 1)	Differential Counts (DC) (reference counts)	error DC (reference counts)
r	56813.40213	16.1	0.0298	LT	-3853.2	1032.9
r	56814.45535	16.2	0.0279	LT	-365.8	969.58
r	56815.40294	16.261	0.0292	LT	1747.0	1012.5
r	56816.27423	16.278	0.0737	LCOGT4	2340.0	2559.5
r	56816.40991	16.279	0.0267	LT	2377.5	925.55
r	56816.63948	16.063	0.0942	LCOGT1	-5135.7	3271.0
r	56817.40994	16.348	0.0268	LT	4775.4	930.72
r	56817.83435	16.135	0.0877	LCOGT1	-2643.0	3045.3
r	56818.41477	16.427	0.0212	LT	7497.7	736.32
r	56819.41485	16.454	0.0209	LT	8432.8	724.5
r	56820.484	16.782	0.0192	LT	19828.0	665.1
r	56821.24253	17.066	0.1064	LCOGT4	29700.0	3691.8
r	56822.39549	16.807	0.0251	LT	20688.0	871.89
r	56823.40645	16.921	0.0315	LT	24646.0	1093.9
r	56824.40028	16.799	0.0327	LT	20422.0	1136.6
r	56825.41423	16.92	0.0318	LT	24616.0	1104.4
r	56826.29162	16.503	0.5344	LCOGT2	10130.0	18548.0
r	56826.392	16.573	0.0323	LT	12576.0	1120.7
r	56827.39678	16.531	0.0316	LT	11116.0	1096.2
r	56828.39911	16.394	0.0326	LT	6373.2	1131.8
r	56829.40894	16.28	0.0306	LT	2413.4	1063.5
r	56830.40168	16.201	0.0346	LT	-338.57	1201.9
r	56831.39309	16.149	0.0315	LT	-2156.8	1092.2
r	56832.43594	16.239	0.033	LT	973.25	1145.7
r	56833.3973	16.098	0.0272	LT	-3926.7	944.88
r	56834.39189	16.105	0.0275	LT	-3653.8	953.99
r	56835.39334	16.067	0.0317	LT	-4981.8	1098.9
r	56837.23411	16.185	0.5326	LCOGT2	-896.93	18483.0
r	56839.33665	16.228	0.4627	LCOGT2	606.35	16058.0
r	56841.41123	16.193	0.0257	LT	-618.23	892.57
r	56842.24558	16.181	0.1239	LCOGT4	-1021.8	4299.2
r	56843.21577	16.074	0.1129	LCOGT4	-4729.8	3917.7
r	56843.39107	16.195	0.031	LT	-554.81	1074.7
r	56845.41039	16.098	0.029	LT	-3898.5	1004.9
r	56848.85472	15.512	0.5432	LCOGT6	-24260.0	18852.0
r	56858.38762	15.696	0.0322	LT	-17872.0	1117.9
r	56860.38654	15.604	0.0328	LT	-21045.0	1140.0
r	56861.38558	15.824	0.0276	LT	-13428.0	956.39
r	56862.38612	15.644	0.0271	LT	-19677.0	938.87
r	56863.38454	15.653	0.028	LT	-19368.0	972.66
r	56864.38455	15.683	0.0329	LT	-18303.0	1142.4
r	56864.6917	15.906	0.1408	LCOGT1	-10584.0	4887.4
r	56865.3835	15.703	0.0308	LT	-17608.0	1069.3
r	56865.63157	15.934	0.143	LCOGT1	-9595.0	4961.1
r	56866.38291	15.867	0.0329	LT	-11931.0	1140.2
r	56867.38272	16.067	0.03	LT	-4985.7	1041.0
r	56868.38306	16.053	0.0293	LT	-5478.4	1017.4
r	56868.86021	16.108	0.3336	LCOGT6	-3552.8	11579.0
r	56869.38243	16.152	0.0288	LT	-2043.5	998.74
r	56869.87021	16.219	0.3104	LCOGT6	275.73	10773.0
r	56871.38059	16.314	0.0283	LT	3568.5	983.65
r	56871.861	16.18	0.1924	LCOGT6	-1080.6	6676.0
r	56872.37952	16.248	0.022	LT	1295.5	764.66
r	56873.37948	16.312	0.029	LT	3512.6	1004.8
r	56874.37803	16.326	0.0305	LT	4000.8	1058.5
r	56875.37873	16.454	0.0223	LT	8453.6	775.34
r	56878.37671	16.424	0.0221	LT	7386.6	765.91
r	56879.37415	16.569	0.0197	LT	12449.0	684.25
r	56880.37361	17.025	0.0195	LT	28250.0	678.19
r	56883.37822	17.112	0.0306	LT	31267.0	1063.2
r	56884.37099	17.167	0.0309	LT	33182.0	1071.8
r	56885.37016	17.134	0.0221	LT	32042.0	766.33
r	56886.36865	17.035	0.0309	LT	28618.0	1073.7
r	56887.36825	17.181	0.0254	LT	33685.0	881.73
r	56891.36531	17.142	0.0326	LT	32327.0	1130.5
r	56892.36557	17.048	0.0306	LT	29073.0	1060.7
r	56893.36471	17.234	0.0266	LT	35522.0	922.12
r	56894.36954	17.115	0.0208	LT	31376.0	722.06
r	56895.36221	17.085	0.0272	LT	30356.0	942.67
R	56644.64139	12.765	0.1702	CrAO	-7835.7	4544.9
R	56646.62751	12.67	0.022	WC18	-10378.0	588.18
R	56647.63862	12.559	0.0219	WC18	-13352.0	585.57
R	56648.60097	12.455	0.0154	WC18	-16110.0	412.59
R	56650.5573	12.443	0.0388	WC18	-16443.0	1037.2
R	56653.60487	12.576	0.0258	WC18	-12884.0	688.6
R	56655.51715	12.57	0.0171	WC18	-13036.0	457.58
R	56656.53707	12.388	0.0222	WC18	-17919.0	591.77
R	56656.63424	12.331	0.2231	CrAO	-19432.0	5959.0

Table 8 — *Continued*

Filter	HJD $-2,400,000$	F_λ (10^{-15}erg cm^{-2} s^{-1} Å^{-1})	σ_{F_λ}	Telescope ID (as in Table 1)	Differential Counts (DC) (reference counts)	error DC (reference counts)
R	56661.63577	11.985	0.3156	CrAO	-28679.0	8430.0
R	56665.63456	12.213	0.1866	CrAO	-22573.0	4984.5
R	56665.65689	12.086	0.0236	WC18	-25972.0	630.65
R	56670.5543	12.528	0.0241	WC18	-14174.0	643.4
R	56672.61134	12.985	0.1542	CrAO	-1967.8	4119.7
R	56674.57672	12.234	0.0192	WC18	-22031.0	513.83
R	56679.55184	12.643	0.0186	WC18	-11094.0	496.11
R	56682.61237	12.867	0.0388	WC18	-5108.6	1036.3
R	56683.00423	13.075	0.0407	WMO	429.97	1087.5
R	56684.03532	12.988	0.044	WMO	-1888.2	1176.2
R	56684.59373	12.978	0.0286	WC18	-2152.0	764.56
R	56685.04341	12.952	0.0442	WMO	-2842.4	1181.1
R	56686.6204	12.885	0.0323	WC18	-4622.9	863.97
R	56688.5092	12.774	0.0379	WC18	-7604.9	1011.0
R	56691.57639	12.656	0.1977	CrAO	-10747.0	5280.6
R	56691.62732	12.688	0.02	WC18	-9901.2	533.04
R	56692.59183	13.017	0.2305	CrAO	-1106.1	6155.7
R	56693.59902	12.992	0.2037	CrAO	-1771.7	5440.5
R	56696.59964	12.726	0.212	CrAO	-8873.2	5663.1
R	56697.55904	13.003	0.0426	WC18	-1481.1	1138.0
R	56698.54186	13.226	0.0347	WC18	4481.1	927.31
R	56699.47336	13.201	0.025	WC18	3798.1	667.47
R	56700.50066	13.069	0.025	WC18	274.17	667.73
R	56701.56241	13.122	0.0816	WC18	1699.6	2178.5
R	56702.53599	13.244	0.0203	WC18	4957.3	543.0
R	56708.56677	13.378	0.0183	WC18	8536.6	487.52
R	56709.54883	13.261	0.0276	WC18	5409.3	738.19
R	56710.4773	13.216	0.0258	WC18	4196.7	688.15
R	56710.54491	13.145	0.1583	CrAO	2307.4	4227.5
R	56716.47882	12.58	0.0357	WC18	-12775.0	954.76
R	56721.47419	12.182	0.0285	WC18	-23405.0	761.51
R	56723.46431	11.805	0.0187	WC18	-33474.0	499.65
R	56725.87074	11.738	0.0726	WMO	-35258.0	1938.9
R	56727.45456	11.726	0.0271	WC18	-35598.0	723.33
R	56730.92366	12.004	0.0622	WMO	-28175.0	1660.2
R	56737.43777	12.511	0.0289	WC18	-14618.0	771.2
R	56737.61115	12.281	0.1967	CrAO	-20763.0	5254.1
R	56738.44885	12.735	0.0194	WC18	-8646.1	516.84
R	56738.58081	12.461	0.2074	CrAO	-15951.0	5539.8
R	56739.31059	12.807	0.0241	WC18	-6724.8	642.94
R	56739.91574	12.798	0.0647	WMO	-6956.2	1729.3
R	56740.57672	12.562	0.2243	CrAO	-13269.0	5990.9
R	56741.52658	13.351	0.2208	CrAO	7809.7	5897.4
R	56741.82441	13.01	0.0411	WMO	-1301.1	1098.1
R	56742.44914	13.194	0.0306	WC18	3623.0	817.5
R	56744.44266	13.461	0.0265	WC18	10740.0	706.86
R	56746.43072	14.111	0.2069	CrAO	28103.0	5526.4
R	56748.47166	13.902	0.022	WC18	22519.0	586.91
R	56748.54139	14.042	0.1961	CrAO	26274.0	5237.3
R	56750.34601	13.98	0.0313	WC18	24623.0	835.68
R	56750.60316	14.055	0.2164	CrAO	26623.0	5780.0
R	56751.54047	13.973	0.2789	CrAO	24417.0	7449.5
R	56752.4142	13.878	0.0423	WC18	21900.0	1130.7
R	56753.36276	13.772	0.0334	WC18	19047.0	893.34
R	56754.3711	13.561	0.0305	WC18	13411.0	813.74
R	56755.42524	13.402	0.0225	WC18	9188.0	601.56
R	56755.88104	13.35	0.0442	WMO	7796.8	1181.3
R	56757.3435	13.503	0.0236	WC18	11868.0	631.62
R	56758.43907	13.17	0.0271	WC18	2977.8	724.87
R	56758.52717	13.227	0.1981	CrAO	4497.4	5290.5
R	56758.88275	13.163	0.0389	WMO	2786.3	1039.6
R	56763.43422	12.829	0.1452	CrAO	-6128.5	3877.4
R	56765.51344	13.025	0.1386	CrAO	-897.42	3702.3
R	56766.29307	13.115	0.0275	WC18	1522.0	734.8
R	56774.53089	13.661	0.2031	CrAO	16091.0	5424.8
R	56778.80681	13.226	0.042	WMO	4467.0	1121.9
R	56779.78794	13.366	0.0462	WMO	8202.8	1233.9
R	56780.83251	13.39	0.04	WMO	8853.2	1069.2
R	56784.46808	13.433	0.2415	CrAO	9995.3	6449.4
R	56788.47089	13.389	0.1339	CrAO	8818.3	3577.3
R	56791.77006	13.306	0.0348	WMO	6601.3	929.35
R	56792.79587	13.046	0.0425	WMO	-335.42	1135.3
R	56795.50257	12.926	0.1458	CrAO	-3524.7	3894.3
R	56797.3049	13.426	0.0942	MO15	9828.7	2515.8
R	56797.4737	12.947	0.2124	CrAO	-2973.8	5674.6
R	56797.77789	13.269	0.041	WMO	5615.9	1095.3
R	56798.7742	13.371	0.0415	WMO	8337.2	1107.6
R	56799.36128	13.553	0.2774	CrAO	13208.0	7410.0

Table 8 — *Continued*

Filter	HJD $-2,400,000$	F_λ (10^{-15}erg cm^{-2} s^{-1} Å^{-1})	σ_{F_λ}	Telescope ID (as in Table 1)	Differential Counts (DC) (reference counts)	error DC (reference counts)
R	56799.68199	13.374	0.0413	WMO	8439.5	1103.4
R	56800.46101	13.468	0.2503	CrAO	10937.0	6686.5
R	56800.77419	13.392	0.0385	WMO	8898.5	1027.2
R	56801.42776	13.423	0.0219	WC18	9740.7	584.97
R	56802.35871	13.567	0.2377	CrAO	13581.0	6349.3
R	56802.35967	13.358	0.029	WC18	8015.1	775.42
R	56802.39694	13.327	0.0866	MO15	7166.1	2313.9
R	56803.22259	13.405	0.0919	MO15	9262.7	2453.5
R	56803.34016	13.438	0.0425	WC18	10142.0	1134.6
R	56804.39995	13.411	0.027	WC18	9424.7	720.74
R	56804.79155	13.373	0.0386	WMO	8407.0	1030.5
R	56805.43803	13.355	0.2769	CrAO	7918.4	7394.8
R	56806.41473	13.165	0.1867	CrAO	2857.5	4986.5
R	56807.3662	13.2	0.1669	CrAO	3793.9	4458.8
R	56808.74427	13.216	0.0548	WMO	4214.2	1463.0
R	56810.33555	13.344	0.0449	WC18	7635.9	1199.6
R	56811.33532	13.467	0.0352	WC18	10924.0	940.02
R	56812.79921	13.474	0.0391	WMO	11110.0	1045.3
R	56813.7909	13.489	0.0394	WMO	11495.0	1053.4
R	56814.71648	13.446	0.0429	WMO	10342.0	1145.3
R	56815.40513	13.513	0.0762	WC18	12143.0	2034.6
R	56817.39027	13.814	0.0268	WC18	20189.0	714.83
R	56817.42227	13.508	0.1554	CrAO	12018.0	4149.8
R	56818.37198	14.322	0.1803	CrAO	33756.0	4815.7
R	56818.80713	14.003	0.0529	WMO	25236.0	1411.8
R	56819.43218	13.783	0.1435	CrAO	19353.0	3833.4
R	56820.81405	14.233	0.0703	WMO	31381.0	1876.7
R	56821.73168	14.386	0.0649	WMO	35452.0	1732.7
R	56822.31349	14.059	0.0403	WC18	26727.0	1076.9
R	56822.40325	14.163	0.1623	CrAO	29514.0	4335.8
R	56823.351	14.074	0.0178	WC18	27117.0	475.83
R	56824.37249	14.191	0.1573	CrAO	30260.0	4201.1
R	56824.37408	14.163	0.0497	WC18	29504.0	1328.2
R	56825.40733	14.158	0.0468	WC18	29365.0	1249.2
R	56825.43322	14.293	0.2846	CrAO	32981.0	7601.6
R	56827.37667	13.926	0.0278	WC18	23169.0	742.42
R	56827.77166	13.716	0.0495	WMO	17551.0	1322.3
R	56828.80116	13.712	0.0608	WMO	17470.0	1623.8
R	56829.30942	13.782	0.0384	WC18	19321.0	1026.6
R	56831.28618	13.351	0.0465	WC18	7819.1	1242.6
R	56831.46575	13.606	0.1986	CrAO	14638.0	5305.7
R	56832.27962	13.442	0.0443	WC18	10250.0	1184.0
R	56832.79813	13.56	0.0422	WMO	13398.0	1125.9
R	56833.82408	13.595	0.0422	WMO	14345.0	1126.8
R	56834.32974	13.46	0.0491	WC18	10732.0	1312.2
R	56835.36363	13.611	0.0309	WC18	14762.0	825.74
R	56836.31791	13.521	0.0297	WC18	12363.0	794.16
R	56836.81004	13.378	0.0784	WMO	8541.2	2094.9
R	56837.31872	13.501	0.0301	WC18	11834.0	803.94
R	56837.78895	13.576	0.0504	WMO	13828.0	1346.3
R	56838.76999	13.577	0.0468	WMO	13849.0	1249.7
R	56839.32188	13.56	0.0299	WC18	13389.0	798.92
R	56839.75186	13.49	0.0433	WMO	11527.0	1157.7
R	56840.78037	13.64	0.0465	WMO	15536.0	1241.4
R	56841.82767	13.634	0.0853	WMO	15379.0	2277.5
R	56844.36368	13.53	0.034	WC18	12584.0	907.78
R	56845.28141	13.433	0.0142	WC18	10001.0	378.92
R	56846.3411	13.384	0.0183	WC18	8702.6	489.02
R	56846.78281	13.473	0.0521	WMO	11083.0	1390.8
R	56848.29301	13.091	0.0126	WC18	868.04	335.83
R	56850.29872	13.133	0.0148	WC18	1986.7	394.03
R	56852.28364	12.99	0.026	WC18	-1836.4	694.05
R	56853.3129	12.927	0.0166	WC18	-3498.4	443.5
R	56854.30564	12.791	0.0144	WC18	-7135.2	383.56
R	56855.76047	12.647	0.0446	WMO	-10988.0	1190.9
R	56856.24426	12.705	0.0791	MO15	-9446.8	2113.8
R	56856.74788	12.803	0.0548	WMO	-6827.3	1463.5
R	56857.25654	12.788	0.0266	WC18	-7215.4	710.57
R	56858.29198	12.98	0.0243	WC18	-2099.4	648.15
R	56859.31826	13.162	0.0362	WC18	2761.2	966.53
R	56861.73946	13.241	0.0405	WMO	4872.7	1081.6
R	56863.74208	13.262	0.0348	WMO	5430.6	929.6
R	56867.2949	13.316	0.0225	WC18	6883.5	601.78
R	56869.28405	13.399	0.0246	WC18	9090.2	657.44
i	56684.77898	10.163	0.0424	LT	-14639.0	2267.2
i	56685.78476	10.193	0.0388	LT	-13055.0	2074.4
i	56686.77002	10.263	0.0086	LT	-9307.6	458.99
i	56687.88373	10.149	0.0505	LCOGT1	-15371.0	2699.3

Table 8 — *Continued*

Filter	HJD $-2,400,000$	F_λ (10^{-15}erg cm^{-2} s^{-1} Å^{-1})	σ_{F_λ}	Telescope ID (as in Table 1)	Differential Counts (DC) (reference counts)	error DC (reference counts)
i	56689.84145	9.9929	0.0409	LCOGT1	-23731.0	2188.4
i	56692.94969	10.088	0.0233	LCOGT1	-18658.0	1247.9
i	56693.78864	9.9818	0.0108	LT	-24325.0	579.39
i	56694.76919	10.013	0.0114	LT	-22661.0	612.35
i	56695.70858	10.108	0.0107	LT	-17551.0	574.17
i	56696.72704	10.136	0.0139	LT	-16077.0	742.07
i	56696.98498	10.183	0.0368	LCOGT1	-13579.0	1969.8
i	56697.75587	10.152	0.0152	LT	-15198.0	813.25
i	56698.71651	10.214	0.0356	LT	-11924.0	1902.0
i	56699.71212	10.193	0.0393	LT	-13042.0	2101.2
i	56700.69069	10.248	0.0057	LT	-10082.0	305.63
i	56701.56497	10.255	0.014	LT	-9716.5	748.41
i	56701.83187	10.204	0.0573	LCOGT1	-12448.0	3065.2
i	56702.63742	10.327	0.0138	LT	-5850.0	736.52
i	56703.0166	10.295	0.0585	LCOGT1	-7567.0	3126.7
i	56703.88218	10.341	0.0283	LCOGT1	-5110.3	1512.9
i	56704.83926	10.351	0.0336	LCOGT1	-4552.3	1794.9
i	56705.61028	10.381	0.0252	LCOGT4	-2985.4	1345.8
i	56705.95327	10.396	0.0334	LCOGT1	-2149.1	1786.1
i	56706.98285	10.394	0.0413	LCOGT1	-2262.3	2208.4
i	56708.02508	10.421	0.0491	LCOGT1	-826.0	2626.7
i	56709.82915	10.268	0.0443	LCOGT1	-9038.7	2370.8
i	56710.66093	10.238	0.0214	LT	-10610.0	1144.7
i	56711.0179	10.269	0.0577	LCOGT1	-8979.6	3087.4
i	56711.68518	10.219	0.0104	LT	-11626.0	555.32
i	56711.92414	10.224	0.0336	LCOGT1	-11377.0	1794.5
i	56713.72148	10.099	0.0388	LT	-18080.0	2077.6
i	56713.92031	10.189	0.0362	LCOGT1	-13263.0	1936.3
i	56714.7256	10.11	0.0048	LT	-17473.0	256.1
i	56715.91352	10.075	0.0426	LCOGT1	-19344.0	2279.3
i	56716.66497	10.073	0.0119	LT	-19435.0	637.62
i	56717.73364	9.9781	0.0103	LT	-24520.0	548.36
i	56717.95542	10.032	0.09	LCOGT1	-21626.0	4814.4
i	56718.564	10.009	0.0877	LCOGT4	-22877.0	4691.7
i	56718.67105	9.8788	0.0098	LT	-29835.0	522.19
i	56719.60361	9.7784	0.1042	LCOGT2	-35205.0	5574.8
i	56720.69264	9.7176	0.0119	LT	-38457.0	637.55
i	56721.71433	9.6021	0.0086	LT	-44633.0	461.78
i	56722.73829	9.4266	0.0073	LT	-54018.0	391.05
i	56723.57174	9.498	0.0111	LT	-50201.0	591.67
i	56724.52211	9.2922	0.0822	LCOGT4	-61207.0	4396.9
i	56727.61413	9.4276	0.0929	LCOGT4	-53966.0	4968.4
i	56728.57657	9.4829	0.0078	LT	-51008.0	419.46
i	56729.4955	9.3688	0.0099	LT	-57113.0	529.12
i	56730.53842	9.4341	0.0085	LT	-53621.0	454.63
i	56730.83131	9.3824	0.0538	LCOGT1	-56386.0	2879.9
i	56731.48995	9.4652	0.0066	LT	-51956.0	354.08
i	56732.4948	9.4518	0.006	LT	-52675.0	320.31
i	56733.4851	9.465	0.006	LT	-51967.0	323.44
i	56733.79272	9.4379	0.0418	LCOGT1	-53415.0	2235.5
i	56734.4805	9.5518	0.0073	LT	-47322.0	388.96
i	56735.49857	9.5214	0.0064	LT	-48948.0	340.57
i	56735.8602	9.5989	0.0427	LCOGT1	-44805.0	2283.4
i	56736.50476	9.6861	0.0079	LT	-40143.0	422.03
i	56736.7728	9.7435	0.0449	LCOGT1	-37068.0	2401.8
i	56737.4896	9.8445	0.0084	LT	-31669.0	450.08
i	56740.86264	10.188	0.0986	LCOGT1	-13300.0	5274.5
i	56741.61196	10.135	0.0093	LT	-16120.0	496.23
i	56741.717	10.185	0.0877	LCOGT1	-13430.0	4689.6
i	56743.58081	10.336	0.0614	LCOGT4	-5388.5	3281.4
i	56744.53855	10.438	0.0115	LT	64.06	616.56
i	56744.69903	10.422	0.0781	LCOGT1	-763.39	4176.2
i	56746.79815	10.507	0.0469	LCOGT1	3753.5	2508.1
i	56747.97105	10.586	0.1161	LCOGT1	7994.6	6208.4
i	56748.75772	10.573	0.0739	LCOGT1	7284.3	3954.5
i	56749.75488	10.654	0.0531	LCOGT1	11617.0	2840.2
i	56751.98332	10.668	0.0651	LCOGT1	12374.0	3480.8
i	56752.58234	10.71	0.014	LT	14641.0	748.65
i	56753.57733	10.614	0.0138	LT	9488.3	740.64
i	56754.55501	10.533	0.0142	LT	5177.5	758.92
i	56755.97913	10.354	0.0989	LCOGT1	-4410.2	5291.6
i	56756.51191	10.333	0.0085	LT	-5526.9	452.58
i	56757.14081	10.437	0.1179	LCOGT6	33.77	6305.1
i	56757.45963	10.327	0.0397	LCOGT2	-5886.7	2124.9
i	56757.55045	10.455	0.0748	LCOGT4	984.93	4002.0
i	56758.74749	10.349	0.0553	LCOGT1	-4665.0	2958.0
i	56759.88717	10.302	0.0318	LCOGT1	-7179.6	1700.8
i	56760.20633	10.226	0.0774	LCOGT6	-11247.0	4138.4

Table 8 — *Continued*

Filter	HJD $-2,400,000$	F_λ (10^{-15}erg cm^{-2} s^{-1} Å^{-1})	σ_{F_λ}	Telescope ID (as in Table 1)	Differential Counts (DC) (reference counts)	error DC (reference counts)
i	56762.78636	10.162	0.0318	LCOGT1	-14693.0	1702.2
i	56763.75427	10.142	0.0318	LCOGT1	-15760.0	1701.2
i	56764.78767	10.157	0.0399	LCOGT1	-14928.0	2134.3
i	56765.54046	10.193	0.0271	LCOGT4	-13029.0	1448.4
i	56765.58278	10.163	0.0109	LT	-14608.0	582.17
i	56765.87757	10.13	0.0378	LCOGT1	-16393.0	2019.2
i	56766.40167	10.072	0.0356	LCOGT4	-19474.0	1905.4
i	56770.52673	10.251	0.0133	LT	-9915.9	711.69
i	56770.78276	10.251	0.0474	LCOGT1	-9916.4	2536.3
i	56771.51136	10.229	0.0133	LT	-11084.0	713.02
i	56772.49803	10.284	0.0074	LT	-8135.3	398.11
i	56772.82719	10.347	0.0688	LCOGT1	-4810.0	3680.3
i	56773.38964	10.354	0.0551	LCOGT4	-4412.4	2946.7
i	56773.85849	10.367	0.0655	LCOGT1	-3712.9	3502.6
i	56774.76119	10.403	0.1159	LCOGT1	-1800.7	6197.8
i	56775.40695	10.443	0.0526	LCOGT4	319.5	2812.8
i	56775.54837	10.462	0.0083	LT	1342.2	441.85
i	56776.07733	10.515	0.1051	LCOGT6	4186.8	5623.7
i	56776.46341	10.469	0.0076	LT	1716.8	404.54
i	56777.53027	10.468	0.0122	LT	1698.9	654.31
i	56778.49734	10.451	0.0133	LT	756.6	710.85
i	56779.39614	10.45	0.0459	LCOGT2	734.23	2456.3
i	56779.48718	10.426	0.011	LT	-549.71	586.32
i	56779.85183	10.364	0.065	LCOGT1	-3906.2	3476.4
i	56780.49464	10.415	0.0134	LT	-1149.5	717.19
i	56780.81441	10.399	0.0608	LCOGT1	-2010.2	3251.2
i	56781.49383	10.414	0.0134	LT	-1221.5	717.33
i	56782.44705	10.339	0.0132	LT	-5238.9	706.63
i	56782.7402	10.358	0.0757	LCOGT1	-4194.2	4050.0
i	56783.45189	10.321	0.013	LT	-6207.7	692.76
i	56784.44117	10.343	0.013	LT	-4999.5	696.72
i	56785.47585	10.354	0.0113	LT	-4407.9	602.97
i	56786.48274	10.373	0.0101	LT	-3388.7	540.46
i	56787.40373	10.346	0.0081	LT	-4830.0	432.49
i	56790.45933	10.298	0.0089	LT	-7393.9	476.8
i	56792.40286	10.234	0.0064	LT	-10816.0	343.16
i	56793.4653	10.263	0.0115	LT	-9285.9	615.84
i	56794.46365	10.327	0.0139	LT	-5841.6	743.06
i	56795.44566	10.266	0.0137	LT	-9145.4	730.44
i	56796.44806	10.299	0.0162	LT	-7377.5	867.35
i	56797.45075	10.342	0.0157	LT	-5059.7	841.52
i	56798.44366	10.344	0.0166	LT	-4947.2	886.07
i	56799.44057	10.388	0.0157	LT	-2573.3	839.12
i	56800.44296	10.346	0.0126	LT	-4860.8	675.09
i	56801.42747	10.319	0.0112	LT	-6294.4	599.05
i	56802.43701	10.336	0.0098	LT	-5370.9	524.14
i	56803.44075	10.358	0.0141	LT	-4208.6	755.81
i	56805.46065	10.323	0.0167	LT	-6089.5	892.73
i	56806.43379	10.272	0.0103	LT	-8816.3	550.14
i	56807.43561	10.338	0.0126	LT	-5251.7	672.5
i	56808.4151	10.356	0.0146	LT	-4320.0	781.17
i	56809.43	10.365	0.0131	LT	-3811.7	703.3
i	56810.43131	10.381	0.0147	LT	-2996.8	785.33
i	56811.42008	10.372	0.015	LT	-3469.0	800.68
i	56812.43007	10.398	0.0134	LT	-2052.5	715.66
i	56813.40298	10.392	0.0172	LT	-2363.9	922.5
i	56815.40381	10.443	0.0166	LT	352.09	888.58
i	56816.27751	10.523	0.0273	LCOGT4	4616.9	1461.7
i	56816.41077	10.476	0.0146	LT	2082.8	780.58
i	56816.64306	10.492	0.0564	LCOGT1	2985.8	3015.7
i	56817.41079	10.489	0.0135	LT	2828.0	724.75
i	56817.83763	10.501	0.0461	LCOGT1	3421.6	2465.7
i	56818.41563	10.635	0.0123	LT	10602.0	660.13
i	56819.27574	10.607	0.0257	LCOGT4	9127.0	1376.8
i	56819.41571	10.671	0.0133	LT	12523.0	709.06
i	56820.48486	10.676	0.0107	LT	12817.0	572.69
i	56821.24589	10.73	0.0314	LCOGT4	15716.0	1678.6
i	56822.39635	10.768	0.0118	LT	17741.0	628.95
i	56823.40732	10.863	0.0163	LT	22824.0	872.7
i	56824.40115	10.826	0.0174	LT	20808.0	929.44
i	56825.30887	10.887	0.0534	LCOGT4	24103.0	2858.1
i	56825.41508	10.888	0.0184	LT	24140.0	984.27
i	56826.39287	10.736	0.0181	LT	16025.0	968.75
i	56827.39764	10.696	0.0162	LT	13890.0	864.26
i	56828.39997	10.676	0.0167	LT	12781.0	891.01
i	56829.40979	10.648	0.0159	LT	11306.0	851.27
i	56830.40255	10.616	0.0183	LT	9587.9	977.32
i	56831.39396	10.419	0.0163	LT	-936.19	873.9

Table 8 — *Continued*

Filter	HJD $-2,400,000$	F_λ (10^{-15}erg cm^{-2} s^{-1} Å^{-1})	σ_{F_λ}	Telescope ID (as in Table 1)	Differential Counts (DC) (reference counts)	error DC (reference counts)
i	56832.43681	10.473	0.0154	LT	1960.4	821.69
i	56833.39816	10.512	0.0161	LT	4043.1	862.55
i	56834.39275	10.565	0.0143	LT	6885.4	762.65
i	56835.3942	10.492	0.0153	LT	2943.1	820.14
i	56839.33995	10.496	0.0397	LCOGT2	3188.1	2121.7
i	56841.41209	10.514	0.015	LT	4158.3	801.59
i	56842.24887	10.486	0.0439	LCOGT4	2666.3	2349.1
i	56843.21908	10.442	0.0413	LCOGT4	293.23	2208.4
i	56843.39193	10.488	0.0152	LT	2730.8	812.15
i	56845.41125	10.415	0.0164	LT	-1141.3	878.14
i	56847.40192	10.284	0.012	LT	-8178.5	644.39
i	56848.39146	10.219	0.0084	LT	-11612.0	449.08
i	56848.858	10.252	0.0658	LCOGT6	-9858.3	3516.9
i	56850.25912	10.311	0.0295	LCOGT2	-6719.8	1577.1
i	56858.38847	10.166	0.0166	LT	-14447.0	889.27
i	56860.3874	10.135	0.019	LT	-16133.0	1017.7
i	56861.38644	10.197	0.0133	LT	-12800.0	709.36
i	56862.38698	10.128	0.0172	LT	-16490.0	921.74
i	56863.3854	10.119	0.0155	LT	-17001.0	830.02
i	56864.38541	10.245	0.0187	LT	-10247.0	1000.3
i	56864.695	10.165	0.0867	LCOGT1	-14535.0	4636.4
i	56865.38436	10.165	0.0164	LT	-14521.0	877.48
i	56865.63489	10.161	0.0885	LCOGT1	-14736.0	4735.9
i	56866.38376	10.283	0.0177	LT	-8210.4	944.81
i	56867.38358	10.332	0.0148	LT	-5592.3	793.67
i	56868.38409	10.324	0.0143	LT	-6002.3	764.7
i	56868.8643	10.318	0.1591	LCOGT6	-6364.1	8512.3
i	56869.38346	10.369	0.0151	LT	-3597.1	807.56
i	56869.87351	10.401	0.1133	LCOGT6	-1887.1	6059.2
i	56871.38162	10.397	0.0128	LT	-2091.1	685.22
i	56871.86428	10.35	0.0725	LCOGT6	-4649.7	3880.2
i	56872.38054	10.463	0.0124	LT	1410.6	664.31
i	56873.38051	10.489	0.0166	LT	2823.7	885.34
i	56874.37907	10.445	0.0136	LT	472.82	725.62
i	56875.37977	10.44	0.0116	LT	158.27	619.86
i	56878.37774	10.496	0.014	LT	3195.9	749.42
i	56879.37517	10.517	0.0102	LT	4321.8	548.14
i	56880.37465	10.72	0.0133	LT	15149.0	710.42
i	56883.37925	10.885	0.0167	LT	23959.0	892.06
i	56884.37203	10.889	0.0171	LT	24194.0	912.49
i	56885.37119	10.901	0.0134	LT	24854.0	716.05
i	56886.36968	10.874	0.0172	LT	23392.0	917.58
i	56887.36929	10.795	0.0122	LT	19186.0	650.58
i	56891.36634	10.985	0.0169	LT	29325.0	904.4
i	56892.3666	10.963	0.0146	LT	28179.0	781.96
i	56893.36573	10.96	0.0141	LT	28017.0	756.65
i	56894.37057	10.891	0.0134	LT	24287.0	714.35
i	56895.36324	10.86	0.0149	LT	22636.0	794.79
I	56645.62899	8.6661	0.0116	WC18	-6575.6	499.37
I	56646.63385	8.7482	0.017	WC18	-3043.8	732.31
I	56647.64453	8.6892	0.0163	WC18	-5582.9	702.53
I	56648.6075	8.5573	0.0423	WC18	-11250.0	1817.0
I	56650.56419	8.5255	0.0204	WC18	-12615.0	875.19
I	56650.63725	8.4196	0.1978	CrAO	-17167.0	8501.3
I	56651.65375	8.5419	0.1351	CrAO	-11913.0	5807.8
I	56653.61119	8.6773	0.0192	WC18	-6091.5	824.98
I	56655.52326	8.502	0.0138	WC18	-13626.0	591.18
I	56656.54322	8.5077	0.0156	WC18	-13380.0	670.59
I	56661.63974	8.4043	0.1285	CrAO	-17825.0	5522.3
I	56666.60979	8.3767	0.0258	WC18	-19014.0	1108.4
I	56670.59178	8.5868	0.0633	WC18	-9981.8	2721.9
I	56674.58267	8.5999	0.0154	WC18	-9420.4	662.33
I	56682.59955	8.8633	0.0135	WC18	1900.3	581.56
I	56684.59957	8.882	0.0244	WC18	2705.8	1050.6
I	56686.62652	8.9058	0.0203	WC18	3727.7	873.4
I	56688.51505	8.8102	0.0262	WC18	-381.71	1127.5
I	56691.57709	8.8307	0.1011	CrAO	501.21	4344.7
I	56691.60323	8.7317	0.027	WC18	-3753.4	1158.7
I	56692.59282	8.8029	0.122	CrAO	-694.01	5244.6
I	56693.60115	8.6513	0.1255	CrAO	-7209.7	5392.2
I	56697.56501	8.9278	0.0277	WC18	4675.2	1190.8
I	56698.54819	8.9709	0.0259	WC18	6528.4	1113.0
I	56699.47976	8.8364	0.0205	WC18	745.56	881.64
I	56700.50659	8.8091	0.0206	WC18	-429.7	884.08
I	56701.56881	8.8869	0.0248	WC18	2916.1	1066.3
I	56702.54189	8.9436	0.0176	WC18	5351.7	757.96
I	56708.5731	9.057	0.0443	WC18	10227.0	1903.7
I	56709.55489	9.0211	0.021	WC18	8685.4	902.96

Table 8 — *Continued*

Filter	HJD $-2,400,000$	F_λ (10^{-15}erg cm^{-2} s^{-1} Å^{-1})	σ_{F_λ}	Telescope ID (as in Table 1)	Differential Counts (DC) (reference counts)	error DC (reference counts)
I	56710.48332	8.9276	0.0194	WC18	4665.1	835.95
I	56711.60397	8.7975	0.1132	CrAO	-927.19	4866.3
I	56714.47459	8.8213	0.0186	WC18	97.65	799.01
I	56716.48488	8.7184	0.0248	WC18	-4328.2	1064.8
I	56721.48007	8.3886	0.0219	WC18	-18501.0	940.22
I	56723.45793	8.1715	0.0193	WC18	-27831.0	831.41
I	56724.62954	8.1366	0.1258	CrAO	-29333.0	5408.3
I	56726.63023	8.2353	0.2102	CrAO	-25092.0	9036.5
I	56727.4607	8.1925	0.022	WC18	-26930.0	944.16
I	56727.60898	8.2072	0.1777	CrAO	-26298.0	7637.9
I	56728.62722	8.203	0.163	CrAO	-26480.0	7005.2
I	56729.61621	8.227	0.1482	CrAO	-25445.0	6368.3
I	56730.5713	8.1727	0.1381	CrAO	-27780.0	5937.0
I	56732.50843	8.1692	0.0156	WC18	-27931.0	668.86
I	56737.52364	8.5637	0.0146	WC18	-10976.0	628.92
I	56738.45493	8.6607	0.0143	WC18	-6805.7	614.3
I	56738.58392	8.4869	0.1423	CrAO	-14275.0	6116.2
I	56739.3169	8.564	0.0193	WC18	-10961.0	827.8
I	56739.59695	8.4919	0.119	CrAO	-14060.0	5116.2
I	56740.57789	8.7901	0.091	CrAO	-1242.8	3912.6
I	56741.52756	8.9782	0.108	CrAO	6841.9	4641.9
I	56742.45516	8.915	0.0191	WC18	4122.6	822.26
I	56744.4487	9.0916	0.0183	WC18	11713.0	787.91
I	56746.43172	9.2889	0.1126	CrAO	20194.0	4841.8
I	56747.45091	9.2676	0.0853	CrAO	19280.0	3667.1
I	56748.47765	9.2453	0.0152	WC18	18321.0	652.41
I	56748.5421	9.1905	0.0888	CrAO	15963.0	3817.6
I	56750.35261	9.3011	0.0208	WC18	20720.0	892.02
I	56752.42031	9.3049	0.0261	WC18	20882.0	1122.5
I	56753.36861	9.2474	0.0242	WC18	18412.0	1038.3
I	56754.37718	9.176	0.0157	WC18	15340.0	674.79
I	56755.43128	9.0675	0.0366	WC18	10679.0	1571.3
I	56757.34955	9.1152	0.0227	WC18	12730.0	976.1
I	56758.44495	8.9878	0.0219	WC18	7251.9	939.78
I	56762.45281	8.6906	0.1372	CrAO	-5519.5	5899.0
I	56763.43267	8.785	0.1618	CrAO	-1463.7	6952.3
I	56765.31162	8.8668	0.014	WC18	2050.9	603.38
I	56765.51415	8.7722	0.0896	CrAO	-2013.0	3852.6
I	56766.29921	8.8558	0.02	WC18	1580.5	861.55
I	56774.53174	9.1516	0.1134	CrAO	14293.0	4874.9
I	56784.46906	9.1553	0.1088	CrAO	14453.0	4675.0
I	56793.50084	8.998	0.1491	CrAO	7691.1	6407.1
I	56799.36255	9.084	0.0959	CrAO	11387.0	4122.7
I	56800.4099	9.1075	0.0598	WC18	12398.0	2571.8
I	56800.46214	9.1848	0.1207	CrAO	15721.0	5185.9
I	56801.4339	8.9689	0.0122	WC18	6438.8	523.49
I	56802.36572	8.9536	0.0166	WC18	5780.7	711.56
I	56803.34639	9.0135	0.0236	WC18	8358.0	1015.3
I	56804.40722	8.9891	0.0107	WC18	7308.2	458.99
I	56810.34151	9.0305	0.027	WC18	9089.4	1161.2
I	56811.34127	9.0377	0.0181	WC18	9396.4	779.8
I	56815.37378	9.0767	0.0145	WC18	11073.0	625.31
I	56817.36559	9.143	0.0215	WC18	13925.0	924.82
I	56817.42263	9.0437	0.1049	CrAO	9655.3	4510.3
I	56818.37315	9.3889	0.158	CrAO	24491.0	6793.2
I	56819.43436	9.1493	0.1216	CrAO	14195.0	5224.2
I	56820.32712	9.252	0.0124	WC18	18606.0	531.6
I	56822.31831	9.2788	0.0188	WC18	19762.0	805.95
I	56822.40327	9.3468	0.0941	CrAO	22682.0	4043.3
I	56823.35584	9.2709	0.0094	WC18	19421.0	402.09
I	56823.39872	9.2605	0.1411	CrAO	18974.0	6065.5
I	56824.37306	9.2278	0.0796	CrAO	17568.0	3419.7
I	56824.38	9.3354	0.0096	WC18	22194.0	411.06
I	56825.35932	9.337	0.0103	WC18	22263.0	441.52
I	56827.38256	9.2479	0.0172	WC18	18433.0	741.13
I	56829.31543	9.2087	0.0222	WC18	16747.0	954.1
I	56831.29218	9.019	0.0293	WC18	8591.6	1257.6
I	56832.28555	9.0169	0.0254	WC18	8501.3	1092.5
I	56834.33571	9.0397	0.032	WC18	9481.2	1374.0
I	56834.40176	9.2469	0.0967	CrAO	18389.0	4157.7
I	56835.41899	9.1293	0.1381	CrAO	13335.0	5935.8
I	56836.32377	9.0264	0.0179	WC18	8913.5	768.7
I	56837.32461	9.0328	0.0176	WC18	9186.7	756.89
I	56837.41188	9.1002	0.1468	CrAO	12082.0	6309.5
I	56839.32787	9.0474	0.0182	WC18	9815.3	783.46
I	56844.37396	9.0582	0.0172	WC18	10277.0	739.43
I	56845.28505	8.9892	0.0108	WC18	7312.5	462.79
I	56846.34474	8.972	0.0076	WC18	6574.6	325.97

Table 8 — *Continued*

Filter	HJD $-2,400,000$	F_λ (10^{-15}erg cm^{-2} s^{-1} Å^{-1})	σ_{F_λ}	Telescope ID (as in Table 1)	Differential Counts (DC) (reference counts)	error DC (reference counts)
I	56848.28752	8.7447	0.0542	WC18	-3193.8	2330.7
I	56850.30477	8.8867	0.0159	WC18	2905.3	681.42
I	56852.28952	8.8324	0.0105	WC18	572.17	450.26
I	56853.31874	8.7353	0.0303	WC18	-3598.5	1302.3
I	56854.31157	8.6959	0.0249	WC18	-5294.1	1071.0
I	56857.26244	8.7292	0.017	WC18	-3861.1	729.25
I	56858.29799	8.7835	0.0148	WC18	-1527.5	636.95
I	56859.33924	8.8252	0.0142	WC18	262.12	609.48
I	56866.32379	8.7963	0.0202	WC18	-976.92	868.15
I	56867.29323	8.9316	0.0134	WC18	4838.7	576.42
I	56869.28987	8.9157	0.0125	WC18	4151.9	537.62
z	56684.77831	9.3003	0.0393	LT	-4697.2	984.0
z	56685.78408	9.3354	0.0079	LT	-3818.5	197.04
z	56686.76934	9.3816	0.0404	LT	-2659.7	1013.4
z	56689.01963	9.3364	0.0533	LCOGT1	-3791.8	1335.9
z	56689.84228	9.2154	0.0528	LCOGT1	-6824.3	1322.8
z	56692.95051	9.2215	0.0437	LCOGT1	-6671.7	1095.8
z	56693.62004	9.2243	0.0884	LCOGT4	-6601.7	2215.9
z	56693.78797	9.1997	0.0072	LT	-7218.5	179.95
z	56694.76852	9.2227	0.0152	LT	-6641.5	381.78
z	56695.70791	9.2849	0.0116	LT	-5082.5	291.86
z	56696.25411	9.3547	0.0825	LCOGT5	-3332.5	2069.0
z	56696.72636	9.2685	0.0224	LT	-5493.9	561.72
z	56696.98562	9.3519	0.066	LCOGT1	-3404.9	1655.1
z	56697.7552	9.2937	0.008	LT	-4861.6	200.51
z	56698.61127	9.3296	0.1866	LCOGT2	-3962.1	4677.5
z	56698.71582	9.281	0.0112	LT	-5180.7	280.14
z	56699.27618	9.3444	0.0843	LCOGT5	-3591.4	2114.1
z	56699.71145	9.3387	0.0323	LT	-3734.9	808.75
z	56700.60128	9.483	0.0589	LCOGT4	-117.11	1477.0
z	56700.69001	9.3917	0.0075	LT	-2404.9	186.97
z	56701.5643	9.3415	0.0212	LT	-3665.5	530.21
z	56701.60555	9.3711	0.1233	LCOGT4	-2922.5	3089.7
z	56701.83475	9.3332	0.0527	LCOGT1	-3873.0	1321.2
z	56702.63675	9.3589	0.008	LT	-3227.9	201.29
z	56703.01786	9.3627	0.0784	LCOGT1	-3133.5	1965.7
z	56703.88342	9.4014	0.0421	LCOGT1	-2163.8	1054.5
z	56704.84045	9.4314	0.0525	LCOGT1	-1411.1	1316.9
z	56705.61145	9.4912	0.0595	LCOGT4	88.66	1492.6
z	56705.95446	9.4135	0.0548	LCOGT1	-1860.5	1373.2
z	56706.98401	9.5181	0.0581	LCOGT1	761.03	1456.7
z	56708.02631	9.4026	0.0779	LCOGT1	-2133.1	1951.9
z	56709.83031	9.3931	0.0745	LCOGT1	-2370.5	1868.1
z	56710.66026	9.37	0.0137	LT	-2949.2	343.13
z	56711.01908	9.4054	0.0846	LCOGT1	-2062.0	2120.0
z	56711.6845	9.3353	0.0115	LT	-3820.2	288.62
z	56711.92532	9.3897	0.0457	LCOGT1	-2455.4	1146.4
z	56713.26886	9.2114	0.0823	LCOGT5	-6924.8	2063.4
z	56713.7208	9.2876	0.0089	LT	-5016.6	222.58
z	56713.92148	9.262	0.0493	LCOGT1	-5658.0	1236.5
z	56714.72536	9.2795	0.0115	LT	-5219.5	287.81
z	56715.28224	9.2284	0.1339	LCOGT5	-6498.5	3356.0
z	56715.91469	9.3218	0.0598	LCOGT1	-4157.0	1499.9
z	56716.64347	9.1745	0.0876	LCOGT4	-7849.5	2196.2
z	56716.6656	9.2189	0.0106	LT	-6736.8	266.19
z	56717.73427	9.1761	0.0103	LT	-7809.9	258.05
z	56717.95799	9.1675	0.0941	LCOGT1	-8026.3	2358.9
z	56718.56656	9.0982	0.0975	LCOGT4	-9762.2	2444.5
z	56718.67168	9.1318	0.0106	LT	-8921.9	266.33
z	56719.60622	8.8319	0.5959	LCOGT2	-16437.0	14938.0
z	56720.69328	9.0444	0.0118	LT	-11112.0	296.82
z	56721.71496	8.9802	0.0102	LT	-12720.0	254.72
z	56722.73892	8.9121	0.0115	LT	-14428.0	287.36
z	56723.57238	8.8897	0.0112	LT	-14990.0	280.66
z	56726.17377	8.8643	0.0862	LCOGT5	-15627.0	2160.0
z	56727.15317	8.8556	0.1066	LCOGT5	-15845.0	2672.8
z	56727.61622	8.7806	0.0962	LCOGT4	-17724.0	2410.8
z	56728.57721	8.9119	0.01	LT	-14432.0	250.91
z	56729.49614	8.8292	0.0094	LT	-16505.0	236.57
z	56730.53906	8.8198	0.0093	LT	-16741.0	234.36
z	56730.83303	8.7772	0.08	LCOGT1	-17808.0	2005.9
z	56732.49544	8.9109	0.0107	LT	-14458.0	268.54
z	56733.48574	8.9315	0.0103	LT	-13942.0	257.71
z	56733.80348	8.8256	0.0698	LCOGT1	-16595.0	1749.7
z	56734.48114	8.8854	0.0096	LT	-15097.0	239.55
z	56735.49921	8.9542	0.0099	LT	-13373.0	248.36
z	56735.86208	9.0394	0.1087	LCOGT1	-11238.0	2724.4
z	56736.50541	8.9966	0.0099	LT	-12310.0	248.61

Table 8 — *Continued*

Filter	HJD $-2,400,000$	F_λ (10^{-15}erg cm^{-2} s^{-1} Å^{-1})	σ_{F_λ}	Telescope ID (as in Table 1)	Differential Counts (DC) (reference counts)	error DC (reference counts)
z	56736.7747	9.0315	0.0751	LCOGT1	-11434.0	1881.6
z	56737.49025	9.0435	0.0098	LT	-11133.0	244.78
z	56740.61839	9.2149	0.0108	LT	-6836.7	271.53
z	56740.86453	9.3118	0.1086	LCOGT1	-4408.1	2723.0
z	56741.6126	9.2427	0.0108	LT	-6140.2	271.01
z	56741.71889	9.3448	0.0913	LCOGT1	-3582.1	2287.3
z	56743.59684	9.4699	0.0125	LT	-446.08	312.8
z	56744.5392	9.5105	0.0125	LT	572.73	312.76
z	56744.70091	9.5164	0.0819	LCOGT1	718.83	2052.5
z	56746.81946	9.5486	0.0559	LCOGT1	1526.3	1402.2
z	56748.75962	9.6146	0.0737	LCOGT1	3181.7	1846.8
z	56749.75678	9.6225	0.055	LCOGT1	3378.2	1379.3
z	56751.98521	9.5725	0.0622	LCOGT1	2126.0	1558.3
z	56752.58298	9.7096	0.0142	LT	5561.5	355.01
z	56753.57796	9.6788	0.0141	LT	4790.2	354.38
z	56754.55564	9.5786	0.015	LT	2279.0	374.98
z	56755.56524	9.5203	0.0107	LT	817.52	269.05
z	56755.98052	9.4737	0.1043	LCOGT1	-350.6	2613.9
z	56756.51256	9.5404	0.0109	LT	1322.2	273.05
z	56758.74938	9.4571	0.0721	LCOGT1	-766.19	1807.7
z	56759.88906	9.4253	0.0402	LCOGT1	-1563.8	1008.1
z	56762.78827	9.3001	0.047	LCOGT1	-4701.7	1178.3
z	56763.75624	9.2523	0.0488	LCOGT1	-5900.2	1224.3
z	56764.53775	9.4457	0.0829	LCOGT4	-1051.8	2078.0
z	56764.78939	9.3346	0.0548	LCOGT1	-3837.9	1372.4
z	56765.53431	9.2924	0.0863	LCOGT4	-4895.9	2162.8
z	56765.58342	9.296	0.0109	LT	-4804.5	273.84
z	56765.87186	9.3744	0.076	LCOGT1	-2840.2	1904.6
z	56768.074	9.1989	0.0781	LCOGT5	-7238.0	1957.1
z	56770.52737	9.4039	0.0139	LT	-2101.2	348.13
z	56770.7847	9.3796	0.0549	LCOGT1	-2709.3	1375.8
z	56771.17647	9.4294	0.1246	LCOGT5	-1460.3	3123.0
z	56771.512	9.3576	0.0142	LT	-3259.7	355.57
z	56772.16729	9.4459	0.1032	LCOGT5	-1048.2	2585.5
z	56772.49866	9.3926	0.0117	LT	-2384.0	293.06
z	56772.82913	9.4191	0.073	LCOGT1	-1719.0	1829.3
z	56773.39155	9.419	0.0996	LCOGT4	-1720.7	2496.4
z	56773.86028	9.4308	0.073	LCOGT1	-1426.7	1830.8
z	56774.76257	9.4423	0.1157	LCOGT1	-1138.9	2900.2
z	56775.40886	9.4651	0.095	LCOGT4	-566.64	2381.9
z	56775.54899	9.5143	0.0104	LT	667.09	260.52
z	56777.53091	9.4941	0.0127	LT	159.66	319.32
z	56778.49798	9.4573	0.0139	LT	-762.63	347.81
z	56779.39565	9.4133	0.2064	LCOGT2	-1864.4	5174.7
z	56779.48781	9.4793	0.0132	LT	-210.77	330.75
z	56779.85195	9.4202	0.0621	LCOGT1	-1692.7	1555.5
z	56780.49527	9.4598	0.0127	LT	-698.73	317.6
z	56780.81386	9.4527	0.065	LCOGT1	-877.24	1628.6
z	56781.49447	9.4549	0.0136	LT	-821.21	341.9
z	56782.44769	9.3323	0.0121	LT	-3895.4	304.43
z	56782.73968	9.4342	0.0801	LCOGT1	-1340.4	2008.3
z	56783.45253	9.4113	0.0125	LT	-1915.5	313.05
z	56784.44181	9.3849	0.0145	LT	-2576.7	362.81
z	56785.47648	9.4683	0.0102	LT	-486.03	254.99
z	56786.48337	9.3995	0.0096	LT	-2210.4	241.55
z	56787.40437	9.321	0.011	LT	-4177.6	275.93
z	56790.45996	9.3759	0.0094	LT	-2801.5	236.04
z	56792.40349	9.4213	0.0116	LT	-1663.6	290.66
z	56793.46594	9.3843	0.0113	LT	-2592.0	283.34
z	56794.46428	9.3416	0.014	LT	-3662.9	350.6
z	56795.4463	9.3589	0.0127	LT	-3227.8	319.5
z	56796.4487	9.3882	0.0147	LT	-2494.7	369.7
z	56797.45139	9.374	0.0149	LT	-2849.3	373.39
z	56798.4443	9.4144	0.0156	LT	-1837.8	391.75
z	56799.44121	9.4507	0.014	LT	-925.94	350.2
z	56800.4436	9.4239	0.0124	LT	-1599.4	310.73
z	56801.42812	9.4086	0.0124	LT	-1983.4	310.76
z	56802.43765	9.4191	0.0107	LT	-1719.8	266.99
z	56803.44162	9.3911	0.0136	LT	-2420.0	340.2
z	56805.46152	9.379	0.0138	LT	-2724.0	346.27
z	56806.43467	9.3465	0.0152	LT	-3539.0	380.04
z	56807.43648	9.3667	0.0133	LT	-3032.7	333.48
z	56808.41596	9.4057	0.0129	LT	-2056.0	323.05
z	56809.43087	9.3919	0.0134	LT	-2400.8	337.01
z	56810.43219	9.3999	0.0147	LT	-2201.3	368.85
z	56811.42096	9.457	0.0137	LT	-769.7	343.44
z	56812.43093	9.4513	0.0136	LT	-913.04	340.79
z	56813.40385	9.3901	0.0165	LT	-2446.7	413.57

Table 8 — *Continued*

Filter	HJD $-2,400,000$	F_λ (10^{-15}erg cm^{-2} s^{-1} Å^{-1})	σ_{F_λ}	Telescope ID (as in Table 1)	Differential Counts (DC) (reference counts)	error DC (reference counts)
z	56814.45707	9.4019	0.0135	LT	-2150.5	339.27
z	56815.40467	9.4604	0.0165	LT	-684.77	413.32
z	56816.28071	9.5324	0.0886	LCOGT4	1121.0	2221.4
z	56816.41164	9.4812	0.0147	LT	-161.8	368.7
z	56816.64794	9.4722	0.0708	LCOGT1	-387.88	1775.9
z	56817.41166	9.4202	0.0165	LT	-1691.2	414.42
z	56817.8423	9.538	0.0587	LCOGT1	1261.9	1472.0
z	56818.41649	9.5529	0.0143	LT	1634.6	358.44
z	56819.28041	9.5522	0.0573	LCOGT4	1617.3	1437.5
z	56819.41658	9.5899	0.0131	LT	2561.1	328.61
z	56820.48573	9.6675	0.0133	LT	4506.5	333.04
z	56821.25057	9.647	0.0658	LCOGT4	3993.6	1649.2
z	56822.39721	9.684	0.0147	LT	4919.8	368.89
z	56823.40819	9.762	0.0168	LT	6875.2	421.98
z	56824.40202	9.7451	0.0167	LT	6451.1	417.62
z	56825.31354	9.6372	0.0916	LCOGT4	3746.4	2295.4
z	56825.41596	9.7583	0.0154	LT	6783.3	386.19
z	56826.29969	9.6842	0.2021	LCOGT2	4925.8	5065.5
z	56826.39374	9.6636	0.0167	LT	4409.4	418.14
z	56827.39851	9.6331	0.0176	LT	3644.7	441.67
z	56828.40084	9.6249	0.0152	LT	3438.1	382.22
z	56829.41066	9.588	0.0136	LT	2515.6	340.39
z	56830.40342	9.562	0.0147	LT	1863.7	368.13
z	56831.39483	9.4967	0.0155	LT	225.84	387.29
z	56832.43768	9.477	0.0145	LT	-266.75	364.45
z	56833.39903	9.5207	0.0135	LT	826.59	339.31
z	56835.39508	9.4231	0.0154	LT	-1618.8	386.04
z	56837.24062	9.4664	0.2379	LCOGT2	-533.59	5962.7
z	56837.76067	9.4491	0.0864	LCOGT1	-967.78	2166.9
z	56839.34463	9.5025	0.1417	LCOGT2	371.67	3552.8
z	56841.41295	9.4424	0.0134	LT	-1134.8	336.41
z	56842.25356	9.5093	0.0952	LCOGT4	541.77	2386.6
z	56843.22377	9.4775	0.0854	LCOGT4	-255.96	2140.9
z	56843.3928	9.5532	0.0155	LT	1641.6	388.66
z	56845.41212	9.4557	0.0162	LT	-802.88	406.83
z	56848.39233	9.418	0.0151	LT	-1746.4	378.25
z	56850.26382	9.349	0.194	LCOGT2	-3476.9	4862.5
z	56858.38934	9.2652	0.0164	LT	-5576.0	411.57
z	56860.38827	9.3598	0.0188	LT	-3206.6	471.15
z	56861.3873	9.3412	0.0145	LT	-3672.8	363.1
z	56862.38784	9.3544	0.0188	LT	-3341.1	472.44
z	56863.38626	9.3719	0.0175	LT	-2903.6	439.19
z	56864.38627	9.2316	0.0177	LT	-6418.1	443.38
z	56864.6997	9.2761	0.0901	LCOGT1	-5302.7	2259.0
z	56865.38523	9.3475	0.0164	LT	-3512.9	411.35
z	56865.63955	9.2891	0.096	LCOGT1	-4977.1	2406.7
z	56866.38463	9.3865	0.0171	LT	-2536.5	428.76
z	56867.38444	9.3658	0.0155	LT	-3056.1	387.48
z	56868.38512	9.4058	0.0155	LT	-2052.1	387.55
z	56869.38449	9.447	0.0135	LT	-1019.3	338.69
z	56871.38265	9.5074	0.0134	LT	493.63	336.38
z	56872.38159	9.4437	0.0139	LT	-1101.4	348.5
z	56873.38155	9.5134	0.0162	LT	643.54	407.19
z	56874.38011	9.3959	0.0179	LT	-2301.2	449.07
z	56878.37878	9.469	0.0151	LT	-468.35	379.54
z	56879.37621	9.3982	0.0129	LT	-2244.3	323.08
z	56880.37568	9.6746	0.0133	LT	4684.9	333.39
z	56883.38029	9.7505	0.0154	LT	6588.3	385.46
z	56884.37307	9.7778	0.0155	LT	7272.7	389.56
z	56885.37222	9.8054	0.0139	LT	7964.0	347.6
z	56886.37073	9.8047	0.0151	LT	7946.3	379.51
z	56887.37033	9.7637	0.0135	LT	6919.1	339.28
z	56891.36737	9.8454	0.0164	LT	8966.1	411.24
z	56892.36763	9.8435	0.0156	LT	8919.2	392.23
z	56893.36678	9.8931	0.0146	LT	10163.0	365.03
z	56894.3716	9.7868	0.0138	LT	7497.6	344.99
z	56895.36427	9.7792	0.0148	LT	7306.7	371.67

Table 9
HST Continuum Light Curves

Wavelength (Å)	HJD −2,400,000	F_λ (10^{-15}erg cm^{-2} s^{-1} Å^{-1})	σ_{F_λ}
1157.5	56690.61	32.4	0.89
1157.5	56691.54	34.8	0.92
1157.5	56692.39	37.5	0.95
1157.5	56693.32	39.1	0.98
1157.5	56695.27	41.1	0.99
1157.5	56696.25	45.9	1.05
1157.5	56697.31	48.7	1.08
1157.5	56698.3	52.5	1.13
1157.5	56699.23	49.3	1.1
1157.5	56700.23	48.3	1.08
1157.5	56701.36	49.0	1.08
1157.5	56702.16	51.1	1.11
1157.5	56703.15	52.8	1.13
1157.5	56705.34	49.0	1.09
1157.5	56706.21	46.8	1.06
1157.5	56707.2	49.2	1.08
1157.5	56708.26	43.4	1.02
1157.5	56709.26	40.7	0.99
1157.5	56710.26	35.1	0.92
1157.5	56711.12	31.0	0.88
1157.5	56712.18	32.7	0.9
1157.5	56713.18	32.4	0.89
1157.5	56714.24	31.5	0.88
1157.5	56715.04	28.3	0.84
1157.5	56715.9	27.5	0.83
1157.5	56716.84	25.2	0.81
1157.5	56718.83	23.2	0.77
1157.5	56720.15	21.5	0.76
1157.5	56721.02	19.4	0.73
1157.5	56722.09	18.7	0.72
1157.5	56723.14	17.8	0.72
1157.5	56726.06	20.5	0.74
1157.5	56727.06	18.2	0.71
1157.5	56727.79	19.4	0.73
1157.5	56728.92	19.8	0.74
1157.5	56729.78	21.2	0.75
1157.5	56730.85	21.1	0.75
1157.5	56731.97	20.7	0.75
1157.5	56732.91	20.2	0.74
1157.5	56733.85	22.1	0.76
1157.5	56734.84	25.4	0.81
1157.5	56735.85	32.0	0.89
1157.5	56736.44	36.9	0.94
1157.5	56737.69	38.5	0.96
1157.5	56738.5	40.2	0.98
1157.5	56739.68	46.3	1.05
1157.5	56740.36	50.0	1.11
1157.5	56741.35	46.4	1.06
1157.5	56744.4	59.0	1.2
1157.5	56745.25	57.7	1.19
1157.5	56746.25	57.1	1.18
1157.5	56747.18	59.8	1.21
1157.5	56748.24	60.1	1.21
1157.5	56749.17	55.9	1.16
1157.5	56750.3	53.4	1.13
1157.5	56751.16	50.5	1.1
1157.5	56752.02	49.8	1.1
1157.5	56753.02	39.3	0.97
1157.5	56753.97	32.8	0.89
1157.5	56755.21	32.0	0.89
1157.5	56756.14	33.4	0.9
1157.5	56757.14	34.8	0.92
1157.5	56759.26	33.0	0.9
1157.5	56760.12	34.0	0.91
1157.5	56761.05	37.6	0.96
1157.5	56762.12	38.4	0.96
1157.5	56763.05	39.4	0.97
1157.5	56764.24	40.0	0.99
1157.5	56765.17	37.0	0.95
1157.5	56765.97	38.9	0.97
1157.5	56767.03	41.2	0.99
1157.5	56768.09	43.1	1.02
1157.5	56769.15	49.2	1.09
1157.5	56770.08	51.2	1.12
1157.5	56771.08	52.9	1.13
1157.5	56772.01	56.7	1.17
1157.5	56773.07	55.7	1.16

Table 9 — *Continued*

Wavelength (Å)	HJD −2,400,000	F_λ (10^{-15}erg cm^{-2} s^{-1} Å^{-1})	σ_{F_λ}
1157.5	56774.0	54.9	1.15
1157.5	56774.6	55.7	1.16
1157.5	56775.59	52.9	1.14
1157.5	56776.72	48.1	1.08
1157.5	56777.45	50.8	1.1
1157.5	56778.46	47.3	1.07
1157.5	56779.44	47.2	1.07
1157.5	56780.46	46.8	1.06
1157.5	56781.36	45.4	1.05
1157.5	56782.37	42.4	1.01
1157.5	56783.36	49.1	1.08
1157.5	56784.76	55.7	1.16
1157.5	56785.75	60.0	1.21
1157.5	56786.69	55.0	1.15
1157.5	56787.29	53.3	1.14
1157.5	56788.28	52.2	1.12
1157.5	56789.28	46.5	1.05
1157.5	56790.27	42.7	1.01
1157.5	56791.27	42.2	1.01
1157.5	56792.27	49.5	1.09
1157.5	56793.2	50.5	1.11
1157.5	56794.19	47.9	1.07
1157.5	56795.25	44.9	1.03
1157.5	56796.11	45.1	1.04
1157.5	56797.08	52.1	1.12
1157.5	56798.11	50.4	1.1
1157.5	56799.16	49.0	1.09
1157.5	56800.02	50.3	1.1
1157.5	56801.03	49.6	1.09
1157.5	56802.02	49.1	1.09
1157.5	56803.01	48.6	1.08
1157.5	56805.0	45.2	1.05
1157.5	56805.99	45.4	1.04
1157.5	56807.12	44.3	1.03
1157.5	56808.05	46.1	1.05
1157.5	56809.11	47.8	1.07
1157.5	56809.91	46.6	1.06
1157.5	56810.84	45.3	1.05
1157.5	56812.03	49.5	1.09
1157.5	56812.96	51.4	1.11
1157.5	56814.09	52.1	1.12
1157.5	56814.89	55.7	1.16
1157.5	56816.08	57.2	1.18
1157.5	56816.94	62.0	1.24
1157.5	56817.93	68.6	1.31
1157.5	56818.93	72.5	1.34
1157.5	56819.74	71.4	1.34
1157.5	56820.99	67.5	1.29
1157.5	56821.86	64.4	1.26
1157.5	56822.79	60.6	1.22
1157.5	56823.85	59.8	1.2
1157.5	56824.64	58.1	1.18
1157.5	56825.65	53.9	1.14
1157.5	56826.9	44.0	1.03
1157.5	56827.77	43.8	1.03
1157.5	56828.49	42.3	1.02
1157.5	56829.62	38.6	0.96
1157.5	56830.48	38.9	0.96
1157.5	56831.68	42.8	1.01
1157.5	56832.27	43.3	1.02
1157.5	56833.8	49.2	1.09
1157.5	56834.8	50.3	1.11
1157.5	56835.79	45.2	1.04
1157.5	56836.21	45.5	1.04
1157.5	56837.65	45.9	1.05
1157.5	56838.18	45.3	1.04
1157.5	56839.2	46.5	1.06
1157.5	56840.13	47.9	1.08
1157.5	56841.19	45.1	1.04
1157.5	56842.19	45.4	1.04
1157.5	56843.12	43.1	1.02
1157.5	56844.18	39.7	0.98
1157.5	56845.02	39.8	0.98
1157.5	56846.11	40.2	0.99
1157.5	56847.04	38.2	0.96
1157.5	56848.03	37.9	0.95
1157.5	56849.09	37.1	0.95
1157.5	56850.0	33.1	0.9

Table 9 — *Continued*

Wavelength (Å)	HJD −2,400,000	F_λ (10^{-15}erg cm^{-2} s^{-1} Å^{-1})	σ_{F_λ}
1157.5	56850.93	31.6	0.88
1157.5	56851.92	31.6	0.89
1157.5	56852.92	32.8	0.9
1157.5	56854.05	30.7	0.87
1157.5	56855.05	33.2	0.9
1157.5	56856.17	37.5	0.95
1157.5	56857.17	43.8	1.03
1157.5	56858.09	47.5	1.08
1157.5	56858.89	44.0	1.02
1157.5	56860.08	41.4	1.0
1157.5	56860.95	41.0	1.0
1157.5	56861.81	38.4	0.96
1157.5	56862.87	37.0	0.95
1157.5	56863.87	41.8	1.01
1157.5	56864.86	43.2	1.02
1157.5	56865.92	50.6	1.1
1367.0	56690.61	34.27	0.64
1367.0	56691.54	35.45	0.65
1367.0	56692.39	37.71	0.67
1367.0	56693.32	38.14	0.68
1367.0	56695.27	40.94	0.71
1367.0	56696.25	44.25	0.75
1367.0	56697.31	45.3	0.75
1367.0	56698.3	48.27	0.79
1367.0	56699.23	45.8	0.76
1367.0	56700.23	46.0	0.76
1367.0	56701.36	47.46	0.78
1367.0	56702.16	47.74	0.78
1367.0	56703.15	47.56	0.78
1367.0	56705.34	45.77	0.76
1367.0	56706.21	44.7	0.75
1367.0	56707.2	46.65	0.77
1367.0	56708.26	43.24	0.74
1367.0	56709.26	41.43	0.71
1367.0	56710.26	37.69	0.68
1367.0	56711.12	35.22	0.65
1367.0	56712.18	34.76	0.64
1367.0	56713.18	35.18	0.65
1367.0	56714.24	34.45	0.64
1367.0	56715.04	31.46	0.61
1367.0	56715.9	30.58	0.6
1367.0	56716.84	29.64	0.59
1367.0	56718.83	26.75	0.56
1367.0	56720.15	26.01	0.55
1367.0	56721.02	23.76	0.53
1367.0	56722.09	22.25	0.51
1367.0	56723.14	21.87	0.51
1367.0	56726.06	22.96	0.52
1367.0	56727.06	22.72	0.51
1367.0	56727.79	23.07	0.52
1367.0	56728.92	23.91	0.53
1367.0	56729.78	24.54	0.54
1367.0	56730.85	24.22	0.53
1367.0	56731.97	24.69	0.54
1367.0	56732.91	24.39	0.53
1367.0	56733.85	24.94	0.54
1367.0	56734.84	27.63	0.57
1367.0	56735.85	32.43	0.62
1367.0	56736.44	35.78	0.65
1367.0	56737.69	37.88	0.68
1367.0	56738.5	39.91	0.7
1367.0	56739.68	42.46	0.73
1367.0	56740.36	45.44	0.76
1367.0	56741.35	45.23	0.76
1367.0	56744.4	54.35	0.85
1367.0	56745.25	54.79	0.86
1367.0	56746.25	52.54	0.84
1367.0	56747.18	56.59	0.88
1367.0	56748.24	54.97	0.86
1367.0	56749.17	52.83	0.84
1367.0	56750.3	51.55	0.82
1367.0	56751.16	49.37	0.8
1367.0	56752.02	46.72	0.77
1367.0	56753.02	40.89	0.71
1367.0	56753.97	36.19	0.66
1367.0	56755.21	34.46	0.64
1367.0	56756.14	35.46	0.65
1367.0	56757.14	37.26	0.67

Table 9 — *Continued*

Wavelength (Å)	HJD −2,400,000	F_λ (10^{-15}erg cm^{-2} s^{-1} Å^{-1})	σ_{F_λ}
1367.0	56759.26	35.86	0.66
1367.0	56760.12	35.68	0.65
1367.0	56761.05	38.88	0.69
1367.0	56762.12	39.11	0.69
1367.0	56763.05	39.32	0.69
1367.0	56764.24	40.43	0.71
1367.0	56765.17	38.3	0.68
1367.0	56765.97	39.49	0.69
1367.0	56767.03	40.83	0.71
1367.0	56768.09	41.42	0.72
1367.0	56769.15	45.28	0.76
1367.0	56770.08	48.51	0.79
1367.0	56771.08	49.79	0.81
1367.0	56772.01	49.65	0.8
1367.0	56773.07	50.55	0.82
1367.0	56774.0	51.02	0.82
1367.0	56774.6	50.04	0.81
1367.0	56775.59	50.33	0.81
1367.0	56776.72	45.96	0.77
1367.0	56777.45	46.32	0.77
1367.0	56778.46	45.45	0.76
1367.0	56779.44	44.31	0.75
1367.0	56780.46	45.56	0.76
1367.0	56781.36	43.53	0.74
1367.0	56782.37	41.35	0.72
1367.0	56783.36	45.28	0.76
1367.0	56784.76	51.18	0.82
1367.0	56785.75	53.55	0.85
1367.0	56786.69	50.37	0.81
1367.0	56787.29	49.37	0.8
1367.0	56788.28	48.82	0.8
1367.0	56789.28	46.09	0.76
1367.0	56790.27	43.35	0.74
1367.0	56791.27	42.89	0.73
1367.0	56792.27	45.53	0.76
1367.0	56793.2	47.41	0.78
1367.0	56794.19	46.43	0.77
1367.0	56795.25	43.64	0.74
1367.0	56796.11	44.23	0.75
1367.0	56797.08	49.36	0.8
1367.0	56798.11	49.48	0.8
1367.0	56799.16	46.92	0.78
1367.0	56800.02	46.22	0.77
1367.0	56801.03	48.09	0.79
1367.0	56802.02	46.33	0.77
1367.0	56803.01	47.94	0.79
1367.0	56805.0	44.73	0.75
1367.0	56805.99	43.46	0.74
1367.0	56807.12	43.45	0.74
1367.0	56808.05	44.78	0.75
1367.0	56809.11	47.07	0.78
1367.0	56809.91	45.73	0.76
1367.0	56810.84	44.65	0.75
1367.0	56812.03	47.19	0.78
1367.0	56812.96	48.09	0.79
1367.0	56814.09	50.04	0.81
1367.0	56814.89	53.24	0.84
1367.0	56816.08	54.86	0.86
1367.0	56816.94	55.76	0.87
1367.0	56817.93	61.86	0.94
1367.0	56818.93	64.74	0.97
1367.0	56819.74	64.63	0.97
1367.0	56820.99	62.06	0.94
1367.0	56821.86	58.88	0.91
1367.0	56822.79	57.36	0.89
1367.0	56823.85	55.53	0.87
1367.0	56824.64	54.25	0.85
1367.0	56825.65	51.33	0.83
1367.0	56826.9	45.88	0.77
1367.0	56827.77	43.71	0.74
1367.0	56828.49	43.94	0.75
1367.0	56829.62	42.04	0.73
1367.0	56830.48	41.1	0.71
1367.0	56831.68	41.71	0.72
1367.0	56832.27	43.8	0.74
1367.0	56833.8	47.65	0.79
1367.0	56834.8	47.38	0.78
1367.0	56835.79	44.55	0.75

Table 9 — *Continued*

Wavelength (Å)	HJD −2,400,000	F_λ (10^{-15}erg cm^{-2} s^{-1} Å^{-1})	σ_{F_λ}
1367.0	56836.21	44.34	0.75
1367.0	56837.65	44.31	0.75
1367.0	56838.18	44.49	0.75
1367.0	56839.2	44.5	0.75
1367.0	56840.13	45.2	0.76
1367.0	56841.19	44.42	0.75
1367.0	56842.19	44.69	0.75
1367.0	56843.12	42.31	0.73
1367.0	56844.18	40.82	0.71
1367.0	56845.02	41.05	0.71
1367.0	56846.11	40.33	0.71
1367.0	56847.04	38.87	0.69
1367.0	56848.03	37.96	0.68
1367.0	56849.09	37.1	0.67
1367.0	56850.0	35.54	0.66
1367.0	56850.93	34.26	0.64
1367.0	56851.92	33.77	0.64
1367.0	56852.92	34.19	0.64
1367.0	56854.05	33.24	0.63
1367.0	56855.05	34.57	0.65
1367.0	56856.17	38.0	0.68
1367.0	56857.17	43.3	0.74
1367.0	56858.09	45.13	0.76
1367.0	56858.89	43.89	0.75
1367.0	56860.08	40.79	0.71
1367.0	56860.95	40.43	0.71
1367.0	56861.81	39.86	0.7
1367.0	56862.87	37.41	0.68
1367.0	56863.87	41.04	0.72
1367.0	56864.86	43.31	0.74
1367.0	56865.92	47.08	0.78
1478.5	56690.65	29.7	0.48
1478.5	56691.58	31.6	0.51
1478.5	56692.41	33.0	0.52
1478.5	56693.34	33.0	0.52
1478.5	56695.31	35.4	0.56
1478.5	56696.26	38.7	0.6
1478.5	56697.32	40.0	0.62
1478.5	56698.32	41.1	0.63
1478.5	56699.25	40.3	0.62
1478.5	56700.24	40.1	0.62
1478.5	56701.37	40.8	0.63
1478.5	56702.17	41.0	0.63
1478.5	56703.17	42.0	0.65
1478.5	56705.36	39.5	0.61
1478.5	56706.22	38.6	0.6
1478.5	56707.22	40.3	0.62
1478.5	56708.28	36.8	0.58
1478.5	56709.28	35.2	0.55
1478.5	56710.27	32.1	0.51
1478.5	56711.13	29.8	0.48
1478.5	56712.2	30.3	0.49
1478.5	56713.19	30.7	0.49
1478.5	56714.25	29.9	0.48
1478.5	56715.08	28.1	0.46
1478.5	56715.93	26.6	0.44
1478.5	56716.89	25.0	0.41
1478.5	56718.89	23.6	0.4
1478.5	56720.16	22.6	0.38
1478.5	56721.05	20.7	0.36
1478.5	56722.12	19.4	0.34
1478.5	56723.15	18.6	0.32
1478.5	56726.07	19.6	0.34
1478.5	56727.07	19.1	0.33
1478.5	56727.85	20.0	0.35
1478.5	56728.95	21.0	0.36
1478.5	56729.84	21.5	0.36
1478.5	56730.91	21.7	0.37
1478.5	56731.99	21.6	0.37
1478.5	56732.97	21.2	0.36
1478.5	56733.9	21.7	0.37
1478.5	56734.89	24.6	0.41
1478.5	56735.89	28.5	0.46
1478.5	56736.47	31.8	0.51
1478.5	56737.73	34.1	0.54
1478.5	56738.56	35.9	0.56
1478.5	56739.72	38.8	0.6
1478.5	56740.42	40.8	0.63

Table 9 — *Continued*

Wavelength (Å)	HJD −2,400,000	F_λ (10^{-15}erg cm^{-2} s^{-1} Å^{-1})	σ_{F_λ}
1478.5	56741.38	40.8	0.63
1478.5	56744.44	48.7	0.74
1478.5	56745.27	49.1	0.74
1478.5	56746.26	48.5	0.74
1478.5	56747.19	51.0	0.77
1478.5	56748.26	51.1	0.77
1478.5	56749.18	48.0	0.73
1478.5	56750.32	47.1	0.72
1478.5	56751.18	44.5	0.68
1478.5	56752.04	42.6	0.66
1478.5	56753.03	37.0	0.58
1478.5	56754.01	31.9	0.51
1478.5	56755.23	29.8	0.48
1478.5	56756.16	31.2	0.5
1478.5	56757.15	32.1	0.51
1478.5	56759.28	32.6	0.52
1478.5	56760.14	32.2	0.51
1478.5	56761.07	34.1	0.54
1478.5	56762.13	35.3	0.56
1478.5	56763.06	35.4	0.56
1478.5	56764.25	35.3	0.56
1478.5	56765.18	34.7	0.55
1478.5	56765.98	35.5	0.56
1478.5	56767.04	36.2	0.57
1478.5	56768.1	37.5	0.58
1478.5	56769.17	40.9	0.63
1478.5	56770.1	42.6	0.66
1478.5	56771.09	44.2	0.68
1478.5	56772.02	45.5	0.7
1478.5	56773.08	45.3	0.7
1478.5	56774.01	46.1	0.7
1478.5	56774.66	45.1	0.69
1478.5	56775.65	44.5	0.68
1478.5	56776.78	41.4	0.64
1478.5	56777.46	42.0	0.65
1478.5	56778.48	41.3	0.64
1478.5	56779.45	40.0	0.62
1478.5	56780.51	41.2	0.64
1478.5	56781.38	40.4	0.63
1478.5	56782.41	39.5	0.61
1478.5	56783.37	41.7	0.64
1478.5	56784.82	46.5	0.71
1478.5	56785.81	48.3	0.74
1478.5	56786.74	45.8	0.7
1478.5	56787.32	45.5	0.7
1478.5	56788.32	44.4	0.68
1478.5	56789.32	43.0	0.66
1478.5	56790.31	40.2	0.62
1478.5	56791.31	40.7	0.63
1478.5	56792.3	43.4	0.67
1478.5	56793.23	45.1	0.69
1478.5	56794.22	43.1	0.66
1478.5	56795.29	40.6	0.63
1478.5	56796.12	41.0	0.63
1478.5	56797.11	44.3	0.68
1478.5	56798.14	44.6	0.68
1478.5	56799.17	43.1	0.66
1478.5	56800.04	43.0	0.66
1478.5	56801.06	43.7	0.67
1478.5	56802.05	43.3	0.67
1478.5	56803.02	42.6	0.66
1478.5	56805.01	40.8	0.63
1478.5	56806.01	40.0	0.62
1478.5	56807.14	39.6	0.61
1478.5	56808.07	40.9	0.63
1478.5	56809.13	42.2	0.65
1478.5	56809.92	41.2	0.64
1478.5	56810.85	40.8	0.63
1478.5	56812.05	42.3	0.65
1478.5	56812.98	43.0	0.66
1478.5	56814.11	44.0	0.67
1478.5	56814.9	46.8	0.71
1478.5	56816.1	48.0	0.73
1478.5	56816.96	50.2	0.76
1478.5	56817.95	56.1	0.84
1478.5	56818.95	58.3	0.88
1478.5	56819.77	58.8	0.88
1478.5	56821.01	55.0	0.83

Table 9 — *Continued*

Wavelength (Å)	HJD −2,400,000	F_λ (10^{-15}erg cm^{-2} s^{-1} Å^{-1})	σ_{F_λ}
1478.5	56821.87	53.8	0.81
1478.5	56822.82	51.5	0.78
1478.5	56823.86	51.2	0.78
1478.5	56824.68	50.2	0.76
1478.5	56825.7	47.9	0.73
1478.5	56826.91	42.3	0.65
1478.5	56827.8	39.6	0.62
1478.5	56828.56	39.4	0.61
1478.5	56829.68	37.4	0.58
1478.5	56830.55	36.3	0.57
1478.5	56831.71	38.2	0.6
1478.5	56832.29	38.7	0.6
1478.5	56833.81	42.3	0.65
1478.5	56834.81	42.4	0.65
1478.5	56835.81	39.2	0.61
1478.5	56836.26	38.7	0.6
1478.5	56837.69	39.5	0.61
1478.5	56838.2	38.6	0.6
1478.5	56839.26	40.0	0.62
1478.5	56840.18	39.8	0.62
1478.5	56841.25	39.7	0.61
1478.5	56842.25	39.6	0.62
1478.5	56843.17	37.7	0.59
1478.5	56844.24	36.5	0.57
1478.5	56845.04	35.3	0.55
1478.5	56846.16	35.6	0.56
1478.5	56847.08	34.8	0.55
1478.5	56848.08	34.0	0.54
1478.5	56849.14	32.3	0.51
1478.5	56850.01	31.7	0.51
1478.5	56850.94	30.5	0.49
1478.5	56851.94	29.6	0.48
1478.5	56852.93	30.8	0.49
1478.5	56854.06	29.2	0.47
1478.5	56855.06	30.1	0.49
1478.5	56856.19	34.0	0.54
1478.5	56857.18	38.5	0.6
1478.5	56858.11	40.5	0.63
1478.5	56858.91	39.5	0.61
1478.5	56860.1	37.0	0.58
1478.5	56860.96	37.3	0.58
1478.5	56861.82	35.2	0.56
1478.5	56862.89	33.2	0.53
1478.5	56863.88	36.7	0.58
1478.5	56864.88	38.2	0.6
1478.5	56865.94	42.4	0.65
1746.0	56690.65	26.7	0.63
1746.0	56691.58	27.9	0.64
1746.0	56692.41	30.4	0.68
1746.0	56693.34	30.4	0.67
1746.0	56695.31	31.9	0.71
1746.0	56696.26	34.2	0.74
1746.0	56697.32	35.0	0.74
1746.0	56698.32	36.0	0.75
1746.0	56699.25	35.1	0.74
1746.0	56700.24	36.5	0.77
1746.0	56701.37	36.0	0.76
1746.0	56702.17	36.0	0.75
1746.0	56703.17	36.3	0.76
1746.0	56705.36	35.9	0.76
1746.0	56706.22	34.9	0.74
1746.0	56707.22	36.0	0.75
1746.0	56708.28	33.3	0.73
1746.0	56709.28	33.2	0.72
1746.0	56710.27	28.9	0.66
1746.0	56711.13	27.0	0.63
1746.0	56712.2	28.1	0.66
1746.0	56713.19	28.1	0.65
1746.0	56714.25	27.0	0.63
1746.0	56715.08	26.1	0.63
1746.0	56715.93	25.2	0.62
1746.0	56716.89	23.3	0.59
1746.0	56718.89	21.6	0.57
1746.0	56720.16	20.9	0.56
1746.0	56721.05	19.0	0.53
1746.0	56722.12	18.5	0.52
1746.0	56723.15	17.4	0.51
1746.0	56726.07	19.1	0.54

Table 9 — *Continued*

Wavelength (Å)	HJD −2,400,000	F_λ (10^{-15}erg cm^{-2} s^{-1} Å^{-1})	σ_{F_λ}
1746.0	56727.07	18.1	0.52
1746.0	56727.85	18.6	0.52
1746.0	56728.95	19.4	0.53
1746.0	56729.84	19.7	0.54
1746.0	56730.91	20.1	0.54
1746.0	56731.99	19.9	0.54
1746.0	56732.97	19.9	0.55
1746.0	56733.9	20.0	0.54
1746.0	56734.89	22.7	0.58
1746.0	56735.89	25.6	0.63
1746.0	56736.47	28.5	0.65
1746.0	56737.73	29.8	0.67
1746.0	56738.56	32.3	0.71
1746.0	56739.72	33.6	0.73
1746.0	56740.42	35.9	0.75
1746.0	56741.38	35.7	0.75
1746.0	56744.44	41.6	0.83
1746.0	56745.27	41.5	0.83
1746.0	56746.26	42.3	0.84
1746.0	56747.19	43.7	0.87
1746.0	56748.26	42.4	0.84
1746.0	56749.18	40.9	0.82
1746.0	56750.32	40.8	0.81
1746.0	56751.18	38.4	0.79
1746.0	56752.04	37.4	0.77
1746.0	56753.03	34.2	0.74
1746.0	56754.01	29.6	0.67
1746.0	56755.23	26.9	0.64
1746.0	56756.16	28.5	0.66
1746.0	56757.15	29.8	0.68
1746.0	56759.28	29.6	0.67
1746.0	56760.14	28.4	0.66
1746.0	56761.07	31.1	0.7
1746.0	56762.13	30.9	0.69
1746.0	56763.06	32.0	0.71
1746.0	56764.25	31.9	0.71
1746.0	56765.18	31.1	0.69
1746.0	56765.98	31.9	0.7
1746.0	56767.04	33.7	0.74
1746.0	56768.1	32.6	0.71
1746.0	56769.17	35.2	0.75
1746.0	56770.1	36.8	0.77
1746.0	56771.09	38.0	0.79
1746.0	56772.02	39.5	0.8
1746.0	56773.08	38.8	0.8
1746.0	56774.01	39.4	0.81
1746.0	56774.66	39.2	0.8
1746.0	56775.65	38.4	0.79
1746.0	56776.78	37.3	0.78
1746.0	56777.46	37.4	0.78
1746.0	56778.48	36.8	0.78
1746.0	56779.45	34.9	0.75
1746.0	56780.51	35.6	0.75
1746.0	56781.38	35.7	0.75
1746.0	56782.41	34.4	0.74
1746.0	56783.37	35.1	0.75
1746.0	56784.82	39.2	0.81
1746.0	56785.81	41.6	0.83
1746.0	56786.74	40.4	0.82
1746.0	56787.32	39.1	0.81
1746.0	56788.32	38.4	0.8
1746.0	56789.32	36.9	0.77
1746.0	56790.31	34.9	0.74
1746.0	56791.31	34.5	0.74
1746.0	56792.3	35.2	0.75
1746.0	56793.23	37.6	0.79
1746.0	56794.22	36.6	0.77
1746.0	56795.29	34.2	0.74
1746.0	56796.12	34.8	0.75
1746.0	56797.11	38.4	0.79
1746.0	56798.14	37.6	0.78
1746.0	56799.17	36.6	0.78
1746.0	56800.04	36.3	0.78
1746.0	56801.06	36.9	0.77
1746.0	56802.05	36.5	0.77
1746.0	56803.02	36.7	0.78
1746.0	56805.01	35.1	0.75
1746.0	56806.01	35.5	0.76

Table 9 — *Continued*

Wavelength (Å)	HJD −2,400,000	F_λ (10^{-15}erg cm^{-2} s^{-1} Å^{-1})	σ_{F_λ}
1746.0	56807.14	35.7	0.76
1746.0	56808.07	36.2	0.76
1746.0	56809.13	37.6	0.78
1746.0	56809.92	37.1	0.77
1746.0	56810.85	35.9	0.77
1746.0	56812.05	37.5	0.79
1746.0	56812.98	37.9	0.79
1746.0	56814.11	39.7	0.82
1746.0	56814.9	40.9	0.83
1746.0	56816.1	43.0	0.85
1746.0	56816.96	44.6	0.88
1746.0	56817.95	48.1	0.93
1746.0	56818.95	49.6	0.94
1746.0	56819.77	50.8	0.96
1746.0	56821.01	47.9	0.93
1746.0	56821.87	46.9	0.91
1746.0	56822.82	44.8	0.87
1746.0	56823.86	44.0	0.88
1746.0	56824.68	44.2	0.87
1746.0	56825.7	42.4	0.85
1746.0	56826.91	38.3	0.79
1746.0	56827.8	36.4	0.77
1746.0	56828.56	35.2	0.75
1746.0	56829.68	33.6	0.74
1746.0	56830.55	33.0	0.73
1746.0	56831.71	34.8	0.75
1746.0	56832.29	34.6	0.74
1746.0	56833.81	37.5	0.79
1746.0	56834.81	37.8	0.79
1746.0	56835.81	36.2	0.77
1746.0	56836.26	35.9	0.76
1746.0	56837.69	36.2	0.76
1746.0	56838.2	35.2	0.76
1746.0	56839.26	35.5	0.77
1746.0	56840.18	36.5	0.77
1746.0	56841.25	36.4	0.78
1746.0	56842.25	36.3	0.77
1746.0	56843.17	34.6	0.76
1746.0	56844.24	33.6	0.73
1746.0	56845.04	32.5	0.73
1746.0	56846.16	32.4	0.72
1746.0	56847.08	31.8	0.72
1746.0	56848.08	31.6	0.71
1746.0	56849.14	31.2	0.7
1746.0	56850.01	29.2	0.68
1746.0	56850.94	28.4	0.66
1746.0	56851.94	28.0	0.66
1746.0	56852.93	27.5	0.66
1746.0	56854.06	27.4	0.65
1746.0	56855.06	28.1	0.66
1746.0	56856.19	30.1	0.68
1746.0	56857.18	32.7	0.73
1746.0	56858.11	35.0	0.75
1746.0	56858.91	35.0	0.76
1746.0	56860.1	33.2	0.72
1746.0	56860.96	33.5	0.74
1746.0	56861.82	31.2	0.7
1746.0	56862.89	30.2	0.69
1746.0	56863.88	32.9	0.73
1746.0	56864.88	34.2	0.75
1746.0	56865.94	37.6	0.78